Terms and Conditions of Use of Digitised Theses from Trinity College Library Dublin

Copyright statement

All material supplied by Trinity College Library is protected by copyright (under the Copyright and Related Rights Act, 2000 as amended) and other relevant Intellectual Property Rights. By accessing and using a Digitised Thesis from Trinity College Library you acknowledge that all Intellectual Property Rights in any Works supplied are the sole and exclusive property of the copyright and/or other IPR holder. Specific copyright holders may not be explicitly identified. Use of materials from other sources within a thesis should not be construed as a claim over them.

A non-exclusive, non-transferable licence is hereby granted to those using or reproducing, in whole or in part, the material for valid purposes, providing the copyright owners are acknowledged using the normal conventions. Where specific permission to use material is required, this is identified and such permission must be sought from the copyright holder or agency cited.

Liability statement

By using a Digitised Thesis, I accept that Trinity College Dublin bears no legal responsibility for the accuracy, legality or comprehensiveness of materials contained within the thesis, and that Trinity College Dublin accepts no liability for indirect, consequential, or incidental, damages or losses arising from use of the thesis for whatever reason. Information located in a thesis may be subject to specific use constraints, details of which may not be explicitly described. It is the responsibility of potential and actual users to be aware of such constraints and to abide by them. By making use of material from a digitised thesis, you accept these copyright and disclaimer provisions. Where it is brought to the attention of Trinity College Library that there may be a breach of copyright or other restraint, it is the policy to withdraw or take down access to a thesis while the issue is being resolved.

Access Agreement

By using a Digitised Thesis from Trinity College Library you are bound by the following Terms & Conditions. Please read them carefully.

I have read and I understand the following statement: All material supplied via a Digitised Thesis from Trinity College Library is protected by copyright and other intellectual property rights, and duplication or sale of all or part of any of a thesis is not permitted, except that material may be duplicated by you for your research use or for educational purposes in electronic or print form providing the copyright owners are acknowledged using the normal conventions. You must obtain permission for any other use. Electronic or print copies may not be offered, whether for sale or otherwise to anyone. This copy has been supplied on the understanding that it is copyright material and that no quotation from the thesis may be published without proper acknowledgement.

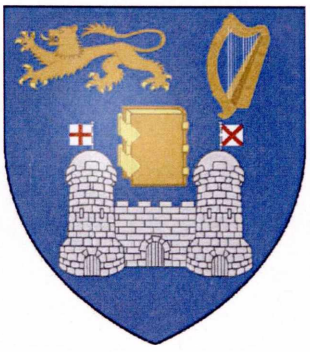

TRINITY COLLEGE DUBLIN

Conductance Probe Microscopy Investigation on the Local Electronic Properties of Single Walled Carbon Nanotube Systems

Thesis submitted to the University of Dublin,
Trinity College for the degree of Doctor of Philosophy

Peter Niraj Nirmalraj

March 30th, 2010.

Center for Research in Adaptive Nanostructures & Nanodevices
School of Chemistry
Trinity College Dublin

Declaration

This thesis is submitted by the undersigned for the degree of Doctor of Philosophy at the University of Dublin, Trinity College and has not been submitted to any other university as an exercise for a degree. I declare that this thesis is entirely my own work and I give permission to the library to lend or copy this thesis upon request.

Contents

Abstract

In order to build electronic devices and circuits comprised of nanoscale materials as the active element it is imperative to unravel the local electronic properties of these materials. We have performed an in-depth study on the local electronic behavior of individual single walled carbon nanotubes (SWCNT) and on two dimensional networks based on these tubes using conductance imaging atomic force microscopy (CI-AFM). This technique allows us to simultaneously investigate the morphology and the local electronic structure of the nanotubes, when a metal coated tip is scanned over the surface. SWCNTs solubilised in N-methyl pyrrolidone (NMP) were sprayed onto SiO_2 substrates to form homogeneous and percolating networks. The electrodes were fabricated using UV-lithographically and these samples were subjected to controlled annealing at 500 degrees Celsius under Ar/H_2 atmosphere to remove the adsorbed NMP molecules.

A novel approach to analyze and optimize nanotube-metal contacts has been developed that makes use of the conductive probe to locally anneal the interface between the metal electrode and the nanotube by the controlled application of voltage pulses. The metallic nanotubes were identified from their semiconducting counterparts by applying a positive gate voltage that sweeps of the carriers from the semiconducting tubes thereby making only the metallic tubes visible in the current map. Using the local annealing technique we show that Pd forms superior contacts resulting in contact resistance values that are amongst the lowest ever reported. Furthermore the onset of conductive pathways across the network was monitored and the percolation threshold for these systems was determined as the network scales from a sparse to a fully connected thick network in a bottom up approach, these results were confirmed by complementary bulk electrical measurements.

In addition naturally occurring junctions between SWCNTs were investigated and we find the charge transport in SWCNT networks to be dominated by resistance at network junctions which scales with the size of the interconnecting bundles. Also the junction resistance can be controlled by acid treatment, and the dominant effect of doping is a dramatic reduction of the barrier to transport between individual tubes and bundles, whereas annealing significantly increases this resistance.

Measured junction resistances for pristine, acid-treated and annealed SWCNT bundles correlate with conductivities of the corresponding films, in excellent agreement with a model in which junctions control the overall network performance.

To My

Most Affectionate Grandparents

Acknowledgements

The past few years in Ireland has been a very fruitful period for which I am greatly indebted to a lot of people who stood by me through all these years.

I am deeply grateful to my supervisor Prof John Boland for having given me the opportunity to work towards my PhD in his lab. He has a profound influence on my overall development as a scientist and I have always admired the methodology in which he approaches a scientific problem. He has given me the space to explore new ideas whilst focussing on the core issues of this project. I hope that some of his scientific calibre has rubbed off me so that I may share it with my future colleagues. I would also like to thank Prof Jonathan Coleman for the stimulating discussions and for having shared his extensive expertise in the area of carbon nanotube dispersions that played a pivotal role in this research work.

I would like to thank Mick Philips and John Sheridan for having taught me on how to use the scanning probe microscope especially about the nuance that was not in the manual. I learnt a lot of little tips and tricks that still helps me in tackling our AFM system. Moving into the present CRANN building in 2007 would have been a difficult task but for the help rendered by past and present members of the Boland research group. The experimental downtime was minimized a lot after the shifting, thanks to Dorothee and Ronan for having been there in setting up the AFM / wet labs. I would also like to thank you both for the suggestions which helped me shape up my work at different points of time and for the good time we had outside the lab. Thanks also to Niall Kinahan, Alan Bell and Eoin McCarthy for spending your time in helping me out in the clean room. I would also like to thank David Meehan for patiently solving my computer related problems. An enormous amount of work was put in by Tarek Lutz and Peter Gleeson in contacting graphene and carbon nanotube materials via electron beam lithography, thanks a lot guys, without your help it would have been a very time consuming experiment. I would also like to thank Sukanta De and Phil Lyons for providing me with the silver nanowire materials for my various experiments and for the four probe measurements on carbon nanotubes they performed. Thanks also to Amro Satti for providing me with the post processed materials of nanotubes through acid treatment.

I take this opportunity to thank Prof Georg Duesberg and his group members for providing me with access to their furnace that facilitated the annealing experiments. I would also like to thank our group administrator Mary McCarthy, Rita Keane and administrative officer Jennifer Egan for all their hardwork and patience throughout all these years.

Thanks to all of you for having created a very nice and healthy working atmosphere for me, it truly has been a real pleasure working with you all. Thanks to SFI and Hewlett Packard for funding this project throughout all stages.

I want to thank my family back at home to whom I owe a lot. To my parents, I cannot just thank them with words for all that they have done for me that has brought me to where I am today. I hope that you will be glad to see the successful completion of my PhD. I want to thank you Appa and Amma for the time and thought you have spent for me in all these years. Huge thanks to my brother Nishanth who has taken care of so many things during my absence from home, which allowed me to concentrate on my work better and for all the great time we had. I would like to thank my grandparents to whom I owe a lot for the love and affection they showered upon me throughout all these years and I hope I have lived up to the high expectations that they all had in me. I would like to thank Natacha for her continuous support and affection, you have been very understanding and thanks for having been by my side during difficult times.

Thanks to Priya with whom I started working towards the distant dream of starting a career in nanoscience and I would like to thank you for all your efforts and timely advice. I would like to thank all my family and friends in India and here in Ireland with whom I had a wonderful time and I would like to wish you all success in your future endeavours.

Acronyms

AFM	Atomic force microscopy
Al_2O_3	Aluminium oxide
AlN	Aluminium nitride
Au	Gold
BN	Boron nitride
CI-AFM	Conductance imaging atomic force microscopy
CNT	Carbon nanotube
CVD	Chemical vapour deposition
FET	Field effect transistor
GaN	Gallium nitride
Ga_2O_3	Gallium oxide
HiPCO	High pressure carbon monoxide
HNO_3	Nitric acid
H_2SO_4	Sulphuric acid
HOPG	Highly oriented pyrolytic graphite
ITO	Indium tin oxide
InP	Indium phosphide
MWCNT	Multi walled carbon nanotube
NMP	N-methyl-pyrollidone
NTN	Nanotube network
NO_2	Nitrogen Dioxide
Pd	Palladium
Pt	Platinum
SWCNT	Single walled carbon nanotube
SPM	Scanning probe microscopy
SEM	Scanning electron microscope
STM	Scanning tunneling microscopy
SiC	Silicon carbide
Si	Silicon
Si_3N_4	Silicon nitride
STS	Scanning tunneling spectroscopy
SDBS	Sodium dodecyl benzene sulfonate

SDS	Sodium dodecyl sulfonate
SiO_2	Silicon Dioxide
SnO_2	Tin oxide
Sc	Scandium
TEM	Transmission electron microscope
Ti	Titanium
TiC	Titanium carbide
vHSs	van Hove Singularities
Y	Yttrium

List of Figures & Tables

Chapter 1

Chapter 2

Chapter 3

Chapter 4

Chapter 5

Chapter 6

Chapter 7

.

Introduction

Nanoscience brings scientists together across broad disciplines spanning synthetic biotechnology, condensed matter physics, organic chemistry to electronic engineering in order to study matter on length scales that are less than 100 nm (1nm = 10^{-9} m). Nanotechnology is defined as the ability to build materials and devices with control down to the level of individual atoms and molecules.

Devices based on materials of reduced dimensions are expected to surpass the performance of those based on conventional technologies as the basic properties of nanoscale materials vary significantly from their bulk counterparts. Physical phenomena like surface tension, van der Waals attraction and the increase in surface to volume ratio play a more significant role on the nanoscale when compared to the macroscale. A detailed understanding is therefore required to exert control over these nanoscale properties thereby opening up a wide range of applications based on nanoscale materials. The progress of nanoscience was accelerated by the advent of scanning probe microscopy (SPM) nearly three decades ago [1-4] which has now become a routine imaging tool which faithfully reproduces the structural features with atomic resolution in real space [5-7].

Emergence of Scanning Probe Microscopy

Scanning tunneling microscopy (STM) and atomic force microscopy (AFM) are the two principal techniques that helped define the basis for SPM. STM revolutionised the field of nanoscience and has been instrumental in not just imaging nanoscale materials and describing their detailed electronic and vibrational properties but has also made nanoscale manipulation possible thereby enabling scientists to build and explore the properties of material assemblies that was hitherto impossible. One such example was the effort of Eigler et al, who positioned 35 xenon atoms on a nickel (100) surface to spell the word IBM [8] and later studies involving the creation of quantum corals. Pioneering work was performed again in IBM where they demonstrated the capability to vertically manipulate atoms of semiconductor surfaces [9] and to reversibly transfer a single atom between the tip of a STM and a metallic surface. This led to switching behaviour in the tunnelling current by applying a selective voltage bias [10].

In due course STM was employed to construct nanoscale systems including formation of an atomic wire [11], studying the local interface between metal-molecule architectures [12-14] and computation with individual molecules [15]. More intriguing mechanisms like the quantum confinement of electrons in two [16-18] and three dimensions [19], doping of single molecules [20], stimulation of chemical reactions [21], conformational changes of molecules at surfaces [22-25], single bonds [26] and the magnetic properties of matter in atomic scale [27]. The prowess of the STM in terms of atomic scale imaging and structural manipulation has long overshadowed the potential of AFM, although the invention of both these techniques were intimately related [28]. Unlike STM where the current of electrons quantum mechanically tunnelling through a vacuum gap between a biased tip and a conductive surface is measured, the AFM operates by scanning a probe across a surface (conductive and insulating) that acts to traduce the localised tip-sample force interaction. The resulting image is a convolution between the tip geometry and the surface topography together with the spatial variation of the force under study. More recent studies have demonstrated the capability of the AFM to match and perhaps surpass STM by resolving the individual atoms within a pentacene molecule adsorbed on copper (111) and sodium chloride film [5]. AFM also offers the possibility to register several other physical quantities in addition to its capability to map the surface topography by developing probe specifically designed to detect spatially varying force gradients that exist in the sample. Measurements ranging from the visualisation of domain walls in nickel films [29], observing magnetic stray fields of cobalt nanoclusters films [30] using magnetic force microscopy, probing nanoscale dipole-dipole interactions [31], analysing the local work function of Pt/TiO_2 [32] using electric force microscopy and dopant profiling in semiconductors using scanning capacitance microscopy [33, 34] have been reported so far. This rich local information is obtained as a secondary data when the probe is employed in non contact mode in addition to the simultaneously obtained topographic information. A higher resolution mode exists where the probe (metal coated) is scanned over a conductive sample in contact mode thereby generating local electronic information. Conductance imaging atomic force microscopy (CI-AFM) is one such technique which has been an important tool in investigating several local electronic interactions in nanoscale material systems, ranging from electronic transport in individual carbon nanotubes [35-39], carbon nanotube junctions [40, 41], probing the conductivity of biological systems like DNA [42] and proteins [43].

Nanoscale Materials

The advancements in the instrumentation discipline of nanoscience has enabled the emergence of a new class of materials such as zero dimensional quantum dots [44], one dimensional nanotubes [45], two dimensional structures like quantum wells [46] and graphene [47]. These artificial building blocks can be synthesized using various approaches and the ability to generate these minuscule structures is essential to nanoscale science and technology.

Zero Dimensional Nanomaterials

Quantum dots for instance are prepared through a range of methods from colloidal chemistry techniques [48, 49], molecular beam epitaxy [50] and metalorganic chemical vapour deposition [51]. These as-synthesised semiconducting nanocrystals have a size dependence on their bandgap. As the charge carriers are confined to a restricted volume, quantum mechanical phenomena start to gain prominence for which the range of sizes under investigation is frequently called the size quantization regime. Some quantum dots are small regions of one material buried in another with a larger bangap like CdSe and ZnS quantum dots. Due their sharper density of states the quantum dots have superior optical and transport properties hence finding applications as molecular labelling in cell biology [52], diode lasers [53] and as solar cells [54]. The phenomena of electron tunneling through 0D quantum dots have led to the concepts of the artificial atom and the evolution of single electron transistors [55].

One Dimensional Nanomaterials

1D nanostructures like nanowires and nanotubes are equally interesting as they are the smallest dimension structures that can be used for efficient transport of electrons and optical excitations, and are thus expected to be decisive in the development of a new generation of nanostructured devices. Nanowires are classified based on their electronic nature as metallic (Pt, Al, Au, Ag), semiconducting (Si, InP), organic (DNA complexes), oxide based (Al_2O_3, Ga_2O_3, SnO_2), metal carbide (SiC, TiC), nitride based (BN, AlN, GaN) and the growth mechanism differs for each these electronic species. An important aspect relating to nanowires crystallisation involves nucleation and growth.

Some standardised techniques adopted over the past years for the synthesis of nanowires include vapour-liquid-solid growth [56], oxide-assisted laser ablation [57], carbothermal reactions [58], solution based growth [59], template based synthesis [60] and solvothermal synthesis [61, 62]. Novel strategies like encapsulation of CeF_3 within carbon nanotubes followed by controlled removal of the carbon sheaths has resulted in highly crystalline CeF_3 nanowires [63]. The resulting nanowires have been probed from different perspectives and their electrical, mechanical, optoelectronic and electromechnical properties have been studied in detail. Additional properties such as quantised conductivity of nanowires [64-66], realising the ultimate strength for nanowires in line with theoretical predictions [67] and excellent luminescent behaviour has been extensively reported [68]. A deeper understanding of these reported properties and in addition to addressing crucial issues like the role of defects, influence of edge structures, the role of finite size and spin charge separation as predicted for a Luttinger liquid may also provide important insight that lead to new device developments.

Two Dimensional Nanomaterials

A more recently reported 2D nanomaterial that has been attracting widespread research interest is graphene which was first observed in the free state by Novoselov et al [69]. This two dimensional monolayer of sp^2 bonded carbon atoms has exotic electronic properties ranging from ballistic transport [70], quantum hall effect at room temperature [71, 72] and a size dependent bandgap [73, 74], all of which may enable new kinds of nanoscale electronic devices. Improvement in the mechanical [75] and solvent-based processing and synthesis of graphene [76], combined with the ability to transfer these materials from one substrate to another [77] have now opened the door to possible applications of graphene films. Graphene's excellent in-plane conductivity and the ability to make ultra thin materials with limited optical absorption are particularly suited to transparent and flexible electronics applications [78, 79]. Graphene research is still at an embryonic stage and there are numerous interesting physical phenomena that remain to be understood.

Nanomaterial Systems Investigated in this Study

1) Individual Single Walled Carbon Nanotubes

One particular nanomaterial that has continued to remain in the spotlight of the scientific community ever since it was first reported by Iijima [45, 80] nearly two decades ago is carbon nanotubes (CNT's). These one dimensional materials represent one of the finest examples of modern day nanostructures derived by bottom-up chemical synthesis methodology. Studying the local electronic behaviour of the single walled carbon nanotube systems is the primary focus of this PhD thesis. The origin of the carbon nanotube traces back to the mid 1980's when Smalley and co-workers developed the chemistry of fullerenes [81, 82]. Fullerenes are geometric cage-like structures of carbon atoms that are composed of hexagonal and pentagonal faces. The first closed, convex structure formed was the C60 molecule which is a closed cage of 60 carbon atoms where each side of a pentagon is the adjacent side of a hexagon and is popularly known as the bucky ball.

A few years later helical microtubules of graphitic carbon were discovered [45] and single shelled carbon nanotubes of ~1 nm were reported [80]. A single walled carbon nanotube (SWCNT) is formed by rolling a single graphene sheet into a cylinder along a (m,n) lattice vector in the graphene plane. The (m,n) indices determine the bandgap of the tube which is inversely proportional to its diameter [83] and depending on the chirality (the chiral angle between the hexagons and the tube axis) the tubes can be either metallic or semiconducting. A multiwalled nanotube on the other hand comprises an array of single walled nanotubes that are concentrically nested like the growth rings in the trunk of a tree [84]. The nanotubes are synthesised using a variety of procedures from arc-discharge [85], chemical vapour deposition [86] and laser ablation [87], the electronic composition of the as prepared CNT bulk material consists of 33% metallic and 67% semiconducting tubes [83]. The as-prepared carbon nanotubes exists as ropes due to their high surface energy and they have to be exfoliated into smaller bundles or individual tubes to examine their intrinsic properties. The exception are nanotubes synthesized through chemical vapour deposition where the tubes are already grown as individual units, however, these tend to aggregate in to ropes/bundles during solvent processing.

Enormous amount of effort has been dedicated to successfully debundle SWCNT ropes into constituent individual tubes in liquid phase systems by dispersing them in a range of amide solvents [88-90], surfactants [91], acids [92] as well as through covalent functionalization techniques [93]. The resultant dispersions were subjected to a controlled sonication and centrifugation treatment to further narrow down the diameter distribution until a sufficient population of individual tubes is attained [90]. The electronic properties of the debundled SWCNTs have been examined using bulk electrical characterisation techniques thereby revealing information on the electrical charge transport along a tube [94-97], contact resistance between the nanotube-metal electrode [98-101] and the resistance at carbon nanotube junctions [102-104]. These nanoscale properties have also been studied using local probe microscopy techniques such as STM [7, 105-108] and STS [109] which probes the electronic density of states of the material along with its atomic structure. CI-AFM [36-41] and EFM [31, 32] have also been adopted to explore these materials, wherein they simultaneously register the local electronic and topographic data with nanometer scale lateral resolution.

Although ballistic transport was first predicted in these one dimensional [110, 111], experimental results on metallic nanotubes have been shown to reach an intrinsic resistance close to the theoretically predicted conductance values (~6.5 kΩ) at room temperature [112, 113]. Semiconducting nanotubes have come within 25% of this theoretical limit at room temperature [100, 112, 114] and to within a few percent at low temperatures [112, 114]. In order to achieve excellent transport along a pristine SWCNT it is necessary to establish good metal electrode-tube coupling as large metal-nanotube contact resistance has led to Coulomb charging effects [115] and to eliminate the structural defects along the tube that reduce the performance of single tube based devices [116]. The key issue of reducing the contact resistance between the metal-nanotube architecture has been an area of active research interest, that has been approached from different angles by selective choice of metals with varying work functions [98-101, 117] and post deposition treatments like rapid thermal annealing [118], electroless metal deposition [119], ultrasonic nanowelding [120], electrical stressing [121] and Joule heating [122, 123] have been performed in order to minimize the contact resistance between the metal of choice and the nanotube.

Apart from the electronic properties of isolated nanotubes and nanotube-metal interfaces, the junction between nanotubes is potentially intriguing due to the variations in the electronic nature of the tubes involved in the formation of these junctions. Naturally occurring junction between metal-metal, metal-semiconducting, semiconducting-semiconducting tubes have been analysed and the conductance was observed to drop significantly at the intersection between the tubes and the junction between a metal-semiconducting tube was reported to be the most resistive in comparison to the other possible junction configurations [104].

This formation of highly resistive junction has been attributed to the formation of a Schottky barrier in addition to the already present tunnel barrier between the tubes [104, 124]. Apart from naturally occurring junctions, artificially manipulated junctions have also been reported [125-128], and extensive studies have been carried out on the structural and electronic property of these junctions [102, 126, 129-132] which have been observed to exhibit rectifying behaviour at room temperature [102, 131]. Based on these intrinsic properties, SWNTs have been proposed as an ideal system for the realization of molecular electronics. Single electron transistors based on metallic nanotubes [115] and field effect transistors based on semiconducting nanotubes have been demonstrated [133]. Three terminal junctions based on individual SWCNTs have also been demonstrated where the third terminal is employed as a gate electrode that controls the switching mechanism, power gain or other transistor applications involved in any extended molecular circuit [102, 130, 134].

2) Single Walled Carbon Nanotube Networks

However, for devices comprised of individual tubes controlling the chirality and material placement remains a challenge, an alternative strategy involves the application of networks based on nanotubes where the effects due the individual variations are greatly suppressed by the ensemble averaging over a large number of tubes. This particular aspect make nanotube networks (NTNs) promising candidates in applications ranging from thin film transistors [135] to flexible displays [136-147]. The arena of display technology has undergone an interesting transition from cathode ray tubes to present day volatile flat panel displays.

The future of display devices is expected to be dominated by flexible electronic displays, which will ultimately be extended to ultra-thin displays or electronic paper applications. Electronic paper, unlike flat panel displays will have low power consumption, will not require front or backlight and is viewable under different lighting conditions, including direct sunlight. The core building block of present day display devices is Indium Tin Oxide (ITO). ITO is preferred due to its high conductivity and optical transparency, but it has some major setbacks such as high cost and lack of flexibility. As we reach the limits of ITO's capability, not to mention the limited world supply of Indium, the emergence of NTNs comprised of 2D random array of conducting sticks has opened up a wide range of applications from condensed matter physics to transparent conducting electrodes. These opportunities extend beyond the display field to include any area where the capture of light and high conductivity is required, such as solar cells.

The present industry standards for realizing transparent and flexible electronics is to achieve an optical and electrical standard of transmittance $T > 90\%$ and sheet resistance $R_s < 100\Omega$/square. NTNs have the added advantage that they are flexible [139, 140], reproducibly mass produced, and done so at low cost and high efficiency making them ideal for applications such as electronic paper. There is a massive body of literature on the bulk electrical characterization [135, 136, 145, 148-154] of these networks that have reported a conductivity values that ranges from 400 [148] to 6600 S/cm [154]. The reasons for such huge variations in the conductivity has been attributed to the volume faction of metallic and semiconducting tubes within the network, doping level of semiconducting tubes, purity of the nanotube material and the presence of junctions. Studies by Simien et al. [155] and Hecht et al. [156] have systematically analyzed the influence of the length of the tubes on the overall conductivity of the NTNs thereby highlighting the importance of retaining the length of the nanotubes to maximise the conductivity of the networks. Other viable means such as treating the NTNs with acids has shown to improve its conductivity considerably [142, 143, 157-159]. Previously, CI-AFM was used by Fujiwara et al.[37, 41], Stadermann et al. [36, 39] Pablo et al. [160] and Rispal et al. [35] to study the local electronic properties of individual nanotubes/bundles in SWCNT networks. These studies did not examine in detail the dependence of the local resistance at junctions on the diameter of constituent tubes, although Stadermann et al. [39] highlighted that increases in resistance in NTNs coincided with junction locations.

Thesis Outline

A vast majority of the bulk experimental studies have addressed the key issues affecting the network performance and have reported on the overall properties and limitations of such systems. In this thesis we will examine these issues in finer detail where we report on the local contributions and factors affecting the overall network performance. We have employed the CI-AFM technique to capture the local electronic behavior of the SWNT systems with nanometer scale lateral resolution and suggest novel approaches to improve the overall conductivity of both the networks and individual tubes.

Chapter 1 discusses the geometry, synthesis and electronic properties of the carbon nanotubes. Chapter 2 focuses on the methodology and methods of probe microscopic approaches used in this study to characterize the SWCNT systems. In chapter 3 we discuss the synthesis of SWCNT dispersions through liquid phase exfoliation of as produced nanotube powder and the subsequent formation of homogeneous nanotube networks through spray coating approach. Chapter 4 discusses a novel approach to tune and optimize the contact resistance of SWCNTs with two of the widely used metal electrodes; Pd and Ti/Au. Chapter 5 is focused on studying the formation of percolative pathways in a nanotube network as a function of network thickness.

Chapter 6 deals with the intrinsic conductivity of individual SWCNTs, SWCNT bundles, the junction resistance between individual tubes and bundles. Chapter 7 concerns the effect of acid treatment and annealing on the intrinsic conductivity of pristine SWCNTs/bundles and its influence on the junction resistance. Finally the junction resistance is linked to the corresponding conductivities of pristine, acid treated, annealed films and in doing so a transport model has been devised for testing the validity between the nanoscopic and macroscopic approach.

References

[1] G. Binnig *et al.*, Surface Science **189**, 1 (1987).
[2] G. Binnig, C. F. Quate, and C. Gerber, Physical Review Letters **56**, 930 (1986).
[3] G. Binnig, and H. Rohrer, Reviews of Modern Physics **59**, 615 (1987).
[4] G. Binnig *et al.*, Physical Review Letters **49**, 57 (1982).
[5] L. Gross *et al.*, Science **325**, 1110 (2009).
[6] P. Kowalczyk *et al.*, Applied Physics A: Materials Science & Processing **87**, 37 (2007).
[7] O. Marti *et al.*, Surface Science **181**, 230 (1987).
[8] D. M. Eigler, and E. K. Schweizer, Nature **344**, 524 (1990).
[9] I. W. Lyo, and P. Avouris, Science **253**, 173 (1991).
[10] D. M. Eigler, C. P. Lutz, and W. E. Rudge, Nature **352**, 600 (1991).
[11] N. Nilius, T. M. Wallis, and W. Ho, Science **297**, 1853 (2002).
[12] G. V. Nazin, X. H. Qiu, and W. Ho, Science **302**, 77 (2003).
[13] J. Repp *et al.*, Science **312**, 1196 (2006).
[14] L. Lafferentz *et al.*, Science **323**, 1193 (2009).
[15] A. J. Heinrich *et al.*, Science **298**, 1381 (2002).
[16] M. F. Crommie, C. P. Lutz, and D. M. Eigler, Science **262**, 218 (1993).
[17] L. Heller *et al.*, Phys Rev B Condens Matter **49**, 1104 (1994).
[18] H. C. Manoharan, C. P. Lutz, and D. M. Eigler, Nature **403**, 512 (2000).
[19] C. R. Moon *et al.*, Nat Nanotechnol **4**, 167 (2009).
[20] D. Kitchen *et al.*, Nature **442**, 436 (2006).
[21] S. W. Hla *et al.*, Phys Rev Lett **85**, 2777 (2000).
[22] J. K. Gimzewski *et al.*, Science **281**, 531 (1998).
[23] B. C. Stipe, M. A. Rezaei, and W. Ho, Science **279**, 1907 (1998).
[24] T. Komeda *et al.*, Science **295**, 2055 (2002).
[25] J. I. Pascual *et al.*, Nature **423**, 525 (2003).
[26] H. J. Lee, and W. Ho, Science **286**, 1719 (1999).
[27] C. F. Hirjibehedin, C. P. Lutz, and A. J. Heinrich, Science **312**, 1021 (2006).
[28] C. Gerber, and H. P. Lang, Nat Nanotechnol **1**, 3 (2006).
[29] C. T. Hsieh, J. Q. Liu, and J. T. Lue, Applied Surface Science **252**, 1899 (2005).
[30] S. A. Koch *et al.*, Applied Surface Science **226**, 185 (2004).
[31] T. Mélin *et al.*, Physical Review Letters **92**, 166101 (2004).
[32] K. Hiehata, A. Sasahara, and H. Onishi, Nanotechnology **18**, 084007 (2007).
[33] M. L. O'Malley *et al.*, Applied Physics Letters **74**, 272 (1999).
[34] A. Erickson *et al.*, Journal of Electronic Materials **25**, 301 (1996).
[35] L. Rispal *et al.*, Japanese Journal of Applied Physics Part 1-Regular Papers Brief Communications & Review Papers **45**, 3672 (2006).
[36] M. Stadermann *et al.*, Physical Review B **72** (2005).
[37] A. Fujiwara *et al.*, Applied Physics Letters **80**, 1993 (2002).
[38] P. J. de Pablo *et al.*, Advanced Materials **12**, 573 (2000).
[39] M. Stadermann *et al.*, Physical Review B **69**, 201402 (2004).
[40] P. N. Nirmalraj *et al.*, Nano Letters **9**, 3890 (2009).
[41] A. Fujiwara *et al.*, Physica B-Condensed Matter **323**, 227 (2002).
[42] T. Heim, D. Deresmes, and D. Vuillaume, Journal of Applied Physics **96**, 2927 (2004).
[43] D. Xu *et al.*, Nano Letters **5**, 571 (2005).
[44] A. P. Alivisatos, Acs Nano **2**, 1514 (2008).
[45] S. Iijima, Nature **354**, 56 (1991).

[46] H. Benisty, C. M. Sotomayor-Torrès, and C. Weisbuch, Physical Review B **44**, 10945 (1991).
[47] A. K. Geim, and K. S. Novoselov, Nat Mater **6**, 183 (2007).
[48] M. A. Hines, and P. Guyot-Sionnest, The Journal of Physical Chemistry **100**, 468 (1996).
[49] A. Mews *et al.*, The Journal of Physical Chemistry **98**, 934 (1994).
[50] C.-P. Lee, and D.-C. Liu, Applied Surface Science **92**, 519 (1996).
[51] J. H. Ryou, and R. D. Dupuis, Journal of Electronic Materials **32**, 18 (2003).
[52] D.-z. Yang, S.-k. Xu, and Q.-f. Chen, Spectroscopy and Spectral Analysis **27**, 1807 (2007).
[53] K. Sears *et al.*, (Inst. of Elec. and Elec. Eng. Computer Society, Brisbane, Australia, 2006), pp. 505.
[54] D. W. Zhang *et al.*, (SPIE, Wuhan, China, 2009), pp. Chinese Optical Society; Huazhong University of Science and Technology; China Hubei Provincial Science Technology Department; Adm. Comm. Wuhan East Lake High.
[55] R. C. Ashoori, Nature **379**, 413 (1996).
[56] I. K. Ng, and H. Suzuki, (Maney Publishing, Suite 1C, Joseph's Well, Hanover Walk, Leeds, LS3 1AB, United Kingdom, 2009), pp. 192.
[57] W. S. Shi *et al.*, Applied Physics Letters **78**, 3304 (2001).
[58] J. V. D. S. Araujo *et al.*, Solid State Sciences **11**, 1673 (2009).
[59] H. Gerung *et al.*, Journal of the American Chemical Society **128**, 5244 (2006).
[60] H. S. Shin, J. Y. Song, and J. Yu, Materials Letters **63**, 397 (2009).
[61] S. Biswas *et al.*, Journal of Physical Chemistry C **113**, 3617 (2009).
[62] K.-B. Tang *et al.*, Advanced Materials **15**, 448 (2003).
[63] W. Zhiyu, Z. Zongbin, and Q. Jieshan, Chemistry of Materials **19**, 89 (2007).
[64] C. Z. Li, and et al., Nanotechnology **10**, 221 (1999).
[65] Y. Oshima *et al.*, Journal of the Physical Society of Japan **75**, 053705 (2006).
[66] B. Rodell *et al.*, Nanostructured Materials **7**, 229 (1996).
[67] L. T. Ngo *et al.*, Nano Lett **6**, 2964 (2006).
[68] Y. Kim *et al.*, (SPIE, Gwangju, Korea, Republic of, 2006), pp. SPIE; Optical Society of Korea.
[69] K. S. Novoselov, Science **306**, 666 (2004).
[70] F. Miao *et al.*, Science **317**, 1530 (2007).
[71] D. A. Abanin *et al.*, Phys Rev Lett **98**, 196806 (2007).
[72] K. S. Novoselov *et al.*, Science **315**, 1379 (2007).
[73] A. H. Castro Neto *et al.*, Reviews of Modern Physics **81**, 109 (2009).
[74] J. Nilsson *et al.*, Phys Rev Lett **97**, 266801 (2006).
[75] C. Lee *et al.*, Science **321**, 385 (2008).
[76] Y. Hernandez *et al.*, Nat Nanotechnol **3**, 563 (2008).
[77] A. Reina, Nano Lett. (2008).
[78] W. Cai *et al.*, Applied Physics Letters **95**, 123115 (2009).
[79] K. S. Kim *et al.*, Nature **457**, 706 (2009).
[80] S. Iijima, and T. Ichihashi, Nature **363**, 603 (1993).
[81] H. W. Kroto, Nature **329**, 529 (1987).
[82] H. W. Kroto *et al.*, Nature **318**, 162 (1985).
[83] R. Saito *et al.*, Applied Physics Letters **60**, 2204 (1992).
[84] E. Couteau *et al.*, Chemical Physics Letters **378**, 9 (2003).
[85] C. Journet *et al.*, Nature **388**, 756 (1997).
[86] Y. Y. Wei *et al.*, Applied Physics Letters **78**, 1394 (2001).
[87] M. Yudasaka *et al.*, The Journal of Physical Chemistry B **103**, 6224 (1999).
[88] K. D. Ausman *et al.*, The Journal of Physical Chemistry B **104**, 8911 (2000).

[89] S. D. Bergin *et al.*, ACS Nano **3**, 2340 (2009).
[90] S. Giordani *et al.*, Journal of Physical Chemistry B **110**, 15708 (2006).
[91] H. Wang, Current Opinion in Colloid and Interface Science **14**, 364 (2009).
[92] P. K. Rai *et al.*, (American Scientific Publishers, 25650 North Lewis Way, Stevenson Ranch, CA 9138-1439, United States, 2007), pp. 3378.
[93] J. Amiran *et al.*, The Journal of Physical Chemistry C **112**, 3519 (2008).
[94] S. Li *et al.*, Nano Letters **4**, 2003 (2004).
[95] R. Martel *et al.*, Physical Review Letters **87**, 256805 (2001).
[96] S. J. Tans *et al.*, Nature **386**, 474 (1997).
[97] C. Zhou, J. Kong, and H. Dai, Phys Rev Lett **84**, 5604 (2000).
[98] A. Javey *et al.*, Nano Letters **4**, 447 (2004).
[99] A. Javey *et al.*, Physical Review Letters **92**, 106804 (2004).
[100] A. Javey *et al.*, Nature **424**, 654 (2003).
[101] A. A. Kane *et al.*, Nano Letters **9**, 3586 (2009).
[102] A. N. Andriotis *et al.*, Phys Rev Lett **87**, 066802 (2001).
[103] W. Dacheng, and L. Yunqi, Advanced Materials **20**, 2815 (2008).
[104] M. S. Fuhrer *et al.*, Science **288**, 494 (2000).
[105] P. A. Albrecht, and J. W. Lyding, (IEEE, Piscataway, NJ, USA, 2005), pp. 49.
[106] A. Hassanien *et al.*, (Elsevier, Switzerland, 2004), pp. 338.
[107] Z. Osvath *et al.*, Chemical Physics Letters **365**, 338 (2002).
[108] L. Tapaszto *et al.*, Journal of Physics: Condensed Matter **18**, 5793 (2006).
[109] J. W. Janssen *et al.*, Physical Review B (Condensed Matter and Materials Physics) **65**, 115423 (2002).
[110] L. Chico *et al.*, Physical Review B (Condensed Matter) **54**, 2600 (1996).
[111] Y. Young-Gui, and S. G. Louie, (Kluwer Academic Publishers, Dordrecht, Netherlands, 2001), pp. 233.
[112] J. Kong *et al.*, Phys Rev Lett **87**, 106801 (2001).
[113] W. Liang *et al.*, Nature **411**, 665 (2001).
[114] M. J. Biercuk *et al.*, Phys Rev Lett **94**, 026801 (2005).
[115] M. Bockrath *et al.*, Science **275**, 1922 (1997).
[116] M. Freitag *et al.*, Physical Review Letters **89**, 216801 (2002).
[117] A. Javey *et al.*, Nano Lett **5**, 345 (2005).
[118] J.-O. Lee *et al.*, Journal of Physics D: Applied Physics **33**, 1953 (2000).
[119] R. Seidel *et al.*, Nano Letters **3**, 965 (2003).
[120] C. Chen *et al.*, Nanotechnology **17**, 2192 (2006).
[121] Q. Chen, S. Wang, and L.-M. Peng, Nanotechnology **17**, 1087 (2006).
[122] L. Dong *et al.*, Journal of Applied Physics **101**, 024320 (2007).
[123] Y. Woo, G. S. Duesberg, and S. Roth, Nanotechnology **18**, 095203 (2007).
[124] Z. Yao *et al.*, Nature **402**, 273 (1999).
[125] N. Gothard *et al.*, Nano Letters **4**, 213 (2004).
[126] D.-H. Kim *et al.*, Nano Letters **6**, 2821 (2006).
[127] J.-M. Ting, and C.-C. Chang, Applied Physics Letters **80**, 324 (2002).
[128] I. Zsoldos *et al.*, Modelling and Simulation in Materials Science and Engineering **12**, 1251 (2004).
[129] P. Lambin, and V. Meunier, (Kluwer Academic Publishers, Dordrecht, Netherlands, 2001), pp. 265.
[130] M. Menon *et al.*, Physical Review Letters **91**, 145501 (2003).
[131] C. Papadopoulos *et al.*, Physical Review Letters **85**, 3476 (2000).
[132] M. S. Wang *et al.*, Advanced Functional Materials **15**, 1825 (2005).
[133] S. J. Tans, A. R. M. Verschueren, and C. Dekker, Nature **393**, 49 (1998).
[134] L. W. Liu *et al.*, Physical Review B **71**, 155424 (2005).

[135] E. Artukovic *et al.*, Nano Letters **5**, 757 (2005).
[136] C. M. Aguirre *et al.*, Applied Physics Letters **88** (2006).
[137] T. M. Barnes *et al.*, Physical Review B **75** (2007).
[138] T. M. Barnes *et al.*, Applied Physics Letters **90** (2007).
[139] S. De *et al.*, Acs Nano **3**, 714 (2009).
[140] E. M. Doherty *et al.*, Carbon **In press** (2009).
[141] G. Eda *et al.*, Applied Physics Letters **92** (2008).
[142] G. Fanchini, H. E. Unalan, and M. Chhowalla, Applied Physics Letters **90** (2007).
[143] H. Z. Geng *et al.*, Journal of the American Chemical Society **129**, 7758 (2007).
[144] H. Z. Geng *et al.*, Chemical Physics Letters **455**, 275 (2008).
[145] G. Gruner, Journal of Materials Chemistry **16**, 3533 (2006).
[146] B. B. Parekh *et al.*, Applied Physics Letters **90** (2007).
[147] Z. C. Wu *et al.*, Science **305**, 1273 (2004).
[148] E. Bekyarova *et al.*, Journal of the American Chemical Society **127**, 5990 (2005).
[149] G. Gruner, Scientific American **296**, 76 (2007).
[150] L. Hu, D. S. Hecht, and G. Gruner, Nano Letters **4**, 2513 (2004).
[151] M. Kaempgen *et al.*, Nano Letters **9**, 1872 (2009).
[152] V. Skakalova *et al.*, Physical Review B (Condensed Matter and Materials Physics) **74**, 85403 (2006).
[153] E. S. Snow *et al.*, Applied Physics Letters **82**, 2145 (2003).
[154] Z. Wu *et al.*, Science **305**, 1273 (2004).
[155] D. Simien *et al.*, Acs Nano **2**, 1879 (2008).
[156] D. Hecht, L. B. Hu, and G. Gruner, Applied Physics Letters **89** (2006).
[157] Y. Kim *et al.*, Synthetic Metals **156**, 999 (2006).
[158] V. Skakalova *et al.*, Journal of Physical Chemistry B **109**, 7174 (2005).
[159] Y. Zhao, and W. Li, Microelectronic Engineering **87**, 576.
[160] Pedro J. de Pablo *et al.*, Advanced Materials **12**, 573 (2000).

Chapter 1

Single Walled Carbon Nanotubes

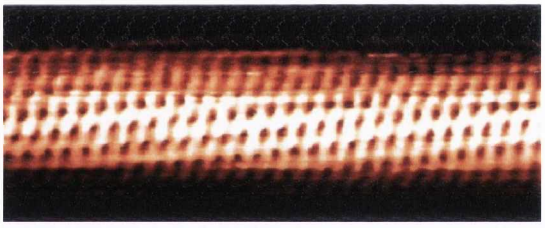

1.1 Introduction

Understanding the fundamentals of material properties is a critical platform upon which device physics and modern age electronics are built. The exploration of new nanoscale materials was made possible with the development of electron and probe microscopy techniques. Carbon nanotube (CNT) is one such material which has attracted wide spread research interest from various scientific disciplines ranging from biochemistry to surface physics. Ever since CNTs were introduced following the pioneering work of Sumio Iijima [45, 80] they have developed as promising materials in a range of applications from organic light emitting diodes [136] to transparent electrodes in solar cells [138]. These allotropes of carbon have been shown to exhibit exceptional material properties that depend on how the graphene sheet is rolled to form the CNT. Therefore controlling the synthesis of CNTs is crucial in developing these materials with predictable properties.

1.2 Geometry

Carbon nanotubes are synthesised as cylindrical nanostructures with hemispherical end caps and based on the number of cylindrical shells formed during the synthesis they are classified as single walled carbon nanotubes (SWCNT) [161] or multiwalled carbon nanotubes (MWCNT) [162]. Fig. 1.1 A and 1.1 B shows a schematic of a SWCNT and a MWCNT (with an inner and outer shell).

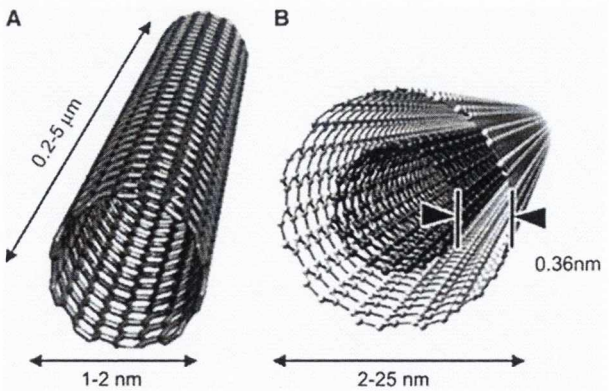

http://jnm.snmjournals.org/cgi/content-nw/full/48/7/1039/FIG1

Figure 1.1: Structural schematic of carbon nanotubes. (A) and (B) Schematic of a single walled carbon nanotube and a multiwalled carbon nanotube respectively.

A SWCNT is formed by rolling a sheet of graphene into a cylinder along an (m,n) lattice vector in the graphene plane. Depending on how the sheet is rolled, the nanotube will have a chirality described by the chiral vector C_h which can be expressed as

$$C_h = na_1 + ma_2 \qquad \text{Equation 1}$$

Where n and m are integers, a1 and a2 are the graphene lattice unit vectors as shown in Fig. 1.2. The translational vector T is along the tube axis and orthogonal to C_h and its magnitude represents the length of the unit cell of a tube. The angle between the vector C_h and the unit vector a1 is the chiral angle θ which can range from $0^\circ \leq \theta \leq 30^\circ$ and can be determined from Equation 2.

$$\theta = \tan^{-1}\left(\frac{\sqrt{3}m}{m+2n}\right) \qquad \text{Equation 2}$$

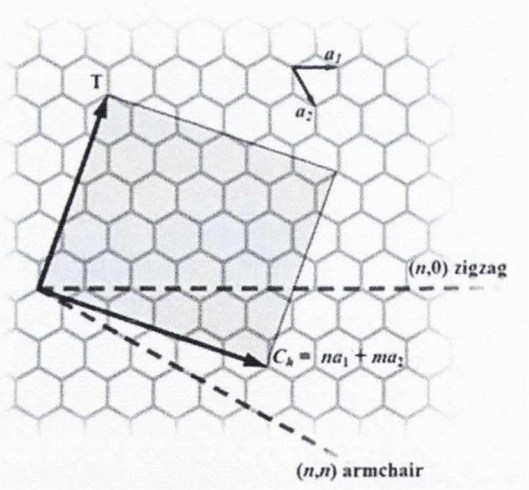

http://wpcontent.answers.com/wikipedia/commons/thumb/3/35/CNTnames.png/300px-CNTnames.png

Figure 1.2: Schematic representation of a planar graphene sheet. The chirality of the tube depends on the angle in which the graphene sheet is rolled.

The (m,n) indices determine the diameter and chirality which are the key factors in determing the electronic nature of the nanotube. SWCNTs can be either chiral (Fig. 3C) or achiral depending on the orientation of the carbon hexagons with respect to the tube axis. A molecule is said to be chiral if its mirror image is not super imposable on itself and achiral if it has a super imposable mirror image.

Armchair (Fig. 1.3A) and zigzag (Fig. 1.3B) carbon nanotube structures falls under the achiral nanotube category. Armchair nanotubes are formed when n = m and the chiral angle θ is 30 degrees. Zigzag nanotubes are formed when either n or m is zero and the chiral angle θ is 0 degrees. These structures derive their names from the circumferential pattern of the carbon-carbon bonds as shown in Fig. 1.3.

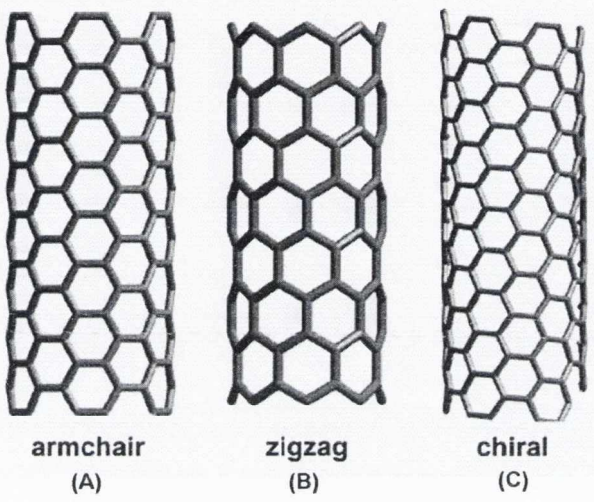

Figure 1.3: Schematic structure of the different electronic species of carbon nanotubes. (A) Armchair, (B) Zigzag and (C) Chiral carbon nanotubes.

1.3 Synthesis and Purification

The standard techniques that have been employed so far for producing CNTs are arc discharge [163] , laser ablation [164] and chemical vapour deposition (CVD) [165]. Arch discharge and laser ablation use solid-state carbon precursors to provide carbon sources needed for nanotube growth and they also involve the vaporization of carbon at temperatures up to a thousand degree Celsius. The arch discharge technique has also been extended for the large scale synthesis of CNTs by rotating the graphitic anode at high velocities and generates stable plasma [166]. CVD on the other hand utilizes hydrocarbon gases as a feed gas for carbon atoms and metal catalyst particles as "seeds" for nanotube growth that takes place at relatively lower temperatures (500-1000 degrees Celsius). The "seeds" are usually transition metal nanoparticles supported on high surface area materials like alumina. CVD technique has also been demonstrated at lower temperatures (120 degrees Celsius) in order to facilitate the growth of nanotubes on glass and plastic substrates as well [167].

Apart from the conventional CVD methodology, there have been novel approaches combined with this technique to increase the quality and throughput of the materials produced. Two such techniques are AFM lithography generated catalyst particles [167] and microwave assisted CVD growth [168]. In all the techniques discussed above the nanotubes are grown parallel to the substrate but it has been showed by Kenji Hata et al. [169] that it is possible to grow SWCNTs as vertical dense forests. Not only can the length of these tubes be tuned from 500 nm to 10 μm but these tubes are of very high quality (99%) due to the introduction of water vapour during the growth phase. During CVD growth the size of the catalyst particle plays a major role in determing the diameter of the tubes [170]. SWCNTs can also be produced by gas phase CVD process known as HiPco [171] (High pressure carbon monoxide). The growth of the tubes takes place at high pressure (30-50 atm) and high temperature (900 -1100 $^{\circ}$ C) while CO gas flows through the chamber on catalytic seeds of iron. The clusters are formed in situ when Fe is added to the gas flow in the form of Fe $(CO)_5$. Upon heating, the Fe $(CO)_5$ decomposes and the iron atoms condense into clusters. These clusters serve as catalytic particles upon which SWNT nucleate and grow (in gas phase) via CO disproportionation as shown in equation 3.

$$CO + CO \Rightarrow CO_2 + C\ (SWNT) \qquad \text{Equation 3}$$

SWNT material of up to 97% purity has been produced and rates of up to 450 mg/hr have been reported using the HiPco process. The pristine carbon nanotubes produced by the HiPco process are found to contain impurities like metal catalyst particles and amorphous carbon which limits the overall performance of there materials. In order to purify these nanotubes several techniques have been adopted ranging from organic functionalization [172] to a mild treatment with bromine [173]. Gas phase purification of SWCNTs has also been shown to remove the unwanted carbon content [174].

1.4 Electronic Structure & 1D Transport in Nanotubes

The (n, m) indices plays a pivotal role in determining the whether a nanotube is metallic or semiconducting as predicted by electronic band structure calculations. The dispersion relations [175] (Fig. 1.4) show how the electronic energy varies with the wave vector in the there different types of nanotubes. In the one dimensional energy dispersion relation, the valence and the conduction bands for all the armchair nanotubes cross at the k point and this crossing takes place exactly at the Fermi level [175]. Each curve corresponds to a single quantum sub band. The Fermi level is at E = 0, below which energy states are fully occupied, while higher energy states are completely empty. Fig. 1.4A and B show for example the electronic energy dispersion of an armchair (5, 5) and a zigzag (9, 0) nanotube respectively.

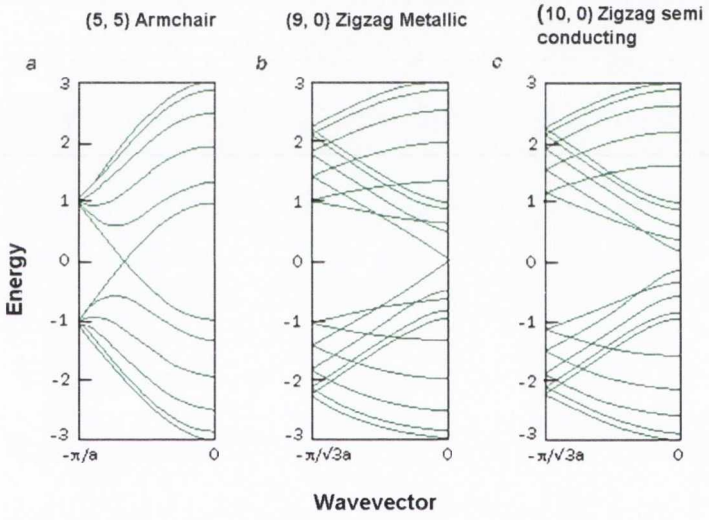

Figure 1.4: Energy dispersion diagram of single walled carbon nanotubes. One dimensional energy dispersion of (A) (5, 5) Armchair carbon nanotube, (B) (9, 0) Zigzag metallic nanotube, (C) (10, 0) Zigzag semiconducting nanotube.

In both cases a small amount of energy is needed to excite an electron into an empty higher state and such nanotubes are termed as metallic. In other words metallic nanotubes can also be considered as zero bandgap semiconductors as some electrons have access to the conduction band without the requirement of external energy. For a zigzag (10, 0) nanotube there is a finite band gap between the occupied and empty states, so this nanotube is classified as a semiconductor nanotube.

A minute increase in the diameter of the tube will therefore have a major impact on the conduction properties of carbon nanotubes. Due to the degeneracy point between the valence band and the conduction band, the armchair nanotube is considered as a zero band gap semiconductor which will exhibit metallic conduction at finite temperatures. Therefore armchair nanotubes are metallic but zigzag nanotubes could be either metallic or semiconducting. For (n,0), i.e, zigzag tubes, when n is a multiple of 3, the energy gap at k = 0 becomes zero (metallic tubes) and when n is not a multiple of 3, an energy gap opens at k = 0 (semi conducting tubes). For chiral nanotubes, in general if the difference between n and m is a multiple of 3 then the nanotubes are metallic while the others are semiconducting. The density of states (DOS) in carbon nanotubes is quantised resulting in sharp peaks known as van Hove Singularities [176] (vHSs) as shown in Fig. 1.5. The value of the DOS at the Fermi level is zero for semiconducting nanotubes as there are no electrons found in the forbidden gap while it is non zero for metallic nanotubes as shown in Fig. 1.5.

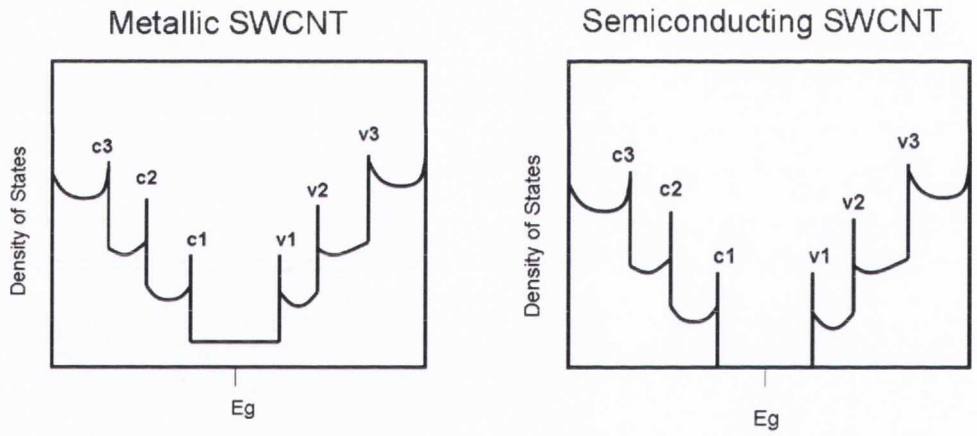

Figure 1.5: Schematic representation of the density of states of a single walled carbon nanotube.

For both semiconducting and metallic nanotubes, the energy gap depends upon the reciprocal of the nanotube diameter specified by equation 4. The term "band gap" in metallic nanotubes is applied to the energy separation for the first pair of singularities in the electronic density of metallic tubes [175]. The electronic structure and atomically resolved topography of individual SWCNTs was reported by Jeroen et al. [177] with the aid of scanning tunneling microscopy (STM) and scanning tunneling spectroscopy (STS).

They confirmed with their high resolution data that the electronic properties of the nanotubes depend on the wrapping angle and they also observed the vHSs at the onset of one dimensional energy bands. This work experimentally proved the concept that the band gap of CNTs was inversely proportional to its diameter. The Landauer formula forms the basis for understanding the transport in 1D carbon nanotubes which states that the conductance of a quasi-1D system is given by equation 4

$$G = 4e^2/h \sum_i \int_{-\infty}^{\infty} \frac{df\left[\frac{(E-E_F)}{k_B T}\right]}{dE} \delta_i(E) dE \qquad \text{Equation 4}$$

Where $\delta(E_F)$ is the transmission of the *i*th 1D subband state at the Fermi energy and df/dE is the energy derivative of the Fermi function. Conductance is thus a measure of the transmission of electrons through the entire device at the Fermi energy, broadened by the finite thermal width of the Fermi function. When the Fermi energy is in the bandgap, $\delta(EF) = 0$ and the conductance is governed by thermal activation from the tails of the Fermi function. When E_F lies within an electron or hole subband, the transmission properties of the entire device that also includes the influence of the contact resistance due to the metal electrodes determine the overall conductance. If the transport is ballistic and the tube has perfect contacts, this equation predicts a quantized conductance of $4e^2/h$ associated with each 4-fold degenerate 1D subband. Neglecting the coherence effects, the total resistance *(R)* of a nanotube device with a uniform channel can be described as shown in equation 5

$$R = R_{\text{contacts}} + R_{\text{tube}} \qquad \text{Equation 5}$$

Where the contact resistance obeys $R_{\text{contacts}} \geq h/4e2$, and for a uniform tube with diffusive scattering the resistance is given by equation 6

$$R_{\text{tube}} = (h/4e^2)(L/l) \qquad \text{Equation 6}$$

Where L is the tube length and l is the electron mean-free path for momentum relaxation, and we assume $L>>l$.

The measured device properties thus reflect the incoherent addition of the resistance of the tube and the contacts, therefore the reduction of the resistance due to the contacts and maintaining a defect free nanotube structure is vital in achieving high performance single nanotube based devices.

Materials used in this study

SWCNT materials synthesised using arc discharge was used in this study which was purchased from Iljin Nanotech, South Korea.

Acknowledgements

The image of page 14 is adapted from Wildoer et al. [178]

References

[1] S. Iijima, Nature **354**, 56 (1991).
[2] S. Iijima, and T. Ichihashi, Nature **363**, 603 (1993).
[3] C. M. Aguirre *et al.*, Applied Physics Letters **88** (2006).
[4] T. M. Barnes *et al.*, Applied Physics Letters **90** (2007).
[5] H. Dai, Accounts of Chemical Research **35**, 1035 (2002).
[6] W. Wasel *et al.*, Carbon **45**, 833 (2007).
[7] T. W. Ebbesen, and P. M. Ajayan, Nature **358**, 220 (1992).
[8] C. Journet, and P. Bernier, Applied Physics A: Materials Science & Processing **67**, 1 (1998).
[9] C. Du, and N. Pan, Materials Letters **59**, 1678 (2005).
[10] S. Jong Lee *et al.*, Diamond and Related Materials **11**, 914.
[11] S. Hofmann *et al.*, Applied Physics Letters **83**, 135 (2003).
[12] K. V. Vijay, and X. Jining, edited by K. V. Vijay, and B. K. Laszlo (SPIE, 2003), pp. 204.
[13] K. Hata *et al.*, Science **306**, 1362 (2004).
[14] A.-C. Dupuis, Progress in Materials Science **50**, 929 (2005).
[15] M. J. Bronikowski *et al.*, in The 47th international symposium: Vacuum, thin films, surfaces/interfaces, and processing NAN06 (AVS, Boston, Massachusetts (USA), 2001), pp. 1800.
[16] V. Georgakilas *et al.*, Journal of the American Chemical Society **124**, 14318 (2002).
[17] K. C. Yao *et al.*, Advanced Materials **8**, 1012 (1996).
[18] J. L. Zimmerman *et al.*, Chemistry of Materials **12**, 1361 (2000).
[19] M. S. D. Dresselhaus, G; Eklund. P.C, (Academic Press, Newyork, 1996).
[20] J. Ernesto, ChemPhysChem **5**, 619 (2004).
[21] T. W. Odom *et al.*, Nature **391**, 62 (1998).
[22] J. W. G. Wilder *et al.*, Nature **391**, 59 (1998).

Chapter 2

Atomic Force Microscopy

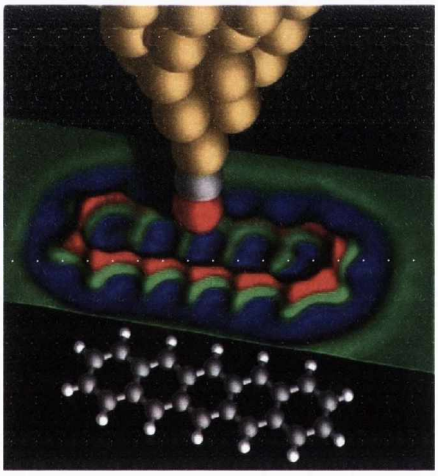

2.1 Introduction

The field of scanning probe microscopy has undergone a rapid progress ever since the invention of scanning tunneling microscope (STM) by Gerd Binnig and Heinrich Rohrer [4] nearly three decades ago. It was STM that made it possible to observe atoms for the first time in real space [4]. Moreover it paved the way to explore properties of materials down to atomic level and triggered the development of a new class of scanning probe microscopy related techniques. The STM operates primarily on the tunneling current that flows between an atomically sharp tip and a conductive surface. When the tip is brought in close proximity (~ 0.1 nm) to the sample under investigation a current in the order of a few pA to nA starts to flow between the tip and the sample depending on the applied bias. The tunneling current is exponentially dependent on the distance between the tip and the sample and responsible for the high spatial resolution of STM. STM however cannot be extended to the analysis of insulating and biological samples as a stable tunneling current and an atomically clean surface are a pre-requisite for STM operation.

This need to study samples irrespective of their electronic nature led to the introduction and invention [2] of the atomic force microscope (AFM) in 1986. AFM measures the forces involved between a lithographically defined tip and the sample instead of the tunneling current as in STM and has enabled AFM to be used in a wide range of studies from the structural analysis of dermal scales of armoured fish [179], to bangap engineering of carbon nanotubes with strain [180], to understanding the contact mechanics of fractal surfaces [181]. AFM has also made possible imaging under fluids [182] thereby facilitating the analysis of biological molecules under appropriate aqueous pH and ionic strength.

2.2 Principles of AFM Operation

In an AFM, a sharp tip is attached to the free end of a cantilever; when the tip is brought in close proximity to the specimen sample various interactions on an atomic scale takes place between the tip and the sample leading to the deflection of the cantilever. These interactions include both long range (10-100 nm) and short range (few Angstroms) forces.

The magnitude of these interactions varies as a function of probe-sample distance. A convenient way to measure forces is to convert them into deflections of a spring according to Hooke's law given by equation 1.

$$F = -kX \qquad \text{Equation 1}$$

Where F is the restoring force exerted by the material, k is the spring constant and X is the displacement of the end of the spring from its equilibrium position.The deflection of the cantilever is measured using a laser beam that is reflected from the backside of the cantilever into a light sensitive photodiode which is segmented into four quadrants. When the laser beam is deflected vertically along the top and bottom positions, there exists a bending due to the local changes in the sample topography. In the case of this movement being in the horizontal direction left and right then it produces torsion due to the lateral forces involved. The sample is scanned beneath the AFM probe using a piezoelectric motor and positioned. The piezoelement within the scanner contracts or expands in the presence of an applied voltage thereby facilitating the motion of the scanner in x, y and z directions. A schematic detailing the operation of an AFM is shown in Fig.2.1.

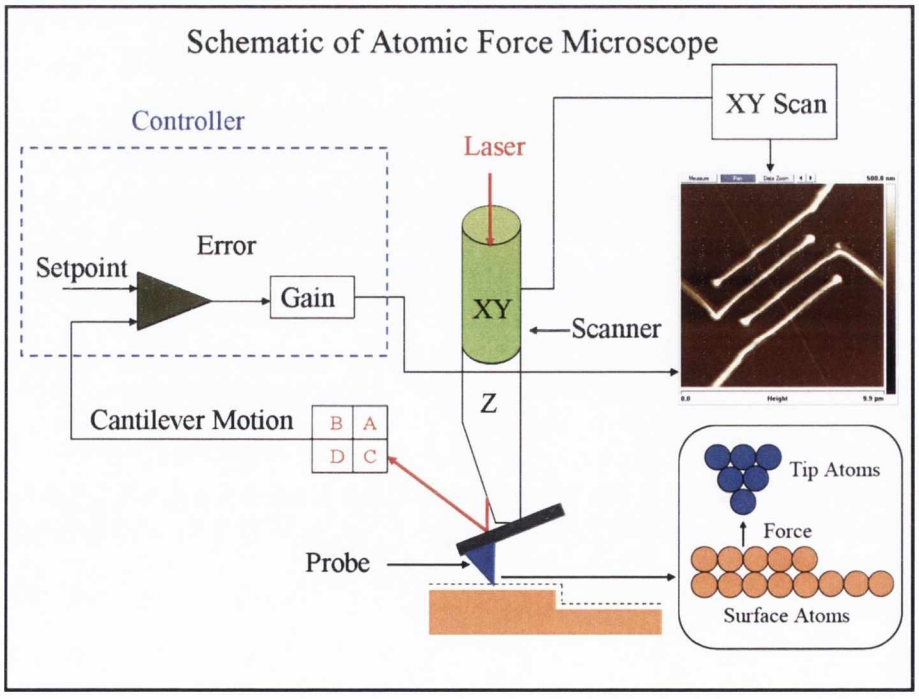

Figure 2.1: Schematic of the working principle of atomic force microscope.

2.3 Role of the Tip

The tip that is attached to the free end of the micromachined cantilever plays an important role in determing the quality of the data acquired as the lateral resolution in an AFM is governed by the shape of the tip and the geometry of the tip apex. Most commercially available probes are based on single crystalline silicon, silicon dioxide (SiO_2) or silicon nitride (Si_3N_4) tips with radius of curvature of less than 10 nanometers. As the tip raster scans across a sample it generates a 3-D map of the surface which is actually a convolution of the tip geometry and local surface topography. By being able to maintain a constant geometry a faithful reproduction of the surface is possible. The tip must also remain sturdy and sharp to allow reliable comparison of data taken during a single scan and if possible over multiple scans. A lot of effort has been dedicated towards achieving shaper tips by using focussed ion beam techniques [183] or by the attachment of carbon nanotube tips [184] to probes. Carbon nanotubes have been discussed as ideal candidates for sharp probes due to their nanometer scaled dimensions, high aspect ratio and excellent mechanical strength. Figure 2.2 shows a typical scanning electron microscopy image of various AFM tips that have been used in this study. Depending on the experiment, a tip with a suitable force constant and resonant frequency can be selected.

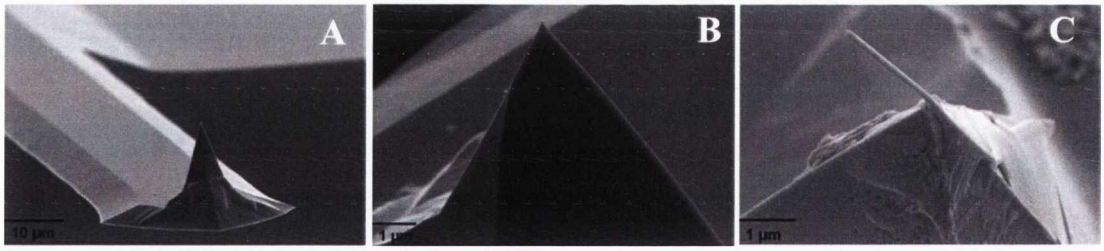

Figure 2.2: Scanning electron microscopy analysis of AFM Tips. (A), (B) and (C) are the pristine bare silicon nitride tips, tips with metal coating (Pt/Cr) and solid metal needles (silver/gallium) attached to a silicon nitride base respectively.

In electrical measurements metallic coating (Cr/Pt) can be applied to the tip while for magnetic force measurements tips can be coated with magnetic materials (Ni/Co) in order to extract magnetic information from the sample.

In certain electrical measurements where the robustness of the tip is critical boron doped diamond tips [185] have been used and this has further been extended to the usage of solid diamond tips [186] for sub nanometer electrical resolution. More recent studies [5] have demonstrated the application of non contact AFM to imaging pentacene molecules with atomic resolution by probing the short range chemical forces that are sensitive to the local electron density of states close to the Fermi level. The crucial element for this experiment was the functionalizing of the AFM tip with CO molecules, which enables the probe to look through the electron cloud and visualise the atomic backbone of an individual molecule. In addition the tip apex was etched using a focussed ion beam prior to molecular attachment to increase the sensitivity to localised forces at the apex. Hence the AFM tip plays a very vital role in describing in detail the local topographic and other relevant information pertinent to the sample under investigation.

2.4 Imaging Modes in AFM

The AFM can be used to image the sample under different scanning modes depending on the texture of the sample and the information that has to be extracted from the sample. There are three basic modes of AFM operation: contact, non-contact mode and tapping mode. The forces measured differ from one mode to another. The dependence of van der waals force as a function of distance between the tip and the sample is shown in Fig. 2.3.

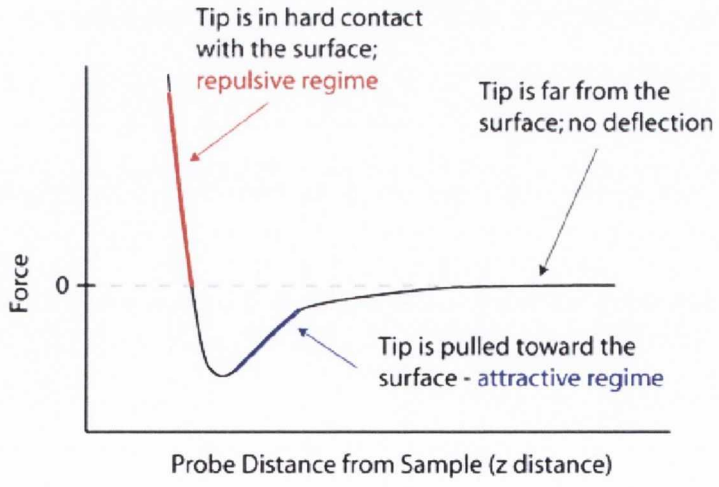

Figure 2.3: Potential energy diagram depicting the forces involved between the probe and the sample.

Contact Mode

In contact mode, also known as repulsive mode, an AFM tip makes a soft and continuous physical contact with the surface. The tip is attached to the end of a cantilever with a low spring constant, lower than the effective spring constant holding the atoms of the sample together. As the scanner gently traces the tip across the sample (or the sample under the tip), the contact force causes the cantilever to bend to accommodate changes in topography. The slope of the van der Waals curve is very steep in the contact regime. As a result, the repulsive van der Waals force balances almost any force that attempts to push the atoms closer together. In AFM this means that when the cantilever pushes the tip against the sample, the cantilever bends rather than forcing the tip atoms closer to the sample atoms. In contact-mode the tip either scans at a constant small height above the surface or under the conditions of a constant force. In the constant height mode the height of the tip is fixed, whereas in the constant-force mode the deflection of the cantilever is fixed and the motion of the scanner in z-direction is recorded.

Non Contact Mode

Lifting the probe by at least one nanometer from the sample surface, only large-range attractive interactions remain. The relevant forces are in general due to van der Waals interactions, electro- and magnetostatic interactions. Under ambient conditions there is typically a liquid surface which limits the types of information that can be obtained in non contact mode. While van der Waals forces are relatively small and capillary forces can be avoided by either choosing a sufficiently large working distance or by working on clean surfaces, electro- and magnetostatic interactions can still yield significant surface contrast to provide important information about the electrical or magnetic charge distribution in the near-surface regime of the sample. The non contact mode forms the basis for magnetic force microscopy [187], scanning capacitance microscopy [188] and electric force microscopy [31].

Tapping mode

In tapping mode-AFM the cantilever is oscillating close to its resonance frequency. An electronic feedback loop ensures that the oscillation amplitude remains constant, such that a constant tip-sample interaction is maintained during scanning. Forces that act between the sample and the tip will not only cause a change in the oscillation amplitude, but also change in the resonant frequency and phase of the cantilever. The amplitude is used for the feedback and the vertical adjustments of the piezoscanner are recorded as a height image. The important point is that the energy transferred and the duration of the interaction between the oscillating probe to the sample surface in this intermittent-contact mode is much reduced over that in the standard contact-mode of operation. This makes the technique especially interesting for the analysis of delicate soft-matter samples. It has also been found that intermittent-contact mode is more effective than non-contact AFM for imaging larger scan sizes that may involve large variations in the sample topography. The "intensity" of the intermittent-contact mode can be controlled by appropriately setting the free-vibration amplitude as well as the set-point drop in amplitude which is kept constant during scanning. Under ambient conditions, amplitudes as large as 10-100 nm are frequently used for cantilevers with resonant frequencies of 100 kHz or more. Under liquid immersions the amplitude and its drop can be set much smaller.

2.5 Conductance Imaging Atomic Force Microscopy (CI-AFM)

The CI-AFM is a very powerful and non destructive technique to characterise the local topography and the electronic properties of a sample simultaneously. In this technique the AFM tip acts like a mobile probe on the surface and is held at ground potential with a DC bias applied to the sample. The tip can also be biased for certain experiments where the voltage needs to be applied more locally. The z feedback signal is used to generate a normal contact mode AFM topographic profile and the current passing between the tip and the sample is measured using a preamplifier to generate the conductance image. A maximum bias voltage of -10 V upto +10 V can be applied to the electrode on the surface that drives current through the sample under study. A current range of 2 pA to 1 μA can be detected by the preamplifier in the CI-AFM module. The sensitivity of the preamplifier can be controlled in the range from 1 to 100 nA/V.

Conducting tips are of course required in these measurements and are usually coated with a metal coating (Pt/Ir or Cr/Pt). In addition there are solid metal tips that are used to study conductive samples (silver / gallium) as shown in Fig. 2.2B and 2.2C. In order to obtain high resolution current maps it is necessary to have tips with low force constant (less than 1 N/m) and the loading force applied to the sample should be between 0.5-15 nN in order to establish electrical contact with the sample while at the same time penetrating the viscoelastic water layer on the surface. In each experiment the loading force must be optimised depending on the sample under investigation, for instance in the case of nanotubes it is kept as low as possible so that the probe doesn't rupture the nanotube sidewalls. Figure 2.4 shows the schematic for the CI-AFM technique involving measurements on a carbon nanotube network.

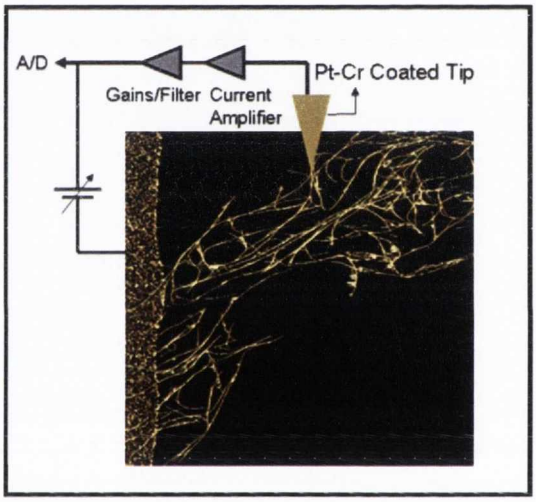

Figure 2.4: Schematic representation of CI-AFM technique. The metal coated AFM tip is made to scan a carbon nanotube network in contact mode and thereby producing a simultaneous topography and current map of the material under study.

Under normal scanning conditions the metal coating wears off the AFM probe after several scans (~10 scans) depending on the loading force applied. Furthermore tip contamination is one issue that has to be dealt with carefully so that the values obtained from the sample is not misinterpreted. A detailed investigation shows the contact resistance between the probe and the sample increases as the metal coating wears off and as the tip gets contaminated.

For these reasons, great care must be taken to guarantee the electrical quality and mechanical integrity of the AFM probe. In our case we do this by requiring the same measured contact resistance to a metal electrode between scans.

AFM Instrumentation Used In This Study

Almost all the AFM measurements in this PhD work was performed on the Veeco Dimension V system with a hybrid XYZ scanner and in certain experiments were very high resolution was needed the Veeco Multimode system with a Nanoscope IV controller was used. The scanner in the Dimension system is capable of scanning a maximum area of ~80 microns and the E-scanner in the multimode system can scan a maximum area of ~10 microns.

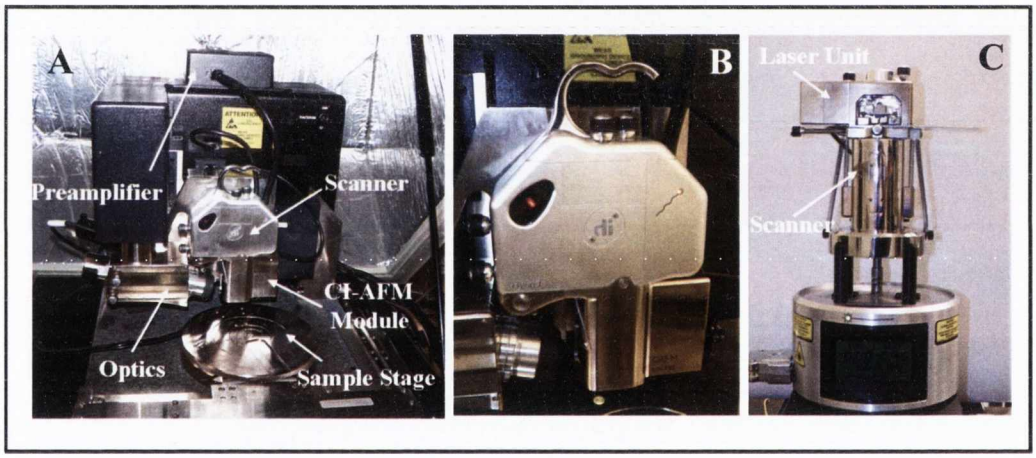

Figure 2.5: Experimental setup of the AFM instruments used in this study. (A) and (B) Dimension V experimental setup with a closer view of the AFM hybrid scanner shown in Fig. (B). (C) Experimental setup of the multimode system that has also been used in order to obtain very high resolution images in this study.

The E-scanner is more stable even after longer period of scanning and has minimal drift due to the reduced scanning area. For the CI-AFM measurements a suitable CI-AFM module is attached along with the scanner system and a special tip holder is used for these measurements. This involves attaching a special preamplifier lead into the CI-AFM module from the tip holder. Figure 2.5 shows the actual experimental setup and the AFM systems used in this work.

Acknowledgements

The image of page 23 is adapted from www.ixibo.com/in_gadgets/ibm/

References

[1] G. Binnig *et al.*, Physical Review Letters **49**, 57 (1982).
[189] G. Binnig, C. F. Quate, and C. Gerber, Physical Review Letters **56**, 930 (1986).
[3] B. J. F. Bruet *et al.*, Nat Mater **7**, 748 (2008).
[4] E. D. Minot *et al.*, Physical Review Letters **90**, 156401 (2003).
[5] R. Buzio *et al.*, Nat Mater **2**, 233 (2003).
[6] M. Raspanti, T. Congiu, and S. Guizzardi, Matrix Biology **20**, 601 (2001).
[7] H. Ximen, and P. E. Russell, Ultramicroscopy **42-44**, 1526 (1992).
[8] N. R. Wilson, and J. V. Macpherson, Nat Nanotechnol **4**, 483 (2009).
[9] K. Arstila *et al.*, Microelectronic Engineering **86**, 1222 (2009).
[10] T. Hantschel *et al.*, physica status solidi (a) **206**, 2077 (2009).
[11] L. Gross *et al.*, Science **325**, 1110 (2009).
[12] G. Xiao *et al.*, Physica C: Superconductivity **341-348**, 769 (2000).
[13] G. Kazuya, and H. Kazuhiro, edited by A. M. Terry, and A. W. Mark (SPIE, 1997), pp. 84.
[14] T. Mélin *et al.*, Physical Review Letters **92**, 166101 (2004).
[15] P. J. de Pablo *et al.*, Advanced Materials **12**, 573 (2000).
[16] A. Fujiwara *et al.*, Applied Physics Letters **80**, 1993 (2002).
[17] A. Fujiwara *et al.*, Physica B-Condensed Matter **323**, 227 (2002).
[18] P. N. Nirmalraj *et al.*, Nano Letters **9**, 3890 (2009).
[19] L. Rispal *et al.*, Japanese Journal of Applied Physics Part 1-Regular Papers Brief Communications & Review Papers **45**, 3672 (2006).
[20] M. Stadermann *et al.*, Physical Review B **72** (2005).
[21] M. Stadermann *et al.*, Physical Review B **69**, 201402 (2004).
[22] T. Heim, D. Deresmes, and D. Vuillaume, Journal of Applied Physics **96**, 2927 (2004).
[23] D. Xu *et al.*, Nano Letters **5**, 571 (200

Chapter 3

Liquid Phase Exfoliation

&

Film Formation of Single Walled Carbon Nanotubes

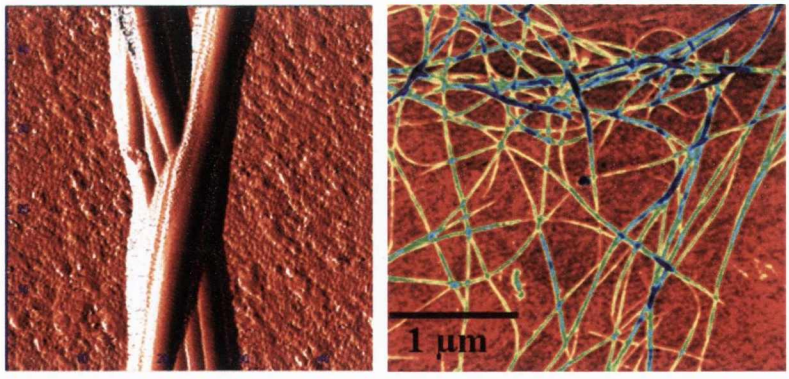

Liquid Phase Exfoliation of SWCNTs

To facilitate the study of the intrinsic properties of SWCNTs it is critical to separate the ropes or bundles of tubes produced during the synthesis into individual tubes. Single tubes can be obtained either from the bottom up synthetic approach like CVD or a top down approach involving solution phase handling processing of tubes synthesised using arc discharge or laser ablation. CVD is an expensive technique and requires specific substrate conditions during the nanotube growth phase. To be useful for many applications it is necessary to remove the tubes from the growth substrate but this typically involves solvents and results in the formation of bundles. Liquid phase exfoliation, on the other hand, is a technique that has been shown capable of exfoliating SWCNTs from bundles and ropes [88]. The nanotubes are synthesised as a raw powder containing aggregates of nanotubes which tend to form bundles of large diameter due the van der Waals attraction acting between the tubes and due to their high surface energy [190]. The availability of bundles of nanotubes limit our ability to exploit the specific properties of the nanotubes since they are composed of both metallic and semiconducting species. For this reason it is important to develop debundling strategies that do not adversely affect the intrinsic properties of the SWCNTs. Several methodologies have been adopted in recent years to effectively disperse SWCNTs by functionalising the end caps with long aliphatic amines [191] and functionalising their side walls with fluorine [192, 193].

Unfortunately, these types of functionalization strategies have been shown to modify the intrinsic properties of the SWCNTs [194]. In order to avoid disrupting the electronic and mechanical structure of the SWCNTs, milder dispersants such as surfactants [195], peptides [196] and polymers [197] were used to coat the tubes. These dispersants resulted in weak internanotube repulsion and a metastable suspension of the nanotubes in liquid media. The post analysis of the SWCNTs dispersed in water based surfactants and the conjugated organic polymers were observed to still strongly adhere to the nanotubes. The removal of these materials by water rinsing is difficult and comes at the cost of sacrificing a large fraction of the tubes.

On the other hand, organic solvents based on amides have been proven over time to act as solvents that are proficient in solvating pristine SWCNTs. Two such solvents are N, N- dimethylformamide (DMF) and N-methylpyrrolidone (NMP) will be discussed here. These solvents are non hydrogen bonding Lewis bases that provide very good solubility. Furtado et al. [198] and Ausman et al. [88] have shown that DMF and NMP can act as excellent dispersants for SWCNTs. The authors suggest that the criteria for a successful solvent are high electron pair donicity, low hydrogen bond donation parameter and high solvatochormic parameter.

It has also been shown earlier by Giordani et al. [199] that for a solvent to act as a good dispersant the solvent-nanotube interaction energy should be higher than solvent-solvent and nanotube-nanotube interaction energies. In this study SWCNTs were solubilised for electrical characterisation using NMP as the solvent of choice as it was found to solubilise the tubes well, and for which the resulting dispersions were stable for long periods (~ 4 weeks) without re-aggregation in the liquid phase. Also a decrease in the concentration always results in a downshift in the diameter distribution, suggesting a route to individual SWCNTs. In order to work with just single tubes it is necessary to reach very low concentration levels or using high speed centrifugation of high concentration dispersions for long periods of time. Although the boiling point of NMP is quite high (204.3 degrees Celsius) when compared to other solvents like DMF and toluene, it can be removed from the nanotubes by controlled annealing at high temperatures without disrupting the nanotube structure.

Synthesis of SWCNT Dispersions

An initial concentration of 1 mg/mL of SWCNTs (Iljin Tubes) in NMP was prepared. Once placed in the solvent an external energy source is necessary to drive the solvent molecules in between the nanotube bundles and mechanically exfoliate the nanotubes. Ultrasonication is the most successful approach in which a sonicating rod produces bubbles due to a cavitation process, and these bubbles have a short life time and become inserted between the nanotubes causing exfoliation. Following mechanical exfoliation the solvent molecules adsorb on the sidewalls of the tubes and efficiently prevent the individual tubes from re-bundling.

Typically dispersions were subjected to 2 minutes tip sonication (Tip amplitude: ~20%) using a high power ultrasonic tip processor (Model GEX600, 120 W, 60 kHz). This initial parent dispersion was serially diluted to produce a range of dispersions till a concentration point of ~0.00625 mg/mL. At each dilution step the dispersion was tip sonicated for 1 minute. Once a series of dispersions were prepared they were placed in a low power ultrasonic bath (Model: Ney Ultrasonik) for 4 hours. This is an important step as it allows a homogeneous concentration without actually reducing the length of the tubes as excessive ultrasonication can cause a reduction in the length also in addition to disrupting the sidewalls. It is critical to maintain the length of the tubes as it has been shown that the tube length is an important parameter in determining the overall conductivity of SWCNT based networks [156].

After the dispersions were removed from the bath sonicator they were tip sonicated with reduced tip amplitude (~10% for 1 minute). The dispersions prepared so far are subsequently centrifuged at 5500 rpm for 90 minutes after having allowed the dispersions to stand overnight.

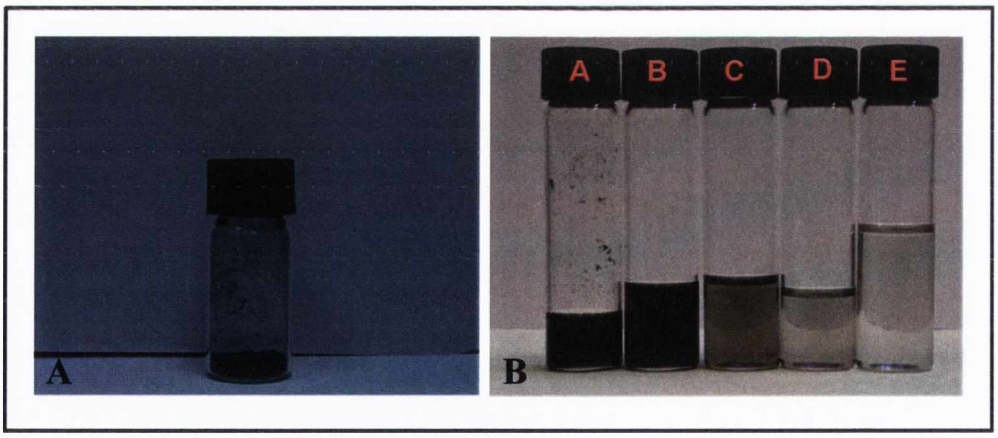

Figure 3.1: Pristine SWCNTs and the synthesized dispersions (A) Pristine Iljin SWCNT and (B) serially diluted stable dispersions as a result of a sonication cum centrifugation involved process from a starting concentration of 0.1 mg/mL (marked A in Fig. 3.1B) till a very low concentration of ~0.00625 mg/mL (marked E in Fig. 3.1B).

This last step of centrifugation removes the larger aggregates which form sediments in the bottom of the vial. These sediments are then decanted and the supernatant solutions of different concentrations are obtained as shown in Fig. 3.1B.

Formation of SWCNT Networks

Synthesizing networks based on SWCNTs has been an area of active research interest in recent years due to numerous possible applications ranging from sensors capable of detecting biomolecules [200] to flexible transparent electrodes [145, 149, 156]. Several groups have developed nanotube networks (NTNs) that are highly conductive while at the same time are highly transparent. Drop casting [201], spin coating [202], vacuum filtration [150], spray coating [203] and a combination of dip/spray coating [204] are some of the prominent techniques that have been employed to fabricate NTNs. In general to form a well interconnected NTN the concentration of the dispersion plays an important role, as a certain amount of tubes is necessary in order to establish enough conducting pathways within the random NTN. Very low concentrated solutions will have a large population of individual tubes but not enough tubes to form a network and higher concentration dispersion will have a large population of tubes but less individual tubes as shown by Giordani et al. [90]. In order to test the validity of the various strategies described in the literature for forming NTNs we tested each method based on its merits and demerits we finally adopted one technique for all our measurements.

Drop Coating & Dip Casting

To start with we experimented with the drop casting and dip coating technique. When SWCNT dispersions were drop coated onto SiO_2 substrate and imaged using a scanning electron microscope it was found that the nanotube content in the dispersion formed ring like deposits on the substrate. These ring-like patterns were found at the periphery of the substrates while the centre of the substrate was devoid of nanotubes. This behaviour is due to the outward capillary flow of the solvent leading to a pinning of the contact line of the drying solvent. This ensures that the solvent evaporating from the edge is replenished by the solvent from the centre of the droplet. Due to this droplet drying mechanism all the dispersed solute particles, nanotubes in this case are transported over to the edges as shown in Fig 3.2.

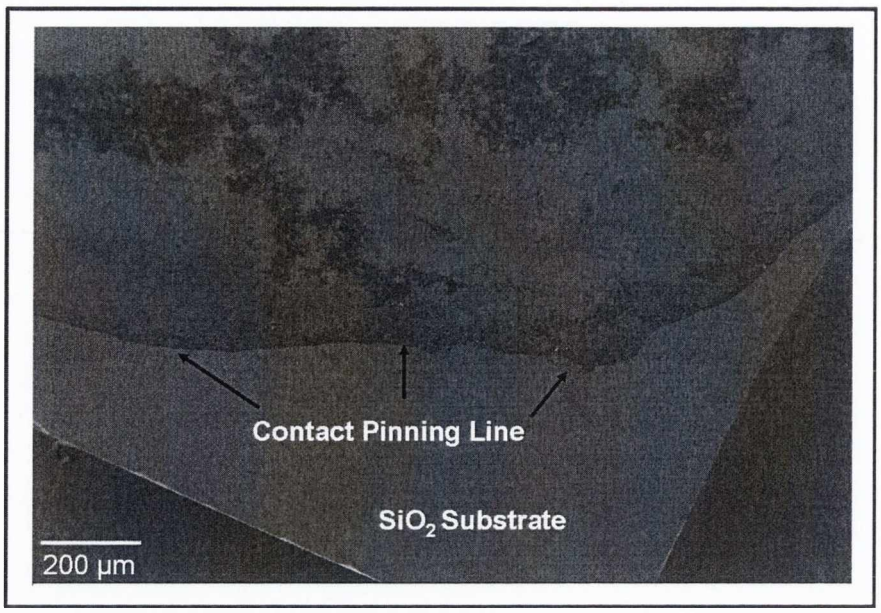

Figure 3.2: Scanning electron microscope image of SWCNT dispersion dropped on SiO_2 substrate. A contact pinning line is formed at which the nanotube content in the dispersion aggregates due to the outward capillary flow of the solvent.

Similar behaviour has been observed when a coffee drop is allowed to dry on a solid surface as studied previously by Deegan et al. [205] and this "coffee ring effect" has also been used to form metallic rings to obtain transparent conductive patterns [206]. Due to the formation of these ring-like deposits of SWCNTs it has not been possible to create a homogeneous distribution of SWCNTs, thus preventing the formation of NTNs. Similar results were obtained using dip coating on comparable solid surfaces. Hence both drop casting and dip coating technique are not suitable for NTN formation.

Spin Coating

Spin coating is another technique that has been in use for a long time especially in the area of coating polymers onto silicon dioxide surfaces for electron beam and UV-lithography. We applied this technique to try and synthesise homogeneous films of carbon nanotubes from selected solvent dispersions. The spinning speed of the chuck, viscosity of liquid medium and the spinning time are the crucial parameters that need to be tuned in order to achieve the best results.

Based on our experience it was difficult to achieve a uniform coating of carbon nanotubes over the SiO_2 surface using spin coating. This was due to the fact that there is a violent expulsion of the drop coated material on the surface once the chuck starts to spin (500 rpm, 5 mins). This resulted in the loss of valuable CNT material and the centre of the substrate was always devoid of any material following the spinning process. Hence this technique could not be adapted for our purpose of developing a homogeneous carbon nanotube based films.

Vacuum Filtration

Vacuum filtration is another approach that has been shown by previous studies [145, 149, 150, 207, 208] to form highly conductive, percolating and uniform films of SWCNTs. In our experiments we vacuum filtered the SWCNT (Iljin Tubes) -NMP dispersion of concentration ~0.025 mg/mL through a porous alumina filter paper (Pore size: 20 nm, Whatman). The filtration process is quick and the solvent drops through the pores leaving behind a well interconnected network of tubes.

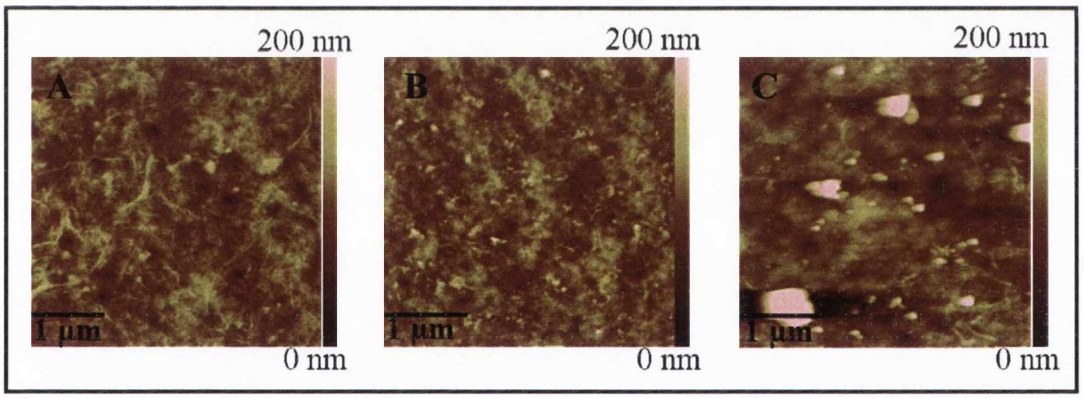

Figure 3.3: AFM analysis on nanotube re-aggregation on the porous alumina membrane after vacuum filtration. (A) Shows the re-aggregation of nanotubes on the filter paper after 5mL of dispersion (concentration ~0.025 mg/ml) was filtered through the filter paper. (B) Formation of NTNs after filtering 5 mL of dispersion (concentration ~ 0.0125 mg/mL). (C) Re-aggregation of nanotubes after filtering 6 mL of very low concentration dispersion (~0.00625 mg/mL).

We were able to control the thickness of the NTN by choosing the appropriate volume and concentration of the dispersion. The main advantage of this method is that it is scalable to large areas dictated only by the dimensions of the filter paper and the networks on the porous membrane can be transferred onto different substrates using a suitable transfer technique [209].

The average surface roughness measured on Fig. 3.3 (A), (B) and (C) were 5 nm, 15 nm and 45nm respectively. When a low concentration dispersion is filtered the NTN is very sparse and hence the surface roughness is high due to the porous alumina membrane. The direct transfer method works by placing the freshly prepared NTNs mounted on the filter paper over the substrate of choice and placing the two substrates under a mechanical press (Exerting a force of ~15 kN). The substrates are allowed to interact for 15 minutes at room temperature after which they are separated. In the case of transfer to SiO_2 substrates the force is reduced in order to avoid cracking of the substrate under the exerted normal force.

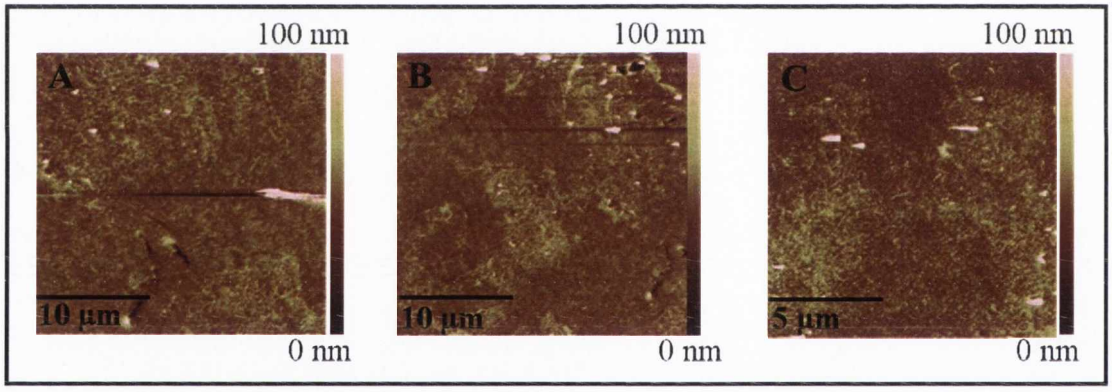

Figure 3.4: AFM analysis of NTNs on various substrates after direct transfer from the filter membrane. (A) & (B) NTN on PET after direct transfer from the alumina membrane as a result of filtering dispersions of concentration ~0.025 mg/mL and ~0.0125mg/mL. (C) NTN on SiO_2 substrate after direct transfer from a filter membrane over which 5mL of dispersion of concentration ~0.0125 mg/mL was previously filtered.

The main disadvantage we encountered with this technique was the re-aggregation of the nanotubes on the face of the filter paper. Although dispersions with very low concentrations were filtered through the membranes the nanotubes in a well dispersed phase with very low diameter distribution flocculated on the surface leading to the

formation of larger bundles. This is a serious problem as the conductivity of a NTN depends largely on the diameter distribution of the tubes within the network [40].

The NTNs formed on an alumina membrane after vacuum filtration were analysed with AFM in order to confirm the re-aggregation of nanotubes. The average surface roughness of the NTNs on poly ethylene Terephthalate (PET) substrates (Fig. 3.4A and B) was ~8 nm whereas the surface roughness in the case of SiO_2 substrate was ~5 nm. The transferred films are not homogeneous on a large scale and several discontinuities were present in the film. Furthermore the transfer of the thicker films (Fig. 3.3A & B) onto PET and SiO_2 substrates resulted only in a very small fraction of tubes being transferred, the cleanliness of the samples were also very poor and unsuitable for precise scanning probe microscopic analysis as shown in Fig. 3.4A, B, C.

Spray Coating

Spray coating is a technique that has been extensively used in the field of arts and painting to provide to a homogeneous coating. This technique has been applied in this work to form homogeneous films of nanotubes after spraying SWCNT dispersions of varying concentrations. Spray coating is a very simple technique and one of the main advantages of this technique is the ease in usage.

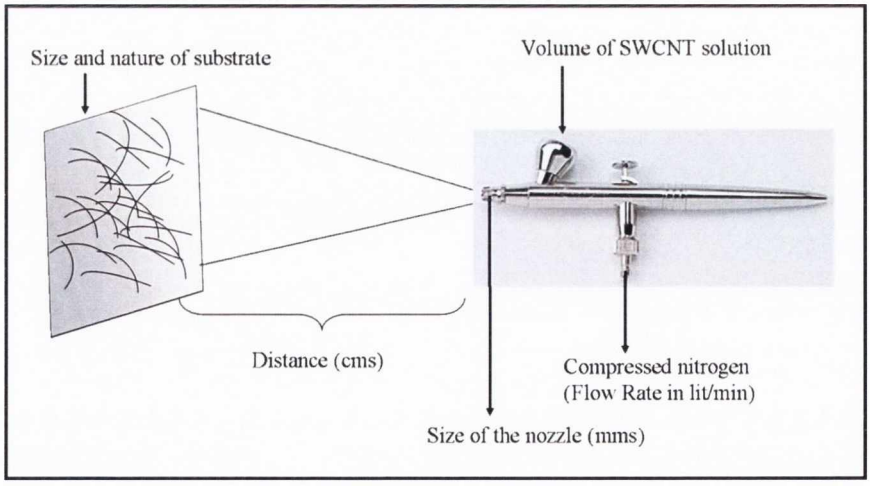

Figure 3.5: Schematic showing the spray coating technique operating procedure. The volume/concentration of the dispersion sprayed, compressed nitrogen flow rate, the nozzle-substrate distance and the size of the substrate all plays an important role in achieving percolating and well interconnected networks of nanotubes.

A spray gun (Evolution model, double action airbrush, Graphics.co.uk) is the main component of this technique which has a separate cup for pouring in the dispersion as shown in the schematic in Fig. 3.5. In the bottom of the gun there is a provision for connecting the airgun to a compressed nitrogen or air source, which is monitored in litres/minute. The compressed air pressure is usually set to 0.5 Torr which allows spraying the dispersions in a controlled manner. The volume of the dispersion sprayed directly dictates the thickness of the NTN formed. The nature and size of the substrate over which the dispersions are sprayed is equally important as increasing the size of the substrate will demand an increase in the volume of the dispersion to achieve a homogeneous coverage.

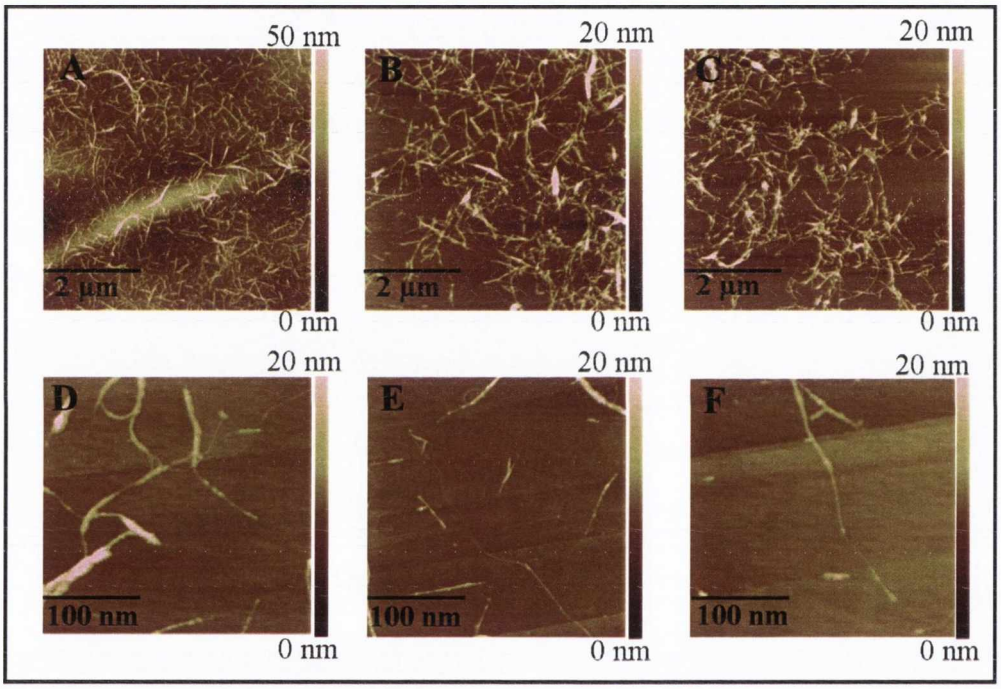

Figure 3.6: AFM analysis of dispersions of varying concentration spray coated on SiO_2 substrates. Spray coating allows us to form NTN with varying thickness by changing the volume of dispersion sprayed. (A) & (B) Thick and thin NTNs sprayed from the same dispersion concentration of ~0.025 mg/mL but by just varying the volume of dispersion sprayed from 10 mL to 1 mL allows us to form thick and thin films respectively. (C) Is a sparse NTN sprayed from a lower dispersion concentration of ~0.0125 mg/mL, by spraying 2 mL of this dispersion on SiO_2 surface forms well interconnected NTN with a lower diameter distribution regime. (D), (E) and (F) are predominantly composed of individual nanotubes (~0.7 nm) and smaller diameter bundles.

The airgun has a very fine nozzle (~ 0.2 mm) and it controls the size of the droplets formed on the sprayed substrates. A nominal distance of ~5 cm is maintained between the nozzle of the spray gun and the substrate in order to ensure that the sprayed material reaches the substrate. This technique also allows us to tune the thickness of the film depending on the volume of the dispersion sprayed. For instance we can tune the film thickness from thick films to sparse but well interconnected films by changing the volume of sprayed material (concentration: 0.025 mg/mL) from 10 mL to 1 mL as shown in Fig. 3.6A and 3.6B respectively.

This shows that by keeping the dispersion concentration constant and by varying the volume of dispersion sprayed we can achieve NTNs of desired thickness. Also as the diameter range of the bundles is found to decrease on decreasing the concentration we can achieve NTNs with lower diameter bundles with a higher population of individual tubes when compared to higher concentration dispersions.

So we chose a dispersion concentration of ~0.0125 mg/mL where there is a higher population of lower diameter bundles and at the same time enough single tubes to form percolating networks. We then sprayed 2 mL of this dispersion onto SiO_2 substrates (1cm × 1cm) and from our AFM analysis in tapping mode we observed the formation of sparse but very well interconnected NTNs suitable for our work as shown in Fig. 3.6C. In a later part of this study we have analysed specific junctions between single tubes and also the intrinsic resistance of a single tube under different conditions.

The spray coating technique also allows us the luxury to deposit single tubes or tubes with limited number of connections by spraying 0.5 mL volume of dispersions of concentrations ~0.00625 mg/mL as shown in Fig. 3.6D, 3.6E and 3.6F respectively. The other main advantage of the spray coating technique is that it is not limited by the substrate on which the NTNs are formed. A range of substrates can be used as supports for the NTNs, yielding NTNs of varying thickness and configurations on graphite, PET, glass, mica, silicon and MoS_2. Furthermore the spraying technique can also be adapted to spray surfactant based SWCNT dispersions. However, it is advisable to have a separate spray gun for each dispersant system and to clean the spray gun thoroughly with acetone after each use.

Given the advantages of the spray coating system over other deposition techniques we have adopted this technique throughout the remainder of our studies of SWCNT networks and individual nanotubes connected to electrodes.

Annealing

Once we disperse the SWCNTs in NMP and then form suitable networks using spray coating, we then focussed on the removal of NMP which tends to be tenaciously bound to the nanotubes and the underlying SiO_2 surface. In order to remove these molecules which hinder probe microscopy measurements, we used controlled annealing experiments. To start with, the sprayed nanotube networks were annealed in vacuum at 80 degrees Celsius for 12 hours and then analysed with AFM in normal tapping mode to check the cleanliness of the surface. After this annealing treatment the NMP molecules were still found to be adsorbed on the surface of the tubes and on the substrate as well as being present as big blobs shown in Fig. 3.7A. The sample condition shown in Fig. 3.7A is totally unsuitable for CI-AFM measurements, hence stressing the need for further annealing treatment. We then annealed a sample of similar dispersion concentration on SiO_2 surface for 12 hours at 250 degrees Celsius under vacuum. Analysis of this sample under AFM revealed the removal of most of the solvent content but the complete removal of the solvent molecules was not achieved as shown from Fig. 3.7B

The NMP molecules were still found to have a strong affinity for the SWCNTs and also the SiO_2 surface. Similarly prepared samples were then subjected to a high temperature anneal at 500 degree Celsius for 5 hours under a continuous flow of argon and hydrogen gas. The temperature was ramped at 100 degree Celsius for one hour. AFM analysis of samples prepared under these conditions showed the complete removal of solvent from both from the tubes and substrate as shown in Fig. 3.7C and 3.7D respectively. A sample with this degree of cleanliness is suitable for CI-AFM measurements as it will be possible to track the morphology and local electronic properties simultaneously without contamination effects to the adsorbed molecules.

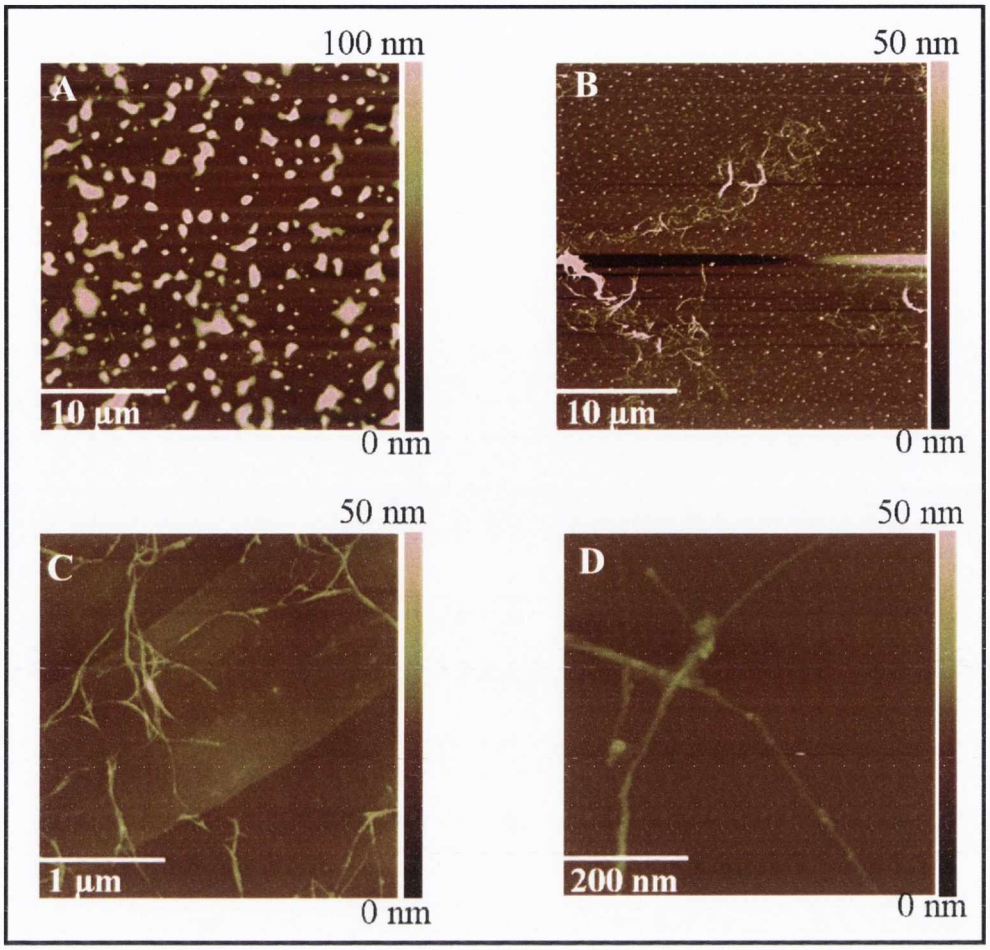

Figure 3.7: Controlled annealing experiments to remove NMP molecules adsorbed on the SWCNTs and on the underlying SiO_2 surface. (A) and (B) SWCNT networks annealed at 250 degrees Celsius and 500 degree Celsius for 12 hours and 10 hours respectively. This mild annealing treatment did not completely remove the solvent molecules as seen from (A) and (B). In order to completely remove the solvent molecules the samples were annealed at higher temperature (500 degree Celsius) under argon/hydrogen atmosphere as shown in parts (C) and (D).

Conclusion

Dispersing the single walled carbon nanotubes in appropriate solvents is a crucial factor in obtaining the optimum distribution of bundle sizes for NTN applications. Given the ultimate aim of this project is to synthesise highly conductive and optically transparent nanotube networks of smaller diameter distribution and with a larger population of individual tubes is essential. In this work we have successfully debundled SWCNTs in NMP solvent to form homogeneous networks of nanotubes using various dispersion concentrations. We have adopted the spray coating approach to tune the thickness of these homogeneous films and thereby allowing us to study the electronic behaviour of these systems in detail at a later stage. After the formation of these nanotube networks we then subjected these networks to controlled annealing experiments to remove the NMP molecules present in the network and adsorbed on the sidewalls of the carbon nanotubes. The samples prepared in this manner are well suited to electrical analysis by probe microscopy based techniques.

Acknowledgements

I would like to thank Prof Georg Duesberg for providing the furnace for the annealing experiments and Ronan Daly for his help with the SEM measurements. Thanks also to Dr Shane Bergin for useful discussions on the CNT dispersion methods and I would also like to thank Evelyn Doherty for her help in preparing films based on vacuum filtration.

The STM image of a SWCNT on page 33 was taken by Dr Zhitao Wang.

References

[1] K. D. Ausman *et al.*, The Journal of Physical Chemistry B **104**, 8911 (2000).
[2] S. Nuriel *et al.*, Chemical Physics Letters **404**, 263 (2005).
[3] J. Chen *et al.*, Science **282**, 95 (1998).
[4] E. T. Mickelson *et al.*, Journal of Physical Chemistry B **103**, 4318 (1999).
[5] E. T. Mickelson *et al.*, Chemical Physics Letters **296**, 188 (1998).
[6] A. Garg, and S. B. Sinnott, Chemical Physics Letters **295**, 273 (1998).
[7] M. F. Islam *et al.*, Nano Letters **3**, 269 (2003).
[8] V. Nicolosi *et al.*, Biomacromolecules **9**, 598 (2008).
[9] R. J. Murphy *et al.*, (SPIE-Int. Soc. Opt. Eng, USA, 2003), pp. 659.
[10] C. A. Furtado *et al.*, J Am Chem Soc **126**, 6095 (2004).

[11] S. Giordani *et al.*, J Phys Chem B **110**, 15708 (2006).
[12] D. Hecht, L. B. Hu, and G. Gruner, Applied Physics Letters **89** (2006).
[13] G. Gruner, Nanosensing: Materials and Devices **5593**, 36 (2004).
[14] G. Gruner, Journal of Materials Chemistry **16**, 3533 (2006).
[15] G. Gruner, Scientific American **296**, 76 (2007).
[16] J. A. Bardecker *et al.*, Journal of the American Chemical Society **130**, 7226 (2008).
[17] C. Stéphan *et al.*, Synthetic Metals **108**, 139 (2000).
[18] L. Hu, D. S. Hecht, and G. Gruner, Nano Letters **4**, 2513 (2004).
[19] H. J. Jeong *et al.*, Carbon **44**, 2689 (2006).
[20] Y. I. Song *et al.*, Journal of Colloid and Interface Science **318**, 365 (2008).
[21] S. Giordani *et al.*, Journal of Physical Chemistry B **110**, 15708 (2006).
[22] R. D. Deegan *et al.*, Nature **389**, 827 (1997).
[23] M. Layani *et al.*, Acs Nano **3**, 3537 (2009).
[24] L. B. Hu, D. S. Hecht, and G. Gruner, Applied Physics Letters **94** (2009).
[25] L. B. Hu *et al.*, Applied Physics Letters **94** (2009).
[26] P. N. Nirmalraj *et al.*, Nano Letters **9**, 3890 (2009).

Chapter 4

Tuning the Contact Resistance between Single Walled Carbon Nanotubes & Metal Electrodes

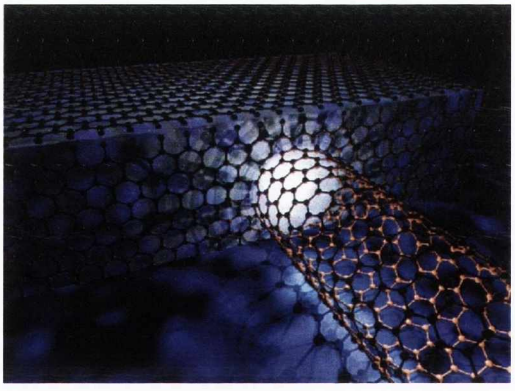

I. Introduction

The electrical interface between a single walled carbon nanotube (SWNT) and a metal electrode has been an area of intense research in recent years. In particular, Schottky barriers are known to exist whenever electrical contact is established between a semiconducting nanotube and a contact metal, which arises due to charge transfer between the SWNT and the contact metal. The presence of such barriers is a major obstacle to the facile use of these materials in electronics applications, such that the inherently attractive properties of SWNTs such as ballistic conduction [99, 100], cannot be easily exploited. In the design of any one-dimensional device structure using SWNTs it is imperative to understand the origins of the Schottky barriers that form between the SWNT and the contact metal electrode. In this regard, the chemical potential of the contact metal that serves as the electrode is critical to achieve transparent electrical contacts and the work function (φ) of the metal electrode itself can be influenced by the adsorption of molecules such as oxygen [210].

Different metals ranging from Pd [98, 99], Pt [101] , Sc [211], Y [212] and Ti [213] have been investigated as potential contact materials. Quantum mechanical density functional calculations have shown Ti to achieve ohmic contacts on both metallic and semiconducting tubes due to the formation of strong chemical bonds with the carbon atoms. However Ti is known to easily oxidise on exposure to air such that these contacts tend to degrade over time. On the other hand, palladium in particular has been shown to eliminate the contact barriers with semiconducting nanotubes due to its high work function and excellent wetting interactions with the nanotubes [100]. Numerous strategies have been described in the literature to optimise and evaluate the properties of the contacts between SWNTs and metals. Rapid thermal annealing [118], electroless metal deposition [119] and Joule heating [122, 123] have been performed to minimize the contact resistance between the metal of choice and the nanotube. In this study we present a local nanoscale analysis of the issues affecting the contact resistance between two widely used metal electrodes; Pd and Ti/Au on metallic and semiconducting SWCNTs using conductance imaging atomic force microscopy (CI-AFM) [39, 40, 194].

II. Experimental Setup

SWCNTs synthesised by the arc discharge technique (Iljin Nanotech arc discharge tubes) were dispersed in N-methylpyrolidone (NMP), an organic solvent that has been shown before to successfully exfoliate carbon nanotubes in the liquid phase [88, 199]. The nanotube dispersions were spray coated onto silicon dioxide substrates (300 nm oxide thickness) and patterned by standard UV-lithography techniques. The metal (Pd and Ti/Au) was thermally evaporated onto the patterned SiO_2 substrates and the thickness of the metal in each case was ~ 25 nm. In the case of Ti/Au, Ti (5 nm) was used as an adhesion layer which was then passivated with 20 nm of Au. The underlying Si wafer was degenerately doped through which the gate voltage was applied. The samples were then subjected to controlled annealing (500 degrees Celsius for 5 hours under Ar/H_2 ambient) in order to remove the NMP molecules adsorbed on the tubes and on the respective metal electrodes.

Using this sample configuration it is possible to discriminate between and selectively analyse metallic and semiconducting tubes within the sample by applying a gate voltage. The application of backgate (the silicon wafer acts as the gate electrode) voltage sweeps carriers from the semiconducting tubes thereby turning them off in CI-AFM images, such that only the remaining metallic tubes are visible.

III. Results and Discussion

Contact Resistance due to the Conductive Probe.

CI-AFM is a two contact electrical measurement and so meaningful data is possible only if you guarantee that the resistances associated with each contact remains fixed during the course of the measurement. This requires that three conditions are met. Firstly, the deposited electrical contact to the network must have low resistance and remain stable during the measurement. Secondly, the resistance between this contact and the metallised probe must be very small (few hundred ohms or less). Finally, the resistance between the metallised probe and the SWCNT target must be constant.

The latter requires that the probe metal coating does not wear away and that the application of a fixed set-point force results in the same measured current. Great care must be taken to insure all three conditions are met. In contact mode in order to establish electrical contact the tip must penetrate any contamination layers present on the samples, and there is a high probability for the metal coating to degrade or for the probe to become contaminated in the process. This leads to a higher contact resistance between the tip and the sample, and if wear is severe it may lead to the tip having multiple contacts with the nanoscale material. In experiments involving soft materials it is advantageous to use tips with force constants less than 1 nN to reduce the possibility of sample damage and to achieve high resolution images.

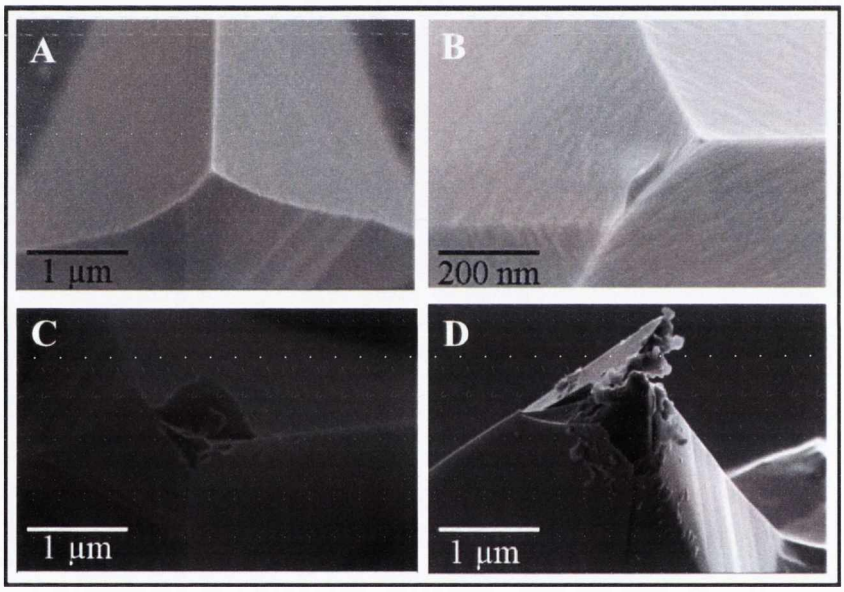

Figure 4.1: SEM images of metal coated tips as a function of number of scans. (A) Clean Pt/Cr tip prior to scanning in CI-AFM mode. (B), (C) and (D) SEM topographs of the Pt/Cr probes after 5, 15 and 25 scans respectively. The loading force was kept constant at ~0.5 nN throughout the measurements. The contact resistance between the tip and the biased electrode on the substrate increases as the metal coating wears off and as the probe gets contaminated.

Fig. 4.1A shows a SEM image of a pristine Pt/Cr tip prior to imaging in CI-AFM mode. The metal coating on the probe eventually peels-off following scanning for long periods. Fig. 4.1B, C and D are the SEM topographs of the Pt/Cr tip after 5, 15 and 25 scans respectively.

The initial contact resistance measured between a clean tip and the deposited electrode; Ti/Au and Pd was about 400 Ω and 100 Ω respectively. In order to ensure stable contacts and to check the quality of the tip the contact resistance between the tip and the electrode was re-measured prior to each scan.

Selective Analysis of Metallic & Semiconducting Tubes.

Individual and isolated SWNTs were first located by AFM in tapping mode and the diameter of the tube was verified to be between 1.2 and 1.8 nm. Note that only individual tubes are considered here as SWCNT bundles (identified by their large diameters) contain mixtures of metallic and semiconducting tubes that complicate the analysis.

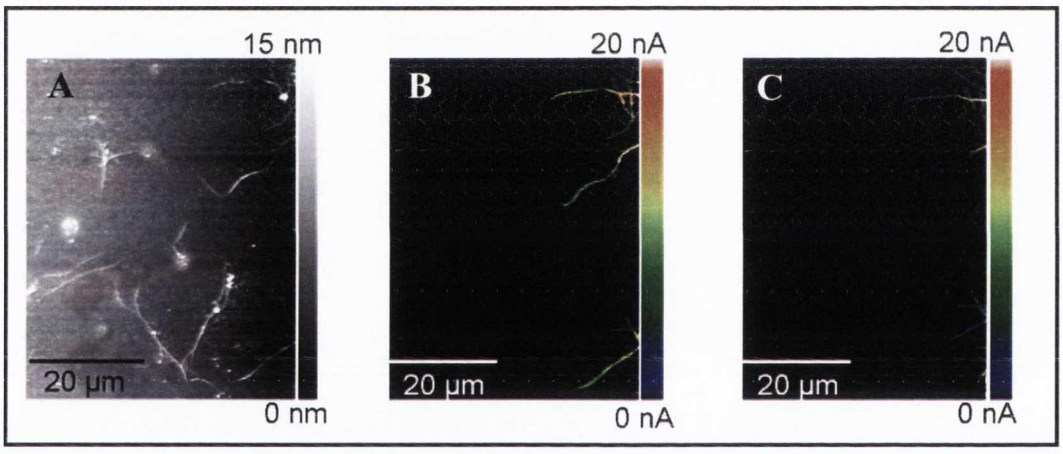

Figure 4.2: Selective analysis of metallic and semiconducting tubes via applying a gate voltage. (A) Topography of a random nanotube network connected to the electrode on the right (not shown in image). (B) Current map of the same network on applying a bias voltage of 15 mV. The tubes that are connected to the electrode turn on after applying a bias voltage thereby highlighting the tubes that are electrically well connected to the network. (C) On applying a gate voltage of + 2 V, the semiconducting tubes are turned off and only the metallic species is visible in the current map. On turning off the gate voltage the current conduction is restored in the semiconducting tubes as well.

Once an individual tube was located close to the electrode the AFM was switched to the CI-AFM mode and a very small bias (0.5 – 5 mV) was applied to the electrode to check the electrical connectivity between the electrode and the nanotube.

After verifying that the nanotube was conductive a gate voltage of + 2 V was applied, which rendered the semiconducting tubes non-conducting due to their intrinsic p-doping, and thus allowing CI-AFM to exclusively image the metallic tubes. This technique has been shown previously by Stadermann et al. [39] to selectively analyse metallic and semiconducting tubes within a random network and a typical example is shown in the backgating experiment in Fig. 4.2. An important advantage of this technique is that it is non destructive and by switching off the gate voltage the semiconducting tubes and the regions connected by the semiconducting tubes are turned on again.

Titanium / Gold as Contact Electrode

To start with we carefully analysed individual tubes connected to Ti/Au electrodes. After identifying the electronic nature of the tube connected to the electrode we carefully analysed the resistivity along the tube and the associated contact resistance due to the electrode.

Figure 4.3A shows a typical example for that found in the case of a metallic tube attached to a Ti/Au electrode. By tracing the current map along the length of the well resolved nanotube (Fig. 4.3B), it is possible to estimate the resistivity of the tube itself and by measuring the resistance at zero length an estimate of the contact resistance due to the leads can be acquired.

The resistivity (ρ) can be calculated from equation 1, where R (d) is the measured resistance at any point d along the length of the tube, Rc is the contact resistance, and A is the cross-sectional area of the tube calculated from its measured diameter assuming a cylindrical shape

$$R(d) = Rc + \rho (d/A) \qquad \text{Equation 1}$$

Using this equation we calculate the resistivity of the pristine metallic tube connected to the Ti/Au electrode in Fig.4.2A to be $1.41*10^{-8}$ Ωm from the slope of the R(d) vs. d curve and the measured diameter of 1.6 nm obtained from the topographic analysis. This resistivity compared favourably with resistivity values of those previously reported by Li et al. [94] and Kim et al. [214].

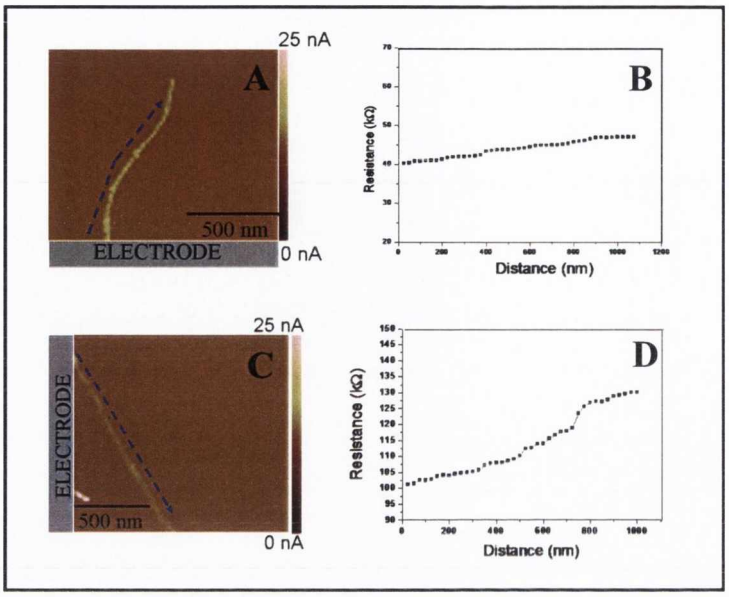

Figure 4.3: Contact resistance analysis of metallic and semiconducting SWCNT contacted to Ti/Au electrodes. (A) & (C) Current map of an individual metallic and semiconducting tube connected to the electrode. (B) & (D) Analysis of the contact resistance of the pristine metallic and semiconducting tube. (Scanning conditions: V_{bias}: 2 mV, preamplifier sensitivity; 100 nA/V).

The intercept in the data in Fig. 4.3B reveals a contact resistance at the Ti/Au electrode of 40.2 kΩ. This is an exceptionally low contact resistance, demonstrating that contact processing and solvent removal is very effective when compared to previous values of approximately 100 kΩ reported for Ti/Au- metallic nanotubes contacts [124, 215]. Likewise we can calculate the resistivity and contact resistance for the semiconducting nanotube in Fig 4.3C connected to the same Ti/Au electrode, to yield values of 6.64 * 10^{-8} Ωm and 96.86 kΩ (calculated from the black trace of Fig 4.2D), respectively, both of which are larger than that found for the case of metal SWCNTs, but comparable to the best values ever reported for semiconducting tubes.

Local Point Annealing

In order to minimise the contact resistance between the metal electrode and the nanotube we then performed a local point annealing treatment involving the application of large but controlled bias voltage using the AFM tip to the region of the electrode where the

SWNT is connected. This treatment is expected to produce local heating that might help optimise the contact resistance with the electrode. The AFM tip was approached with a bias of + 6V applied on it and using the point and shoot capability of our AFM system we were able to specifically place the tip on the electrode where the nanotube was connected. After applying a quick pulse the tip was withdrawn and re-engaed in contact mode (held at ground potential) and a low bias of 2 mV was applied to the nanotubes through the Ti/Au electrode. Changes in resistance was analysed as shown in Fig. 4.4A (red trace) and Fig. 4.4B (red trace). As a result of this 6 V pulsing procedure the contact resistance of the metallic tube was found to drop by ~12 to ~28 kΩ, whereas the resistivity or the slope of the current trace remained essentially unchanged.

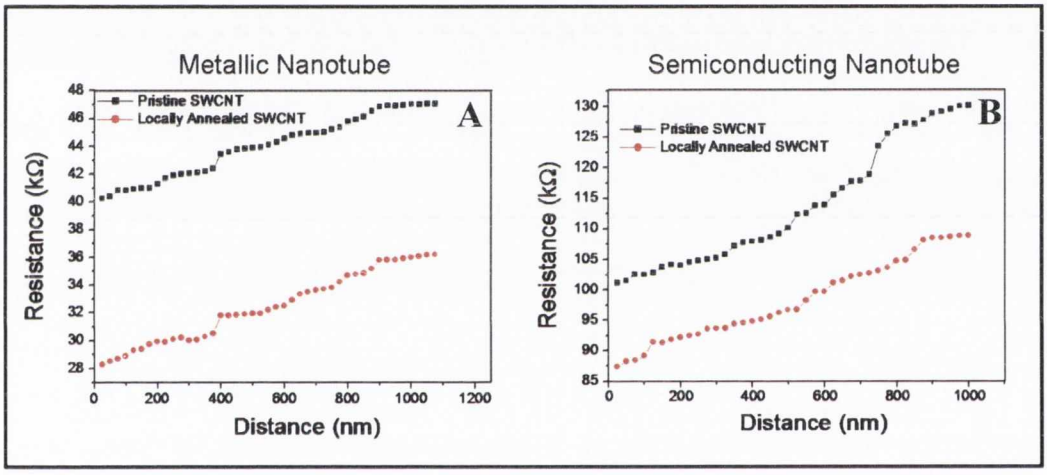

Figure 4.4: Reduction of contact resistance as a result of local pulsed annealing via the conductive AFM tip. (A) Comparative analysis of the local resistance changes along a metallic nanotube before and after local annealing experiment. (B) Local resistance analysis between a pristine semiconducting nanotube and comparing that data with the change in resistance after local pulsed annealing. A bias of 6 V was applied in both cases through the AM tip in order to reduce the contact resistance between the metallic/semiconducting tube and the Ti/Au electrode.(Scanning conditions: V_{bias}: 2 mV, preamplifier sensitivity; 100 nA/V).

Similar measurements were performed on individual semiconducting tubes connected to Ti/Au electrode as shown in the current map (Fig. 4.3C). After pulsing, the contact resistance between the tube and Ti/Au was found to decrease by ~10 kΩ (red trace of Fig. 4.4B).

Based on these results it is clear that it should be possible to tune the contact resistance by controlling the magnitude or the duration of the pulse. The calculated contact resistance between the pristine/pulse- annealed metallic and semiconducting tubes connected to the Ti/Au electrode clearly shows that the contact resistance between the metal electrode and the SWCNT is significantly reduced as a result of local pulse annealing treatment.

Palladium as Contact Electrode

Having completed the analysis of local point annealing on metallic/semiconducting nanotubes connected to Ti/Au electrodes we now compare this behaviour with Pd electrodes. Samples consisting of Pd electrodes were prepared in the same fashion as that for Ti/Au electrodes and individual nanotubes attached to electrode were identified with the AFM in tapping mode and later a detailed CI-AFM study including a backgating analysis was undertaken.

Both metallic and semiconducting tubes were analysed before and after local pulse annealing (using 6 V as the pulsing voltage) and the resistivities and contact resistances were calculated before and after pulsing. Fig. 4.4A shows the current map of a pristine metallic tube connected to the palladium electrode as traced from the current pathway shown in Fig. 4 5B (black trace).

After applying a pulse of 6 V to the electrode, the contact resistance decreases by ~ 7 kΩ. Similarly the contact resistance was observed to decrease by ~10 kΩ for a semiconducting tube after local pulsed annealing. Both these data (pristine and post annealing) was acquired by applying a bias voltage of 1 mV. Furthermore the mean intrinsic resistivity of a pristine individual metallic tube connected to the Pd electrode before and after local annealing was $\rho = (1.3 \pm 0.4) \times 10^{-8}$ Ω m and $(9.5 \pm 0.3) * 10^{-9}$ Ω m respectively. Likewise the mean intrinsic resistivity of a semiconducting tube connected to Pd electrode before and after pulse annealing was $(3.2 \pm 0.5) * 10^{-8}$ Ω m and $(1.02 \pm 0.5) * 10^{-8}$ Ω m respectively. Based on these results it is clear that it should be possible to tune the contact resistance by controlling the magnitude or the duration of the pulse.

Figure 4.5 shows the results of a systematic study in which the effect of the magnitude of the voltage pulse was studied for a metallic tube (shown in Fig. 4.6A) connected to a Ti/Au and Pd electrode. The resistance was observed to gradually decrease as the pulse voltage was increased from 1 V to 7 V.

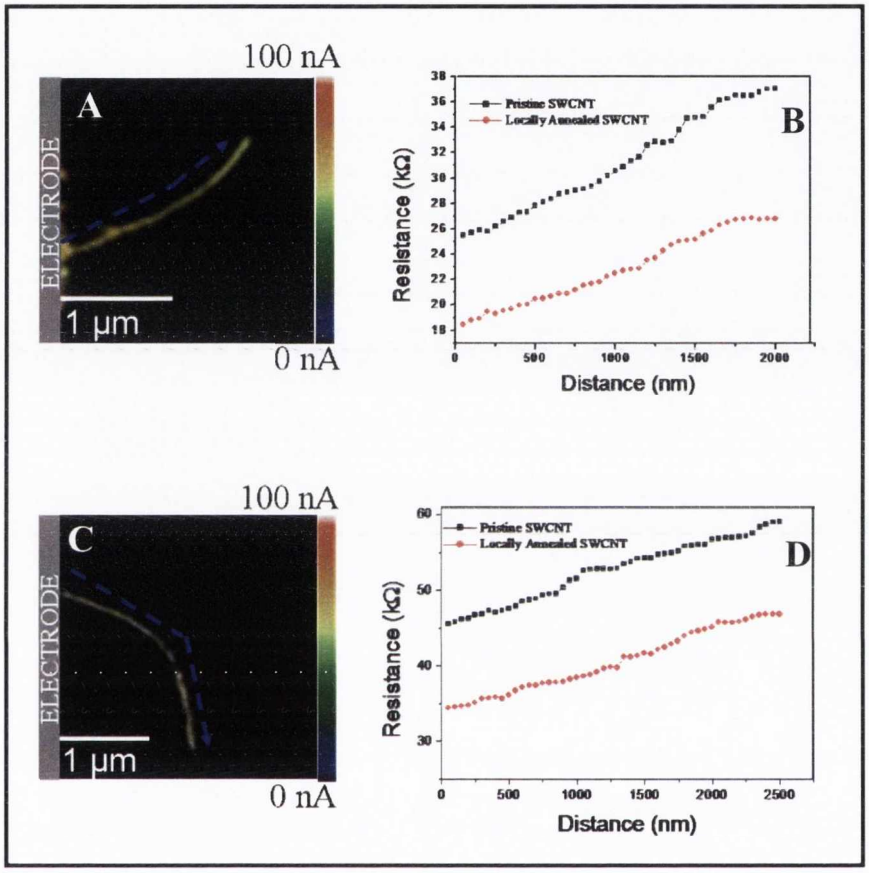

Figure 4.5: Contact resistance analysis of metallic and semiconducting SWCNT contacted to Pd electrodes. (A) & (C) Current map of an individual metallic and semiconducting tube connected to the electrode. (B) & (D) Analysis of the contact resistance of the pristine tube (black trace) and the same tube after subjecting to local annealing (red trace) by applying 6 V via the metallic tip on the Pd electrode for metallic and semiconducting tubes respectively. (Scanning conditions: V_{bias}: 1 mV, preamplifier sensitivity; 100 nA/V).

Above 6 V the contact resistance was observed to saturate and applying more than 7.5 V led to the disintegration of the tube. Similar results were also observed for semiconducting tubes; except that in each case the saturation level of the contact resistance was higher than that observed for metallic tubes.

After each voltage pulse the resistance values plotted in Fig. 4.6 were obtained from the intercept of the current trace using a bias of 2 mV. For each case the duration of the applied voltage pulse was ~2 seconds. Increasing the pulse duration and decreasing the applied voltage, e.g. 10-60 seconds at biases of 1-3 V, proved unsuccessful as the metal coating on the tip degraded rapidly for long pulse durations, making the subsequent resistance measurements unreliable. To keep track of this problem the resistance of the probe tip was constantly measured against a separate reference surface electrode of known resistance.

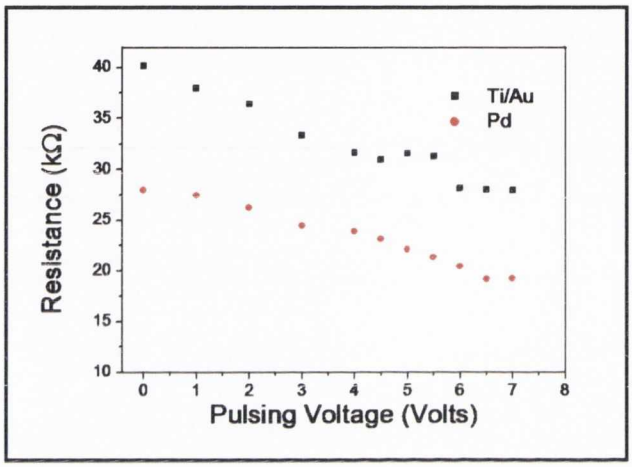

Figure 4.6: Contact resistance analysis as a function of the pulsing voltage. Analysis of the contact resistance along a metallic SWCNT connected to a Ti/Au (black trace) and Pd (red trace) electrode recorded after the application of increasing higher voltage pulses. The resistance is observed to decrease in steps from ~40 kΩ to ~28 kΩ as the pulsing voltage is increased from 1 V to 7 V after which the effect saturates and on application of > 7.5 V resulted in the degradation of the tube.

All the resistance traces were recorded at a constant bias voltage of 2 mV after the application of the voltage pulse. Optimizing the loading force is essential for reliable CI-AFM measurements. The loading force has to be high enough to penetrate the contamination layer between the tip apex and the sample under investigation to establish electrical contact. We analyzed the contact resistance between a metallic nanotube connected to a Pd electrode as a function of loading force while pulsing the electrode at 6 V for 2 seconds as shown in Fig. 4.6 (black trace). The contact resistance of the tube was subsequently analyzed at a lower loading force of 0.5 nN with a bias voltage of 4 mV.

The contact resistance was observed to gradually decrease as we gently increased the loading force. A minimum contact resistance of ~ 13 kΩ was obtained when a loading force of ~1 nN was applied.

A further increase in loading force resulted in a slight increase in contact resistance followed by an abrupt increase for loading forces above 2 nN. SEM analysis revealed that the abrupt increase is associated with a degradation of the metal coated tip as shown in the inset in Fig. 4.7. A new probe used to continue the pulsing experiment (6 V, 2 sec) but starting from an initial loading force of 1 nN is shown as the red curve in Fig. 4.7. Clearly, the result is the same as the original experiment and points to the catastrophic breakdown of the tip at higher loading. To check if the contact had actually improved despite breakdown of the probe, we examined the resistance with a third probe showing a value that corresponds to the minimum value in Fig. 4.7. These data indicate that contacting the electrode at higher loading force (>2 nN) only results in the degradation of the tip and does not in any way improve the contact resistance. The red trace in the plot results from engaging a new tip at a starting loading force of 1 nN and the contact resistance is stable until ~2 nN after which the tip degrades rapidly resulting in higher contact resistance values.

Optimization measurements on metallic/semiconducting nanotubes connected to a Pd electrode showed similar behavior. Consequently, throughout the remainder of the study we used pulsing conditions of 6 V for 2 seconds under a loading force of ~1 nN to achieve the best contact resistance values. To compare the effect of the local annealing treatment on the two different metal electrodes used in this study we performed a statistical analysis of the contact resistance of metallic/semiconducting tubes connected to Pd and Ti/Au electrodes before and after pulsed annealing.

We then extracted the mean contact resistance as shown in Table 1 and for which at least twenty tubes were measured in each case. Table I shows that the mean contact resistance of a metallic tube connected to Ti/Au decreased by ~15 kΩ after the pulse annealing treatment, while that for a semiconducting tube connected to Ti/Au showed a reduction of ~20 kΩ. The corresponding data for metallic and semiconducting tubes contacted by the Pd electrode before and after the pulse annealing revealed decreases of ~ 15 kΩ and ~22 kΩ, respectively.

The optimised values shown in Table 1 are among the lowest contact resistances ever reported for SWCNTs.

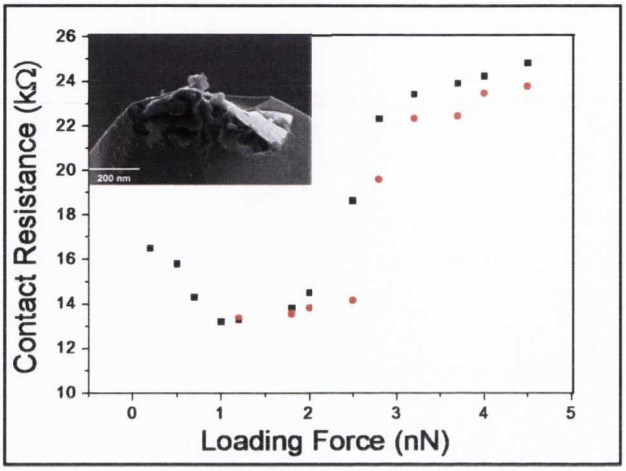

Figure 4.7: Analysis of the contact resistance between a metallic tube and Pd electrode as a function of loading force. The measurements were obtained while applying a pulsing voltage of 6 V. The contact resistance decreases gradually as the loading force is increased and the minimum contact resistance is attained around 1 nN after which the contact resistance increases rapidly (as seen from black trace) due to tip degradation as shown in the scanning electron micrograph in the inset.

Metal Electrode	Contact Resistance (kΩ)			
	Metallic		Semiconducting	
	Pristine	Annealed	Pristine	Annealed
Ti/Au	(40 ± 2.5)	(25 ± 2.5)	(105 ± 4.8)	(85 ± 3.6)
Pd	(25 ± 2.5)	(11 ± 1.6)	(54 ± 5.4)	(32 ± 3.1)

Table 1: Results from the statistical analysis of the contact resistance of pristine / pulse annealed metallic and semiconducting tubes contacted by Ti/Au and Pd electrodes.

To determine whether this pulse annealing treatment resulted in a permanent enhancement we investigated the stability of the contacts over time as shown in Fig. 4.8. The optimized Pd contacts did not vary by more than 5 % during a five month period, and can be largely ascribed to changes in the scanning conditions caused by the use of different metallic coated tips.

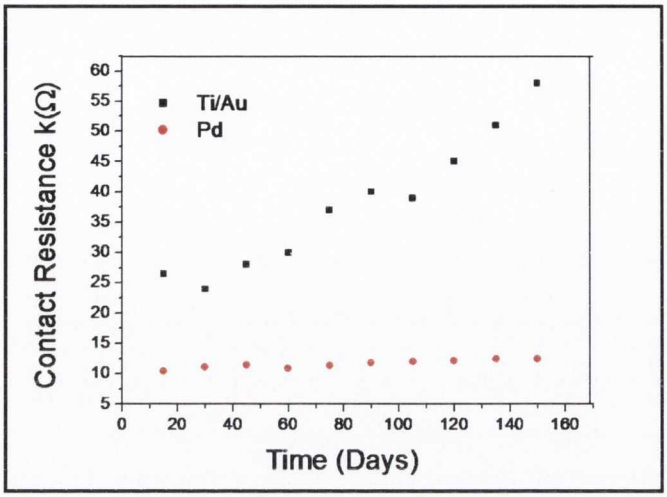

Figure 4.8: Analysis of contact resistance as a function of time. The plot shows the contact resistance for metallic nanotubes contacted by Ti/Au electrode (black curve) and Pd electrode (red curve). The contact resistance was found to increase for metallic annealed nanotubes contacted by Ti/Au electrode when measured periodically over a time period of 150 days. In contrast we did not measure any significant change in the contact resistance of Pd contacted metallic annealed tube over the same time period.

Moreover, Pd contacts that were improved by using sub-optimal pulse conditions retained the same contact resistance over time, indicating that it is possible to tune the contact resistance at any level in between the initial and optimized levels. In contrast, we found a steady increase in the contact resistance for tubes connected to the Ti/Au electrode regardless of whether the contacts were optimized (See Fig.4.8).

IV. Conclusion

There are several important outcomes from this work. First, Pd electrodes are superior to Ti/Au independent of the electronic nature of the nanotube. This is consistent with previous literature results [99, 100, 216] and has been attributed to better wetting properties of the Pd contacts and in the case of semiconducting tubes a larger work function (5.12 eV vs. 4.33 eV) that minimizes the influence of Schottky barrier formation.

The optimised contact resistance measured for metallic nanotubes contacted by a Pd electrode as a result of local pulsed annealing was ~ 11 kΩ and is comparable to previously reported values of ~15 kΩ reported by Javey et al. [99] and much lower that the values reported by Woo et al. [123] of ~100 kΩ who used a pulse annealing method where the current was passed along the entire metal electrode. This shows the advantages of our CI-AFM pulse technique and may indicate that the application of a local force is also important in helping optimise the contact.

We speculate that the combination of Joule heating and pressure is important in assisting in the formation of chemical bonds for achieving good electrical contacts. Significantly, we find that optimized semiconductor nanotube contacts with Ti/Au resulted in a much smaller decrease in contact resistance (15 %) compared to Pd (45 %), the latter yielding values that are only a factor of three larger than the very best contacts with metallic tubes (33 kΩ vs 11 kΩ). These results show that the optimization process leads to an effective collapse of the Schottky barrier so that it is possible to tunnel through the remnant barrier with minimum resistance.

The enhanced performance of Pd is likely due to the better band alignment given its larger work function and the fact that the present tubes are p-type doped (see Fig. 4.2). The stability of the Pd contacts is also striking compared to Ti/Au. The Joule heating associated with the optimization process may also promote specific chemical bonding interactions that have been predicted between Pd and carbon nanotubes [123]. The noble character and enhanced wetting properties of Pd on nanotubes make it very resistive to oxidation. In contrast Ti is chemically more reactive in air and even the deposited 20 nm of gold on top of the Ti layer, which is typical in Ti device contacts, cannot prevent slow oxidation and the deterioration of the contact.

Although Pd has been projected as one of the best contact materials for carbon nanotubes from previous extensive studies, we have demonstrated from our work yet another simple but scalable technique based on local point annealing using an AFM tip to effectively reduce the contact resistance between the metal electrode and a single walled nanotube.

This is a non-destructive technique and crucial parameters like the force between the tip-tube and the voltage applied on the tip can be studied with precise control. Based on the technique discussed one can envision the potential of this technique in developing transparent contacts between metal electrodes and nanotubes, thereby paving the way to build high performance nanotube based electronic devices.

V. Acknowledgements

I wish to thank Tarek Lutz and Peter Gleeson for their help in electron beam / UV-lithography. I would also like to thank Niall Kinahan for the metal deposition procedures using the Temescal thermal evaporator.

VI. References

[1] A. Javey *et al.*, Physical Review Letters **92**, 106804 (2004).
[2] A. Javey *et al.*, Nature **424**, 654 (2003).
[3] T. A. Beierlein *et al.*, Synthetic Metals **111-112**, 295 (2000).
[4] A. Javey *et al.*, Nano Letters **4**, 447 (2004).
[5] A. A. Kane *et al.*, Nano Letters **9**, 3586 (2009).
[6] Z. Zhang *et al.*, Nano Letters **8**, 3696 (2008).
[7] L. Ding *et al.*, Nano Letters (2009).
[8] L. Marty *et al.*, Nano Letters **3**, 1115 (2003).
[9] J.-O. Lee *et al.*, Journal of Physics D: Applied Physics **33**, 1953 (2000).
[10] R. Seidel *et al.*, Nano Letters **3**, 965 (2003).
[11] L. Dong *et al.*, Journal of Applied Physics **101**, 024320 (2007).
[12] Y. Woo, G. S. Duesberg, and S. Roth, Nanotechnology **18**, 095203 (2007).
[13] A. Garg, and S. B. Sinnott, Chemical Physics Letters **295**, 273 (1998).
[14] P. N. Nirmalraj *et al.*, Nano Letters **9**, 3890 (2009).
[15] M. Stadermann *et al.*, Physical Review B **69**, 201402 (2004).
[16] K. D. Ausman *et al.*, The Journal of Physical Chemistry B **104**, 8911 (2000).
[17] S. Giordani *et al.*, J Phys Chem B **110**, 15708 (2006).
[18] S. Li *et al.*, Nano Letters **4**, 2003 (2004).
[19] T.-H. Kim *et al.*, Nanotechnology **19**, 485201 (2008).
[20] Z. Yao, C. L. Kane, and C. Dekker, Physical Review Letters **84**, 2941 (2000).
[21] Z. Yao *et al.*, Nature **402**, 273 (1999).
[22] J. Tersoff, Nature **424**, 622 (2003).

The image on the page 48 is adapted from the work of Kane et al [101]

A section of this chapter has been published in The Journal of Microscopy & Analysis. "Unravelling the local electronic properties in complex nanoscale systems" Peter N. Nirmalraj, Jonathan N. Coleman and John J. Boland. April 2010. Vol 24, 3, 2010.

A section of this chapter has been published in ACS Nano "Selective tuning and optimisation of the contacts to metallic and semiconducting single walled carbon nanotubes". Peter N. Nirmalraj and John J. Boland. ACS Nano. 2010, *4* (7), 3801–3806.

Chapter 5

Local Electronic Behaviour of Single Walled Carbon Nanotube Networks

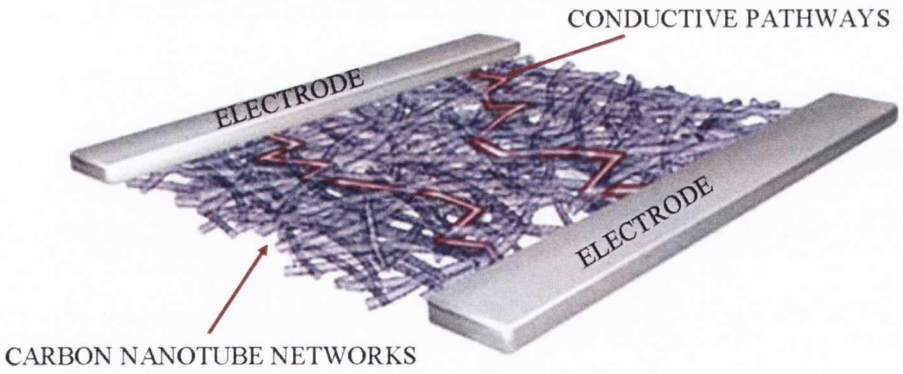

I. Introduction

The electronic behaviour of random networks of carbon nanotubes has been extensively studied for potential applications as transparent and flexible electrode materials [135, 136, 145]. In the design of such materials it is important to understand the complex relationship between the network morphology and the overall electronic properties of these systems. The morphology of the network alone has been previously shown to influence the overall conductivity [217] and other important factors determing the performance of these nanotube networks (NTNs) are length, chirality, diameter of an individual tube and the density of the networks based on these nanotubes. Previous studies by Simien et al. [155] and Hecht et al. [156] have systematically analysed the influence of the length of the tubes on the overall conductivity of the NTNs thereby highlighting the importance of retaining the length during nanotube processing so as to maximise the conductivity of the networks. In chapter 6 of this thesis we demonstrate that the diameter of the network tubes and bundles is a critical parameter in determining the resistance at junctions in the network [40], further demonstrating the correlation between the network morphology and overall conductivity. Although several studies [150, 156, 217, 218] have attempted to link experimental results with theoretical calculations in order to understand the transport in NTNs, we believe that it is essential to record the local electrical connectivity in these random percolating networks in determining the performance of these networks.

In this study we monitor the local electronic behaviour of the NTNs as a function of network density using conductance imaging atomic force microscope (CI-AFM). This probe microscopy technique is an indispensable tool as it has the added advantage of simultaneously acquiring the morphology and current map of these materials. The formation of percolative and conductive pathways has been identified with nanometer scale resolution and the influence of the intrinsic resistance of the tube and the inter tube resistance on the network conductivity has been analysed as the network evolves from a very sparse to a thick network.

II. Experimental Section

We adopted the spray coating technique [203] to tailor the thickness of N-methyl-pyrollidone (NMP) based carbon nanotube (purchased from Iljin Tech) dispersions (concentration = 0.025mg/ml) sprayed onto silicon dioxide substrate (channel dimensions, width = 5 mm and length = 3 mm) with 300 nm oxide thickness. We used dispersion volumes ranging from 1 ml to 10 ml to realize the desired density. Following this deposition the samples were subjected to 5 hours annealing at 500 degrees Celsius under nitrogen atmosphere to get rid of the NMP solvent. As prepared samples were then patterned by UV-lithography and Pd (20 nm) contacts were then thermally evaporated onto the substrates and the desired samples of NTN's contacted by Pd electrodes were obtained after a warm lift off of the polymer in acetone. These samples were then subjected to a further anneal at 400 degree Celsius for 2 hours under Argon/Hydrogen atmosphere to remove the residual resist as previously shown by Ishigami et al. [219]. The samples were then analysed using CI-AFM methodology as described in detail in our previous work [40].

III. Results and Discussion

Classification of Networks

NTNs in general cannot be classified as a thin film because they are not completely continuous over the entire substrate with porous regions [217] occurring at random locations throughout the network. At the same time it is difficult to accurately quantify the thickness in terms of nanometres for sparse networks using probe microscopy or electron microscopy. To establish a relationship between the morphology of the networks with the volume of the dispersion sprayed we can manually calculate the density (number of carbon nanotubes / area) of these networks and categorize them as sparse, thin and thick networks. This form of analysis has its basis in percolation theory [220, 221], where the formation of conductive pathways is analysed for elements of varying geometries.

A suitable representation for a carbon nanotube based system is the adoption of a random array long conducting stick model based on a percolative model. This model has been previously applied by Hu et al. [150] for calculating the density of NTNs. The NTNs analysed in this study are composed of nanotube bundles of varying diameters and individual tubes, since it is not possible (at least at present) to construct networks with just individual tubes. Based on the percolative model each small nanotube bundle and individual tube is considered to be a conducting stick (CS). After each spray coating process we analyse the topography from the AFM images and calculate the average density (number of CS per unit area) from the volume of dispersion sprayed. Note that the concentration of the dispersion used remains constant throughout this calibration process, as changing the CNT dispersion concentration would effectively change the density of the network. In addition, the diameter distribution also shifts to a lower regime as the concentration of the dispersion decreases as shown from earlier work by Giordani et al. [90].

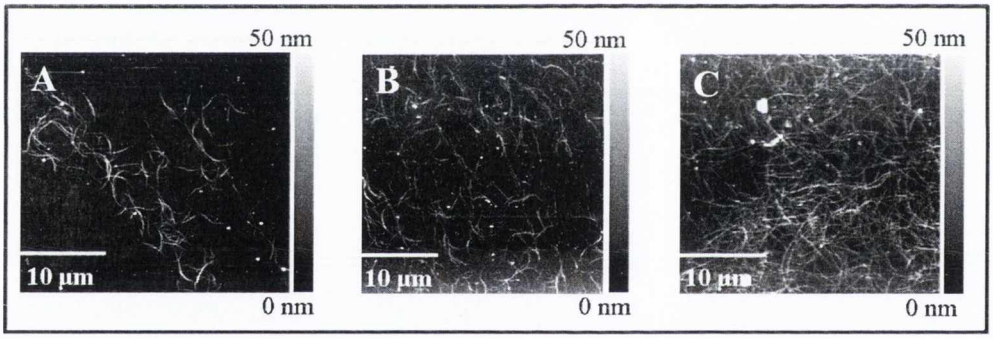

Figure 5.1: AFM topographical images of nanotube networks at varying network densities. (A) Very sparse networks as a result of spraying 2 mL of the CNT dispersion on a SiO_2 substrate; these networks do not have enough conducting pathways. (B) 5 mL of CNT dispersion after being sprayed on a SiO_2 substrate, these networks are considered to be thin networks with enough conducting pathways. (C) Nanotube network as a result of spraying 10 mL of CNT dispersion. These films are taken to be thick films with several layers of nanotubes.

We calculated the average network density after spraying 10 mL of the CNT dispersion to be 5.5 CS/μm^2. And subsequently after spraying 5 mL & 2 mL the network densities are 2.5 and 1 CS/μm^2. As shown in Fig. 5.1 we classify sparse (Fig. 5.1A), thin (Fig. 5.1B), thick networks (Fig. 5.1C) to be obtained after spraying 2 mL, 5 mL and 10 mL of CNT dispersions respectively. The NTN thickness is proportional to the volume of the CNT dispersion sprayed. The mean diameter (Fig. 5.2B) and length (Fig 5.2C) of the tubes (concentration of ~0.025 mg/mL) that form the sparse networks in this study have been calculated to be (1.6 ± 0.2) nm and (1.8 ± 0.3) μm respectively. Diameter and length values are better calculated when the networks are still in two dimensional space and as the network approaches a third dimensionality the tubes are highly intertwined and closely spaced that accurate measurements are not possible.

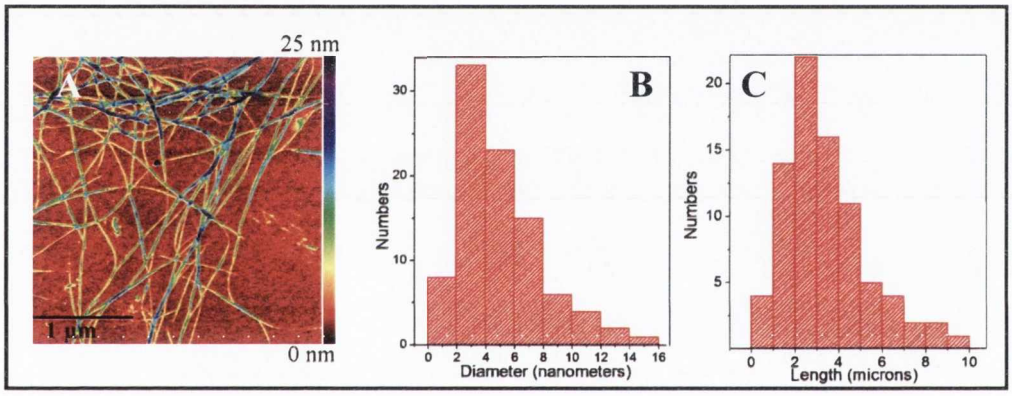

Figure 5.2: Statistical analysis of the diameter and length of SWCNT's. (A) A typical AFM topographical image of a SWCNT network showing the variations in length and diameter of the tubes present within a network. (B) and (C) Diameter and length distribution of several tubes analysed within a network. The mean diameter and length of the tubes is (1.6 ± 0.2) nm and (1.8 ± 0.3) μm, respectively.

Density Dependent Analysis of Networks

Carbon nanotube networks were fabricated with varying densities in order to systematically analyse the formation of percolative pathways. Figure 5.3A, 5.3B, 5.3C depicts the current maps of sparse, thin and thick NTN regions respectively.

Analysing the current maps of the sparse, thin and thick networks shows the formation of conductive pathways and reveals how the local variations in the resistance begin to fade away as the density of the networks increases. In order to obtain the overall resistance of these networks, the electrodes were connected to external leads and the resistance (R) was measured. As the width (W) and length (L) of the NTN channel we calculated the sheet resistance (R_S) for these 2D systems based on equation 1,

$$R_S = R\,(W/L) \qquad \text{Equation 1}$$

For the thick and thin networks the sheet resistance was 2.5 kΩ/square and 20 kΩ/square respectively. No source-drain current measurement was possible for sparse networks even at high bias voltages due to the absence of a connecting pathway between electrodes.

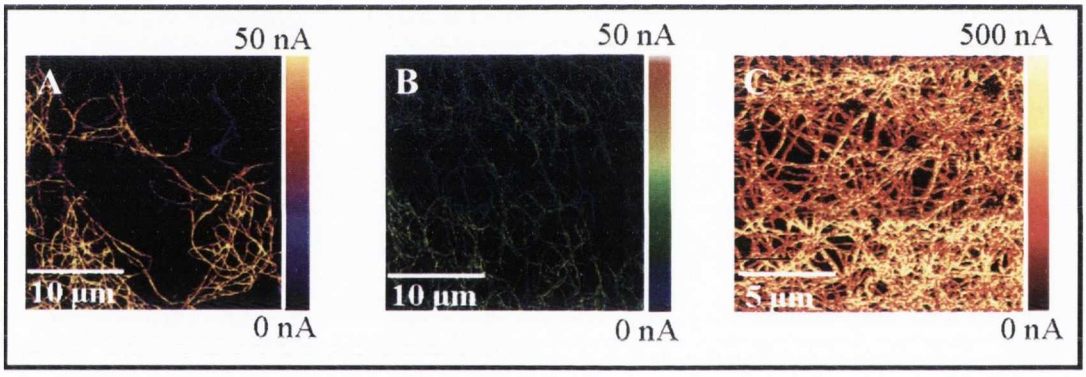

Figure 5.3: CI-AFM analysis on nanotube networks as a function of network density. (A) Current map of a sparse network showing the few available conductive pathways and the variations in the local resistance. (B) Current map of a thin network with plenty of conduction pathways and the resistance is observed to be uniform in most regions of the sample. (C) Current map of thick network portraying a high degree of homogeneity in the local resistance measured within the network. (Scanning conditions. V_{bias}: 5 mV in all the cases; the electrode was at the left hand side for (A) and at the bottom of the images for (B), (C)).

This indicates that even though there are conductive regions within the network there aren't enough conductive pathways to bridge the source and drain electrodes. These sparse networks were formed by spraying 2 mL of the CNT dispersion. In order to increase the number of conductive pathways we increased the volume of sprayed material in steps of 0.5 mL from 2.5 mL and the electrical connectivity was checked until the channel became conductive. It was only after reaching 3.5 mL of CNT dispersion that a sheet resistance of 34 kΩ/square was measured. Furthermore simultaneous CI-AFM measurements were performed on this sample as shown in the topographic and current maps from Fig. 5.4A and 5.4B respectively.

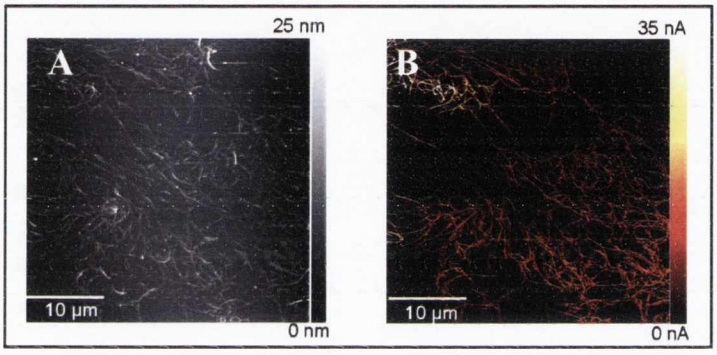

Figure 5.4: Local electronic behaviour of sparse well interconnected networks. (A) Topography of well interconnected nanotube networks. (B) Corresponding current map. (Scanning conditions. V_{bias}: 5 mV, the electrode is at the left hand side of the image).

Analysing the topography of these sparse but well connected networks (Fig. 5.4A) shows that the tubes don't aggregate at certain points of the network but percolate well and spread out as a continuous network over the underlying substrate. This is primarily due to the spray coating technique which doesn't allow the aggregation of the tubes over the surface unlike vacuum filtration technique where the tubes re-aggregate on the filter paper during the filtration process. In addition the current pathways (Fig. 5.4B) revealed the formation of enough conducting pathways between the source and drain electrodes and investigating the local electronic behaviour of this sparse but well connected network highlighted the presence of certain resistive spots that coincided with inter tube junctions. By manually counting the number of CS within a given area from the AFM topographs for the sparse but well connected networks yields a density of 1.5 CS/µm^2 at a critical volume of 3.5 mL of CNT dispersion.

Analysing the sheet conductance as a function of the sprayed dispersion volume shows that conduction within the network is initiated only after the formation of certain crucial building blocks of nanotubes and from then on the sheet conductance increases only to be stabilised after reaching a certain thickness as shown in Fig. 5.5.

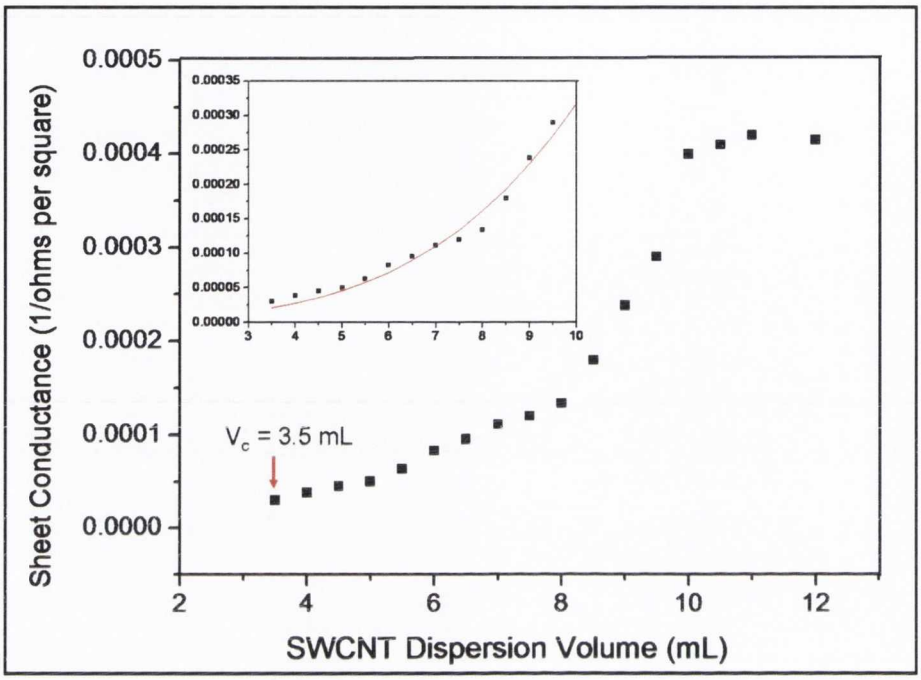

Figure 5.5: Sheet conductance as a function of the volume of SWCNT dispersion sprayed. The network is macroscopically conductive only at reaching the percolation point after a critical volume (V_c = 3.5 mL) of dispersion is sprayed. The sheet conductance increases from onset of the percolative pathways and saturates after stepping into the regime of a thicker network. The inset shows the power fit in the percolation regime, where the critical exponent $\alpha = 1.57$.

According to percolation theory the conductivity of the network is related to the density as shown in equation 2,

$$\sigma = k\,(N - N_c)^{\alpha} \qquad \text{Equation 2}$$

Where σ is the conductivity in three dimensions and as we refer to the sheet conductance in our measurements we use G. K is a constant and N_c is the critical density corresponding to the percolation threshold.

α in equation 2 is an exponent which is predicted to be 1.33 and 1.94 for two-dimensional networks and three dimensional networks respectively [222]. The inset in Fig 5.5 shows a corresponding fit to equation 2 for the data points in the percolation regime. The onset of the macroscopic conduction is initiated upon the formation of percolative pathways within the network. The best fit to our data is results in an α value of 1.57. This value is close to previous work reported by Hu et al. [150] but is still higher than the theoretically predicted value.

At large thicknesses the sheet conductance as shown in the plot in Fig. 5.5. To get a better understanding of such sparse networks, several samples were analysed and similar behaviour was observed in all samples. The interface between highly conductive regions to a comparatively resistive region was analysed and the specific locations limiting the network conductivity were pinpointed as shown in Fig. 5.6.

Figure 5.6A & 5.6B shows the topography and current map of a sparse but well connected nanotube network that is connected to the electrode on the left hand side of the image. As seen from the current map certain regions are found to be more conductive than others. A closer analysis of the area where there seems to be a transition from higher conductivity to lower conductivity as marked in the red box in Fig. 5.6B reveal that area to be a junction between several nanotubes as shown in the current pathway in Fig. 5.6C. Tracing the current pathway along the marked region in Fig. 5.6C reveals the resistance to increase exactly at the junction point where several tubes intersect. This increase in resistance is also shown in Fig. 5.6D where the local resistance is traced as a function of distance. Clearly this data shows that the inter tube resistance sharply increases at the junction between the tubes occurring in a sparse network. From our previous studies we have clearly showed the effect the junction resistance has on the overall properties of the network [40]. The diameter of the tube and the number of connections associated with each junction determines the resistance drop at these intersection sites.

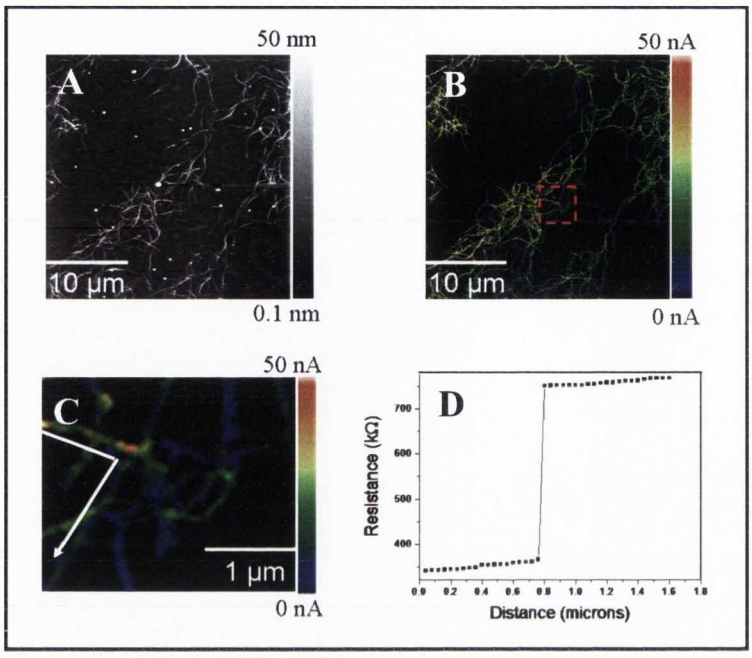

Figure 5.6: CI-AFM analysis on sparse NTNs and junction resistance between nanotubes. (A) & (B) are the simultaneous topography and current map of a sparse NTN. The local resistance of a sparse network depends on the connectivity between tubes and the number of metallic connections leading to the electrode. The red box highlighted in Fig. 5.6B has been zoomed in as Fig. 5.6C showing the exact area where the resistance increases at the junction site. 5.6D is the current trace along the pathway indicated by the white arrow shown in 5.6C (V_{bias}: 10 mV, the electrode was at the left hand side of the image).

Dependence of Local Resistance on the Distance from the Electrode

The local resistance within the network can also be measured as a function of the tip position from the electrode. The resistance is measured at various points in a grid like manner and the resistance at each point is registered. Similar measurements are taken as the tip is marched in small steps from the initial electrode position. Analysing the sparse, thin and thick networks in the same way resulted in a completely different behaviour for each system. In the case of thin networks the local resistance was observed to be lower when measured close to the electrode and then increased gradually only to be stabilized at larger distances as shown in the black trace of Fig. 5.7.

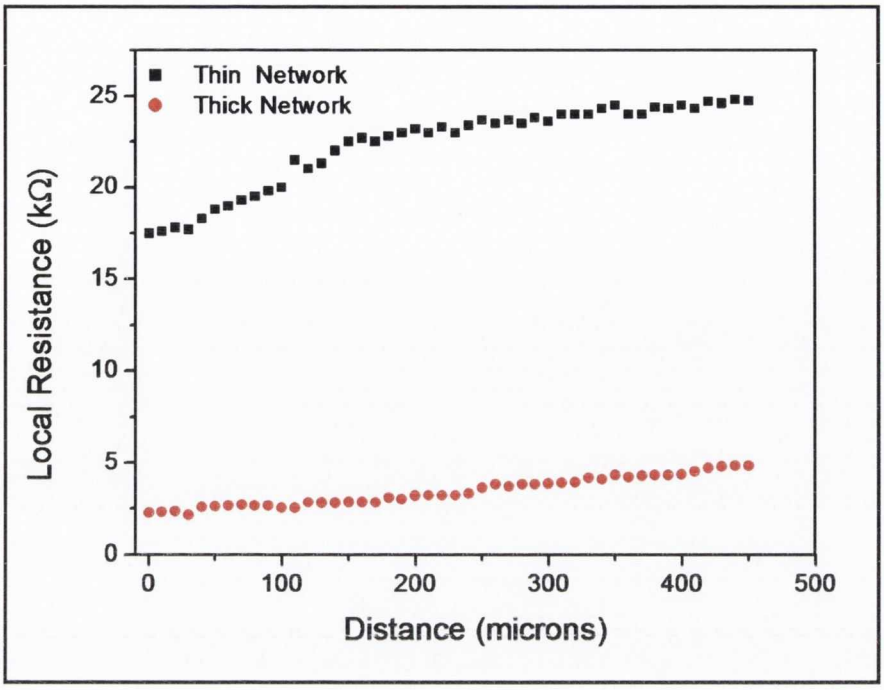

Figure 5.7: Measurement of resistance as a function of distance from the electrode for thin and thick networks. The resistance is observed to increase as we move away from the electrode and then stays constant throughout the network for thin networks and the local resistance increases only very slightly as we march away from the electrode in the case of thicker networks.

In the case of the thicker networks the resistance within the network showed only a very small increase in the resistance and essentially constant throughout the various regions of the sample as shown in the red trace in Fig. 5.7. In contrast to the thin and thick networks, the sparse networks showed no straightforward dependency on the network regions as a function of distance from the electrode. Highly conductive regions were observed nearly 100 microns away from the electrode and very resistive regions were observed in close proximity to the electrode. This behaviour owes its origin to the pronounced presence of mixed metallic and semiconducting connections to the electrode whose effects are subdued as the network thickness increases as seen in the thick networks. The manner in which a specific region in a sparse network is connected to the electrode determines its local resistance, an all metallic pathway results in a highly conductive region and pathway dominated by semiconducting tubes results in a resistive chain of connections.

The scenario is even more complicated when a mixture of metallic and semiconducting tube persists resulting in Schottky barriers [150, 223].

IV. Conclusion

The electronic behaviour of random carbon nanotube networks have been analysed with a high resolution local conductance probe imaging technique. The thickness of these 2D networks is found to be proportional to the volume of the dispersion sprayed.

In the case of a sparse network the proportion of metallic tubes is reduced and conduction is equally shared by the semiconducting species of tubes as well. The prevailing presence of metallic-semiconducting inter tube junctions has been shown to act as Schottky barriers [39] , is one of the focal grounds for the poor conduction in sparse networks. Previous studies by Bekyarova et al [148] and Snow et al [153] on random NTNs have highlighted the co-existence of metallic and semiconducting nanotubes in these networks as its primary limitation. Furthermore the variation in our measured α value of 1.57 in comparison to the theoretically predicted value of 1.33 could also be due to the presence of the semiconducting and metallic tubes within the network as theory does not take this effect into account. As the network thickness is increased from a sparse to a thick network there is a larger population of metallic pathways within these thicker networks and the tubes are well connected thereby facilitating homogeneous conduction throughout the network.

The local resistance within a network is found to be uniform in the case of a thick network and is found to be dependent on the distance from the electrode for a thinner network. Whereas in the case of sparse networks there is no dependency between the local resistance and the distance from the electrode as the local resistance is determined by the electronic pathway through which each region is connected to the electrode. This nanoscale investigation clearly elucidates the conductivity of thicker networks to be controlled by the intrinsic resistance and morphology of the intertwined tubes whereas as the network density is reduced the inter tube junction resistance gains prominence and is shown to dominate the overall network performance.

The behaviour of these NTNs can be analysed based on circuit theory where the thicker, thinner and well connected sparse networks are analogous to a circuit with resistors connected in parallel and very sparse networks correspond to a circuit with resistors in series. The multiple parallel resistors tend to reduce the overall resistance of the networks as seen in the thicker, thinner and well connected sparse networks in contrast to the very sparse networks where there is only one nanotube connected to the electrode that links an entire colony of tubes.

Finally by performing complementary bulk electrical measurements we have analysed the sheet resistance of these NTNs as a function of the dispersion volume and this analysis aids us in highlighting the percolation threshold for conductivity. Furthermore the critical density of the networks at a critical volume of 3.5 mL was calculated to be 1.5 CS/μm^2 based on the macroscopic measurement and AFM topographic data.

CI-AFM analysis on these samples provides well resolved current maps revealing the transistion from sparse and macroscopically non conducting networks into a sparse well connected percolative network. These local conductance measurements provide rich information and insights on the formation of percolative pathways that tend to dominate the overall electronic behaviour of NTNs. The CI-AFM measurement technique can be further expanded to analyse the percolation behaviour in random networks involving metal nanowires and charge transport in self assembled bimolecular films.

V. Acknowledgements

The figure on page 65 is adapted from an article by Gruner. G [149]

VI. References

[1] C. M. Aguirre *et al.*, Applied Physics Letters **88** (2006).
[2] E. Artukovic *et al.*, Nano Letters **5**, 757 (2005).
[3] G. Gruner, Journal of Materials Chemistry **16**, 3533 (2006).
[4] P. E. Lyons *et al.*, Journal of Applied Physics **104** (2008).
[5] D. Simien *et al.*, Acs Nano **2**, 1879 (2008).
[6] D. Hecht, L. B. Hu, and G. Gruner, Applied Physics Letters **89** (2006).
[7] P. N. Nirmalraj *et al.*, Nano Letters **9**, 3890 (2009).
[8] L. Hu, D. S. Hecht, and G. Gruner, Nano Letters **4**, 2513 (2004).
[9] M. A. Topinka *et al.*, Nano Letters **9**, 1866 (2009).
[10] H. J. Jeong *et al.*, Carbon **44**, 2689 (2006).

[11] M. Ishigami *et al.*, Nano Lett **7**, 1643 (2007).
[12] G. E. Pike, and C. H. Seager, Physical Review B **10**, 1421 (1974).
[13] Y. B. Yi, and A. M. Sastry, Physical Review E **66**, 066130 (2002).
[14] S. Giordani *et al.*, Journal of Physical Chemistry B **110**, 15708 (2006).
[15] G. Stauffer, *Introduction to percolation theory* (Taylor & Franics: London, 1985).
[16] S. Heinze *et al.*, Physical Review Letters **89**, 106801 (2002).
[17] M. Stadermann *et al.*, Physical Review B **69**, 201402 (2004).
[18] E. Bekyarova *et al.*, Journal of the American Chemical Society **127**, 5990 (2005).
[19] E. S. Snow *et al.*, Applied Physics Letters **82**, 2145 (2003).
[20] G. Gruner, Scientific American **296**, 76 (2007).

A section of this chapter has been published in The Journal of Microscopy & Analysis. "Unravelling the local electronic properties in complex nanoscale systems". April 2010. Vol 24, 3, 2010

Chapter 6

Nanoscale Probing of Single Walled Carbon Nanotube Junctions

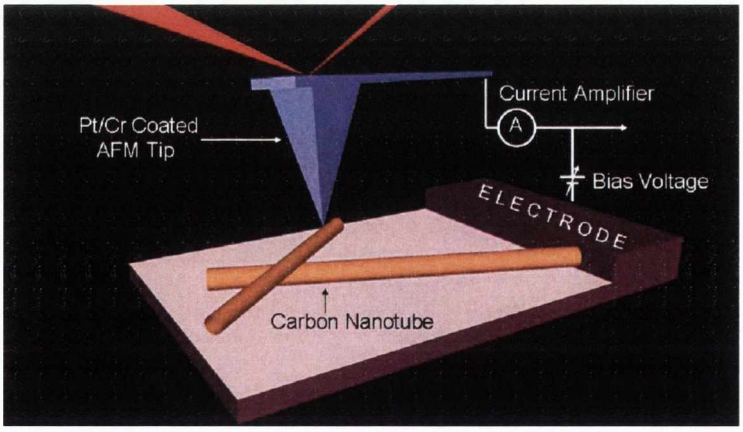

I. Introduction

One of the primary strengths of nanoelectronics is the ability to connect nanoscale materials with a high degree of precision and control, thereby paving the way for producing new building blocks for future electronic devices. This bottom up assembly of nanoscale materials into functional devices has attracted immense attention from diverse quarters of science and technology. Single walled carbon nanotubes (SWCNTs) have been viewed as ideal candidates for nanoelectronics. Depending on their diameter and chirality, SWCNTs are either one dimensional metals or semiconductors [177, 178]. Individual nanotube devices have been constructed and shown to operate in a range of device formats such as single electron tunneling transistors [224] , field effect transistors [133, 225] and even as rectifiers [124]. The fabrication of a multi terminal electronic device based on SWCNTs has been widely anticipated [102, 130] but practical realisation of such devices requires a deeper understanding of the local electronic interactions between the nanotubes. The naturally occurring junctions between nanotubes have been examined closely by Fuhrer et al. [104] and junctions occurring between metallic-semiconducting nanotubes have been shown to be more resistive than metal-metal or semiconducting-semiconducting nanotube junctions.

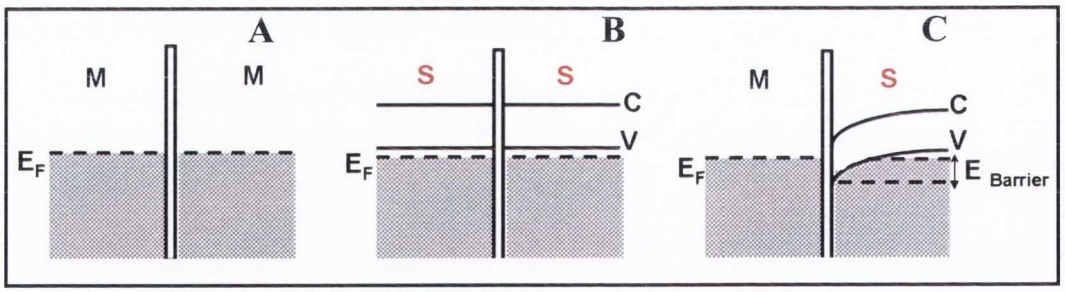

Figure 6.1: Schematic representation of the electronic levels between SWCNT's. Metal-metal junction (A), semiconductor-semiconductor junction (B), metal-semiconductor junction (C). The formation of Schottky barrier with height $E_{Barrier}$ is shown in the metal-semiconductor. (C, V is the conduction and valence bands of the semiconducting tube and E_F denotes the Fermi level).

Studies [104, 124, 127-129, 132, 134] on the electronic properties of the nanotubes forming the junctions have been performed from an experimental and theoretical perspective and the junctions between metallic-semiconducting tubes have been described in terms of Schottky barriers.

Schottky barriers are formed due to the charge transfer driven by the relative alignment of the Fermi level (E_F) of the metallic tube with the band gap of the semiconducting tube at the junction and results in the depleting of carriers from the semiconducting nanotube at this interface. Carrier depletion in the semiconducting nanotube associated with the Schottky barrier formation represents a barrier to charge transport across the interface. A schematic representation of the electronic structure at the junctions between a metal-metal (A), semiconducting-semiconducting (B) and a metal-semiconducting (C) junction are shown in Fig. 6.1. Schottky barriers have been shown to restrict the overall performance of nanotube based devices as reported by bulk electrical measurements [223, 226] and local probe microscopy techniques [39]. The electronic properties at the junction is partly influenced by the underlying substrate where the electronic transport between the nanotubes and the substrate is enhanced when the atomic structures of the two systems in contact are commensurate as shown by the π-orbital tight binding Hamiltonian calculations of Buldum et al. [227]. The issue of adhesion between the SWCNT and the underlying surface is also an important criterion that determines the local charge transport at the junction sites [228].

Apart from naturally occurring junctions it has also been proved possible to construct and manipulate junctions of varying geometries. Terrones et al. [229] have shown the formation of X, Y, and T junctions by controlled electron irradiation. This procedure also results in welding of the nanotubes at the point where they cross to yield stable junction geometries. Probe microscopy has also been used to precisely define local junction geometries by mechanical manipulation and the electrical transport across these junctions have been studied by bulk electrical methods [230] . Despite the enormous amount of effort that has been focused on fabricating and studying the properties of artificially tailored junctions, this approach is time consuming process and is not suited for large scale synthesis of SWCNTs. Random 2D networks of SWCNTs on the other hand are comparatively easy to mass produce and do not require controlled placement.

In random networks we cannot control the local the local geometry of the junctions or the metallic to semiconducting ratio of nanotubes. In certain cases where only a semiconducting network is required a gating voltage can be applied to remove the contribution of metallic tubes from the conducting network.

Although the role of chirality on the junction resistance has been studied, an in-depth study of the effect of bundle diameter on the junction resistance is lacking. To address this problem we have conducted a local probe microscopy investigation on the effect of the carbon nanotube diameter on junction resistance. We have performed a case specific analysis of junction resistance versus a range of diameter distributions and a statistical binning of this data reveals that the junction resistance to increase as the diameter of the bundles forming the junction increases.

II. Results & Discussion

Local Morphology of SWCNT Junctions

Analysing the structure of the junctions within the NTN reveals the presence of various junction geometries depending on the manner in which they are deposited and the number of bundles/tubes available for interaction in close proximity which is dictated by the concentration of the solution, the substrate interactions and the tube/bundle length.

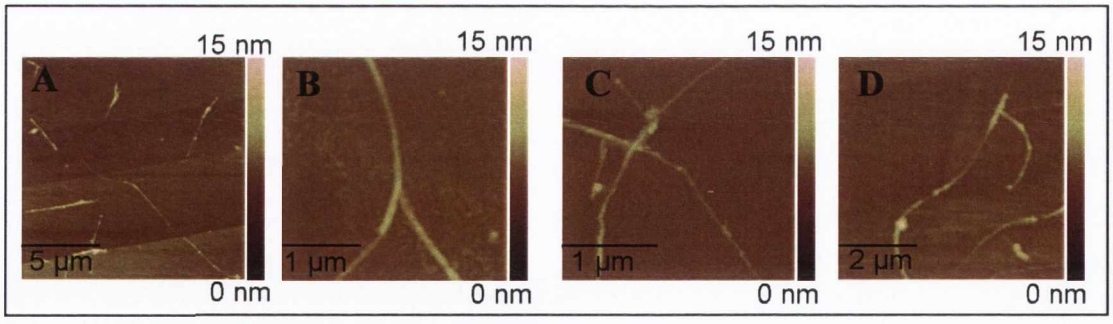

Figure 6.2: AFM analysis of the local morphology of different junction geometries existing within a nanotube network. (A) Head-tail arrangement of a junction between two individual tubes. (B) Topography of Y shaped geometry between two nanotubes. (C) X shaped junction formation between nanotubes crossing over only at one point. (D) Spliced junction between several nanotubes occurring at specific points as seen from the increase in localised height changes.

Various SWCNT junction configurations on SiO_2 surface observed with the AFM in tapping mode is shown in Fig.6.2. Figure 6.2A shows topography of a junction formed between two individual nanotubes of diameter (D) ~1.65 nm, this is a head-tail arrangement where the tubes are connected only at their ends.

The most commonly occurring junctions are the Y shaped junctions (Fig. 6.2B) with spliced junctions (Fig. 6.2D). These spliced junctions can be identified only by the local height difference as one tube merges well with another tube along the side walls. This type of configuration is common in percolating networks of nanotubes. The X shaped junctions (Fig. 6.2C) presents an interesting structure in which tubes and bundles cross over at just one point and the junction resistance is expected to differ depending on whether the underlying or overlying tube is connected to the electrode. After having identified the possible junction configurations occurring within a NTN we analysed nearly 200 junction structures and binned the data to identify whether there was a preference for any particular junction configuration. Figure 6.3 presents the data plotted as a pie diagram which clearly indicates that the most commonly occurring junction structures are the Y shaped junctions followed by the spliced junctions and X shaped junctions. The presence of the head-tail arrangement was the least occurring junction type.

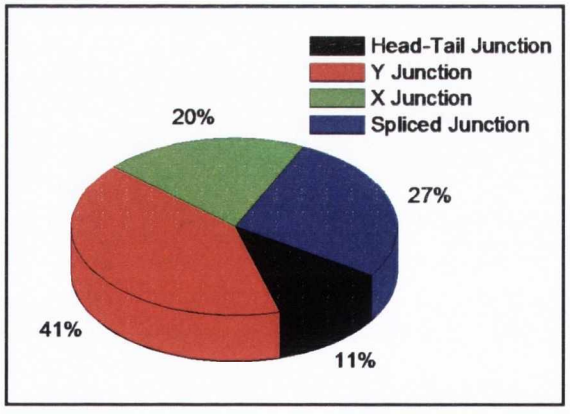

Figure 6.3: Statistical analysis of the occurrence of varying junction geometries within a NTN. On a hierarchical order the Y junction seems to dominate the other available junction geometries. The head-tail arrangement on the other hand seems to be the least energetically favourable configuration from the statistical analysis.

It is important to record such an analysis of the different junction geometries since when we measure the junction resistance we can determine whether there is a particular geometry with a minimum junction resistance.

In order to study the effects of the diameter of the bundles on the junction resistance we have classified the data into 4 different categories; 1) Junction between two individual nanotubes, 2) Junction between an individual nanotube and a smaller diameter bundles, 3) Junction between 2 smaller diameter bundles and 4) Junction between two larger diameter bundles. By analysing and binning the data in these formats we clearly cover all possible configurations within a nanotube network, thereby giving us a true picture of the electronic behaviour of the sparse networks and the expected junction resistance that such network has to offer.

Diameter Dependent Analysis of Junction Resistance

The basic junction that forms within a NTN is the intersection between two individual tubes of any possible configuration. Figure 6.4 shows a similar case where a Y junction is formed between two individual nanotubes. The topography (Fig. 6.4A) shows tube 1 (D: ~ 1.4 nm) that is connected to the electrode (not shown in the image) to be connected by tube 2 (D: ~1.75 nm) at a common junction point.

The simultaneously acquired current map is shown in Fig. 6.4B, where the current pathways along tube 1 and from tube 1 through the junction and over tube 2 are traced. Plotting the local resistance as a function of distance we trace over the two different pathways as shown in Fig. 6.4C. We find the resistance at the junction to increase by ~70 kΩ between the two tubes. Beyond the junction the resistance is observed to increase gradually as we trace along both the different pathways; pathway 1 (along tube 1) and pathway 2 (along tube 2). Note the width of the current trace is not reflective of the actual diameter of the tube as shown in Fig. 6.4B. The data acquired from the diameter of the tubes from high resolution topography maps to the resistance traces obtained from the current maps allows us to correlated the effect the diameter of the tubes have on the local junction resistance.

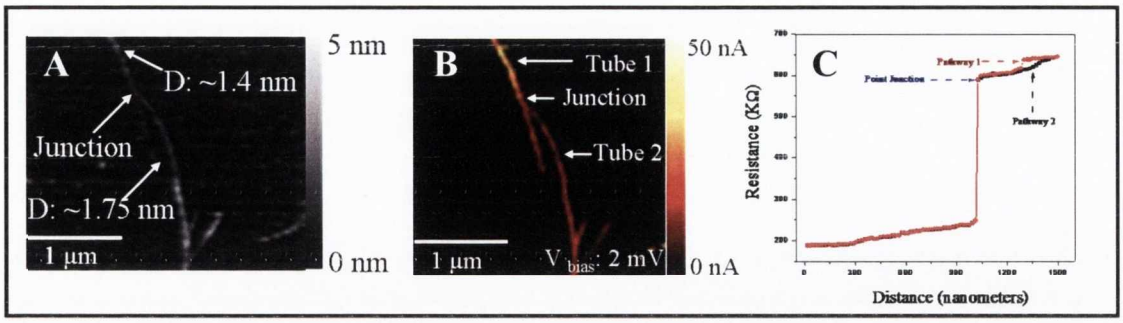

Figure 6.4: Junction resistance analysis between two individual nanotubes. (A) & (B) Topography and current map of the nanotubes intersecting to form a junction. (C) Tracing the resistance along pathway 1 (along tube 1) and pathway 2 (along tube 2). The resistance due to the junction formation is ~ 70 kΩ and the resistance continues to increase along the two different pathways from the junction point onwards. (Scanning conditions: V_{bias}: 2 mV, Preamplifier sensitivity: 100 nA/V)

To further elaborate these effects similar measurements were performed after locating a junction between a smaller diameter nanotube bundle and an individual nanotube. Figure 6.5 shows a junction formed between tube 1 (D: ~2.3 nm) and tube 2 (D: ~1.65 nm).

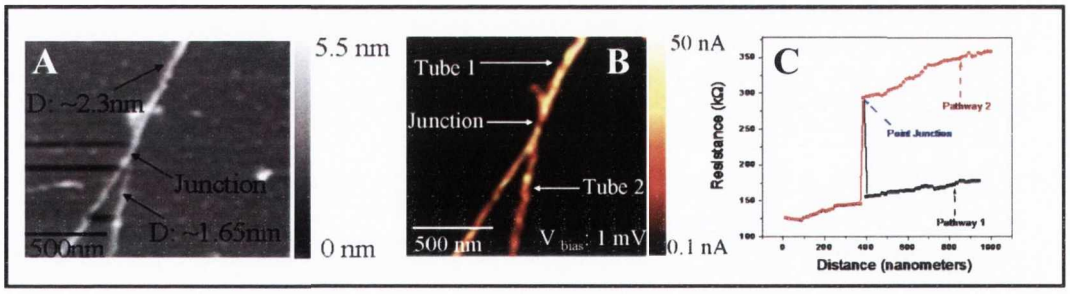

Figure 6.5: CI-AFM results on nanotube junction between a smaller diameter bundle and an individual tube. (A) & (B) Topography and current map of tube 1 (D: ~2.3nm) which is intersected by tube 2 (D: ~1.65nm). The electrode is positioned on the top of the image (not shown). (C) Local resistance analysis through the bundle and individual tube depicted as pathway 1 and 2. (Scanning conditions: V_{bias}: 1 mV, Preamplifier sensitivity: 100 nA/V)

Figure 6.5A shows the topography detailing the tube size and junction geometry while Fig. 6.5B shows the simultaneously acquired current map of the tubes.

The current map was converted into a resistance measurement along the two traces shown (Fig. 6.5C). Pathway 1 is traced from the electrode along tube 1 (D: ~2.3 nm tube bundle), until it encounters tube 2 (D: ~1.65 nm single tube), which is lying on top of the tube 1, and then continues along the length of tube 1. The resistance increases monotonically along the bundle until the junction with the single tube at which point the junction resistance is measured to be ~ 180 kΩ at the junction and after which the resistance recovers to the original level. From data like these we can get two types of information; analysis of the rate of increase of resistance with position along the bundle gives us the effective bundle conductivity, while the magnitude of the jump at the junction tells us about the junction resistance. Treating the bundle as a resistive cylinder connected via the rest of the network to the electrode we can write the bundle resistance, R, as

$$R = R_{other} + \frac{l}{\sigma A} \qquad \text{Equation 1}$$

Here R_{other} is the combined resistance of the network and contacts, l is the position along the bundle, while σ and A are the bundle conductivity and cross-sectional area respectively. By measuring dR/dl we calculate the conductivity of the ~2.3 nm bundle to be ~3×10^{6} S/m (Resistivity (ρ) = 3.34×10^{-7} Ωm). This is in good agreement with measurements on individual ropes of SWNTs which gives conductivity close to 10^{6} S/m [231]. Note however, that the measured conductivity of the bundle is a lower bound since not all the tubes within the bundle cross-section may contribute to the measured current. The observed jump in resistance of ~180 kΩ corresponds to the resistance of the junction between the bundle and the single tube. Along pathway 1 we see a spike in the resistance as the AFM tip momentarily passes over the single tube. For pathway 2, the resistance increases abruptly and then remains constant. This is due to the tip initially following tube 1 before moving to and subsequently following tube 2. In each case, the resistance change is equal to the junction resistance between a ~2.3 nm bundle and a ~1.65 nm single tube.

Similar measurements on junctions occurring between two smaller diameter bundles have been analyzed as shown in Fig. 6.6. Tube 1 (D: ~4.2 nm) as seen from the topographic image (Fig. 6.6A) intersected by tube 2 (D: ~2.6 nm).

It is tube 1 that is connected to the electrode (not seen in the image) and the current map (Fig. 6.6B) shows the possibility of two different pathways along tube 1 and along tube 1 passing over the junction and tracing along tube 2 as shown in the blue arrow. Tracing the resistance along the two different pathways shows the resistance to increase at the junction as we trace along tube 1 as tube 2 is lying under tube 1. The resistance also increases gradually as we trace along tube 1 which is expected as the resistance increases with the length. Tracing the resistance along pathway 2 shows a significant increase in the resistance by ~ 380 kΩ as we shift from tube 1 into tube 2. A similar increase in junction resistance is not observed when measuring along tube 1 since it lies on top of tube 2 at the intersection of the tubes.

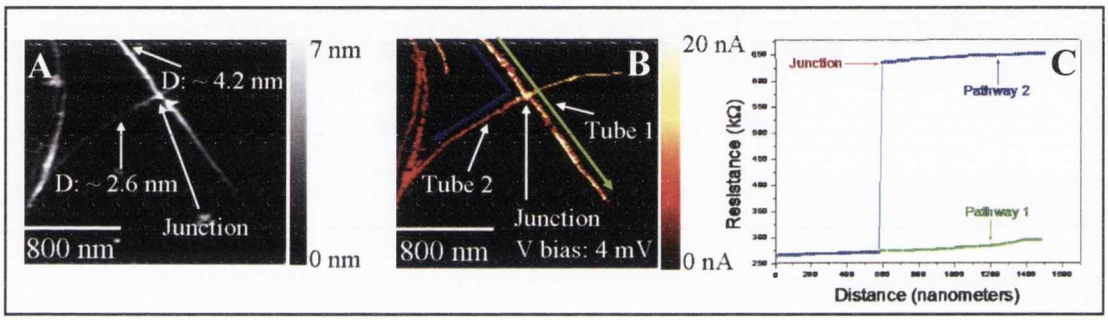

Figure 6.6: Local junction resistance analysis between smaller diameter bundles. (A) Topography image showing the intersection of tube 1 with tube 2, where tube 2 is lying underneath tube 1. (B) Current map showing the possible current pathways across the junction and tracing the resistance along the pathways indicated in the current map, the resistance at the junction along pathway 2 increases by ~ 380 kΩ. (Scanning conditions: V_{bias}: 4 mV, Preamplifier sensitivity: 100 nA/V)

This data also shows that junction shown in Fig. 6.6B is formed of predominantly metallic bundles as a semiconducting tube in that region would have depleted the carriers at the interface and a common increase in junction resistance which would have been observed regardless of the pathway traced.

Figure 6.7A shows the topography and that tube 1 and tube 2 have diameters of ~4.8 nm and ~6 nm respectively. Tube 1 is connected to the electrode at one end and to tube 2 at the other. The parallel local resistance trace between two larger diameter tubes as shown in Fig. 6.7B shows an increase in junction resistance of ~ 750 kΩ when the tip is over the junction.

The current map from Fig. 7B shows the current to drop at the junction between the two tubes and gradually decrease. A bias of 2 mV was applied to the electrode on the surface while the tip was held at ground potential. Tracing the local resistance along the tube 1 and moving onto tube 2 shows the resistance to increase sharply at the junction by a much larger degree when compared to junction cases involving individual tubes and smaller diameter bundles.

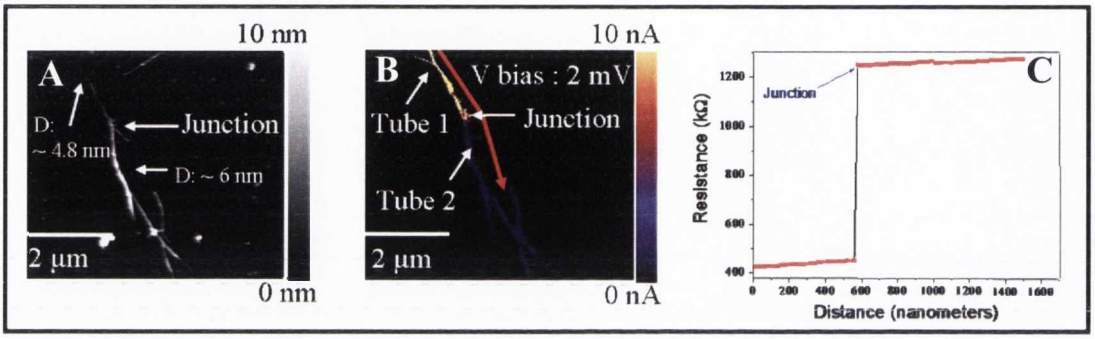

Figure 6.7: Junction resistance analysis between larger diameter bundles. (A) Topography between tube 1 (D: ~4.8 nm) and tube 2 (D: ~ 6 nm). (B) Current map of the junction between tube 1 and tube 2 showing the local electronic effects between the two tubes. Tracing the current pathway along tube 1 through the junction and moving along tube 2 shows a clear increase in the resistance at the junction point as shown in the resistance trace as shown in part C. (Scanning conditions: V_{bias}: 2 mV, Preamplifier sensitivity: 100 nA/V).

The data acquired and discussed so far is specifically focused on junctions occurring between two similar or different diameter bundles/tubes and an analysis of the correlations between local geometry and junction resistance. Although we have systematically analysed single isolated units, the behaviour of these tubes in a network needs more investigation. In a NTN these single unit configurations can occur in different possible combinations and in most cases any small region of tubes exhibits junctions formed by tubes of varying diameters. This is a more complex case study to analyse as the junction resistance is bound to vary as the local topography and the diameter changes. The adhesion between the tubes is also extremely important here as loosely connected tubes tend to exhibit higher contact resistance. Also the contact force between the tip and the tube is maintained at ~0.5 nN in order to establish electrical contact, increasing the loading force damages the tube and also contaminates the tip

leading to a higher measured contact resistance measured. The current pathways across these networks can be classified as either resistor in series or in parallel, depending on how many tubes are connected to the electrode. In the case of multiple connections to the electrode the network behaves as multiple parallel resistors thereby decreasing the overall resistance. When only one tube is connected to the electrode and when it branches out to connect with other tubes can be described as resistors connected in series. Figure 6.8 shows a more complex section of network comprising of two single tubes and two bundles, which intersect to create three different junctions (labelled A-C).

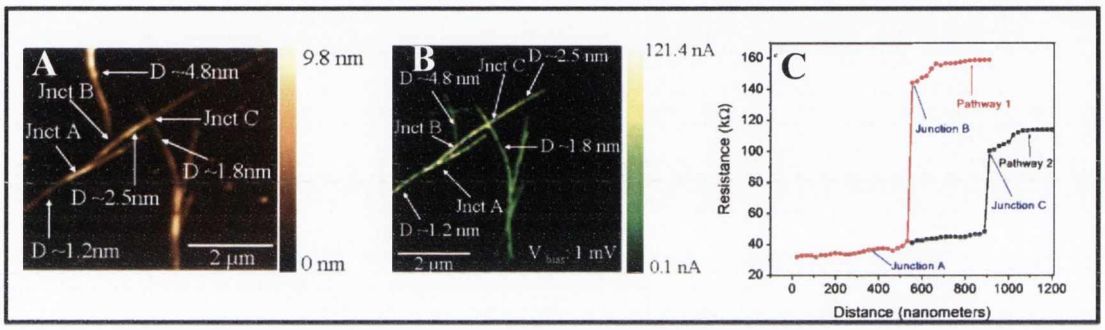

Figure 6.8: Current map of interconnected tubes of varying diameter showing the formation of junctions with varying resistances. (A) & (B) Topography and current map of the nanotubes within a sparse network. (C) Local resistance analysed along the individual tube connected to a sparse configuration of nanotubes highlighted as pathway 1 and 2. The electrode is positioned on the left hand side of the image (not shown). (Scanning conditions: V_{bias}: 1 mV, Preamplifier sensitivity: 100 nA/V).

Two pathways are traced along this network involving junctions A, B and C. Pathway 1 shows a single tube (D: ~1.2 nm) whose resistance slowly increases as the single tube merges into a smaller diameter bundle (D: ~2.5 nm) at junction A. The absence of a marked increase in resistance beyond junction A reflects an intimate contact between the single tube along the length of the bundle, and suggests that both are metallic. The resistance increase along the single tube indicates a conductivity of ~6.7×10^{7} S/m ((Resistivity (ρ) = 1.5×10^{-8} Ωm), significantly higher than that observed for the ~2.3 nm bundle. There is a sharp increase in resistance (~115 kΩ) at junction B between the ~2.5 nm bundle and the larger diameter bundle (D: ~4.8 nm). Along pathway 2, the ~2.5 nm bundle forms junction C with a ~1.8 nm diameter single tube.

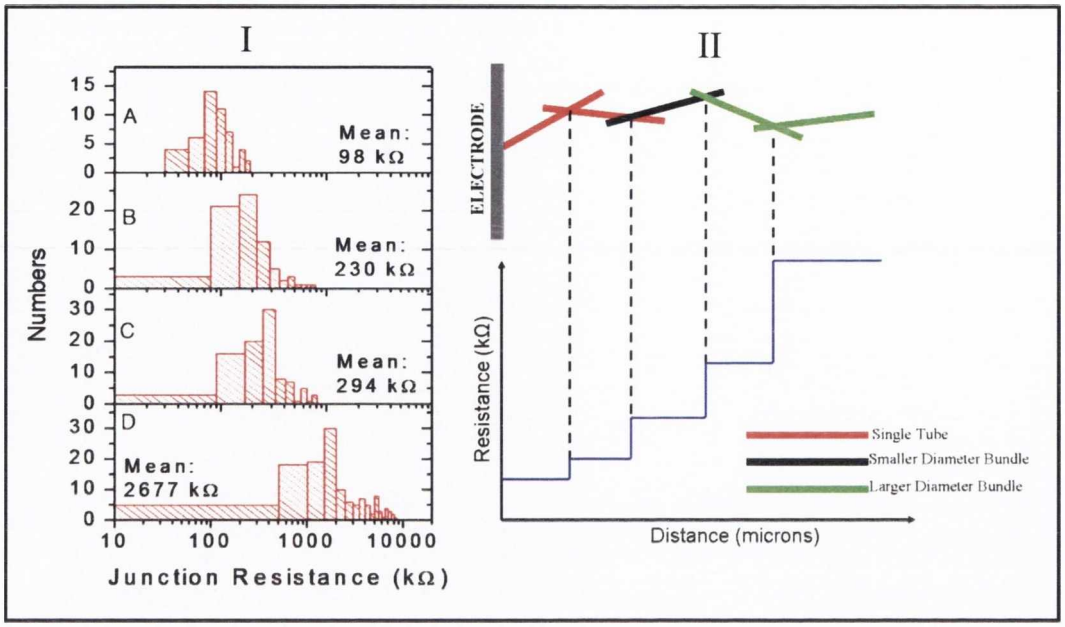

Figure 6.9: Diameter dependent junction resistance analysis. (I) Junction resistance analysis of pristine carbon nanotubes based on the diameter of the participating tubes. Case A, B, C, D are the junction resistance measured between individual tubes (diameter: 1.2 - 1.8nm), between individual nanotubes and smaller diameter nanotube bundles (diameter: 2.5 - 4.5 nm), between medium diameter nanotube bundles (diameter: 4.5 - 6.8 nm) and the junction resistance between larger diameter nanotube bundles (diameter: 7 – 14 nm), respectively. (II) Schematic representation of the different junction resistance values encountered between varying diameter tubes.

The junction resistance is ~70 kΩ, significantly less than the resistance observed between the same ~2.5 nm bundle and the large ~4.8 nm diameter bundle. Evidently, the measured junction resistance is dependent on the diameters of the tubes and bundles comprising the junction. Hundreds of NTN junctions comprised of various diameter were analyzed and segregated into one of the four groups shown in Fig. 6.9. The binning process does not separate metallic and semiconducting elements in these NTNs. The lowest resistance group (labelled A) has a mean value of 98 kΩ and corresponds to junctions comprised of single nanotubes (1.2 – 1.8 nm). Junctions formed between single tubes and small diameter bundles (2.5 – 4.5 nm) (B) have a mean resistance of 230 kΩ, whereas junctions involving exclusively medium (4.5 – 6.8 nm) and larger diameter bundles (7 – 14nm) have resistances of 294 kΩ (C) and 2.7 MΩ (D), respectively.

III. Conclusion

The resistance measured between the various nanoscale junctions comprised of nanotubes of varying diameter reveals a striking dependence between the tube diameter and junction resistance. This is particularly true for junctions involving individual tubes where a mean junction resistance value of ~ 98 kΩ is calculated after measuring several single tube junctions. This value is much lower when compared to previous electrical measurements by Yao et al. [124] where they measure the resistance between two individual tubes to be ~ 608 kΩ.

The lower junction resistance obtained in this work is primarily due to the quality of the materials used and due to the minimal contact resistance between the metal electrode and the nanotube. From our earlier measurements on the contact resistance between a Ti/Au electrode and metallic tubes exhibits a contact resistance of ~ 40 kΩ in comparison to ~ 100 kΩ measured by Yao et al for an individual metallic nanotube contacted by a Ti/Au electrode. This trend in junction resistances has not been previously reported but can be understood in terms of the resistances that exist between individual tubes within a bundle. Thus the sharp increase in resistance is a direct measure of the junction resistance only for the case of junctions between individual SWCNTs.

The junction resistance measured between an individual tube and a smaller diameter bundle is more intricate as a bundle is comprised of several tubes and the nature of coupling between the tubes is equally important. This is a more compelling study as the diameter of the tubes forming the junction increases as in case B, C and D in the section I in Fig 6.9. For bundles the measured jump in resistance is actually comprised of the two resistances in series: the contact resistance between the bundles R_C and the resistor network associated with charge transport across the bundles R_B.

The latter depends on the bundle conduction mechanism and we consider here two limiting cases: (i) transport has contributions from all the tubes in the bundle, and (ii) transport is confined to the tube into which charge injection occurs.

Since CI-AFM is restricted to measurements at the top surfaces of bundles, it measures $R_C + R_D$, where R_D is the resistor network associated with transport across the entire diameter of the bundle. For case (i), since $R_B \leq R_D$ the measured resistance jump is an upper bound on the true junction resistance $R_J = R_C + R_B$. . For case (ii) the value of R_B depends on the precise location of the tubes that carry charge in and out of the junction. At one extreme, we consider the two tubes that make physical contact at the junction, in which case $R_B = 0$ and hence $R_J = R_C$. Alternatively, the tubes could be on the opposite sides of the two bundles that comprise the junction so that $R_B = 2 \times R_D$. Therefore, for case (ii) the junction resistance is bounded by $R_C \leq R_J \leq (R_C + 2 \times R_D)$, and thus the average value is well described by the measured resistance jump of $R_C + R_D$. Apart from the influence of the diameter of the tubes on the inter tube resistance the electronic variations (metallic/semiconducting) that are composed within a bundle also affects the junction resistance.

This analysis shows that CI-AFM provides a good measure of junction resistance and that effective debundling and hence obtaining smaller R_B values is necessary as a lower junction resistance is measured between individual tubes and smaller diameter bundles.

IV. References

[1] T. W. Odom et al., Nature **391**, 62 (1998).
[2] J. W. G. Wilder et al., Nature **391**, 59 (1998).
[3] H. W. C. Postma et al., Science **293**, 76 (2001).
[4] R. Martel et al., Applied Physics Letters **73**, 2447 (1998).
[5] S. J. Tans, A. R. M. Verschueren, and C. Dekker, Nature **393**, 49 (1998).
[6] Z. Yao et al., Nature **402**, 273 (1999).
[7] A. N. Andriotis et al., Phys Rev Lett **87**, 066802 (2001).
[8] M. Menon et al., Physical Review Letters **91**, 145501 (2003).
[9] M. S. Fuhrer et al., Science **288**, 494 (2000).
[10] P. Lambin, and V. Meunier, (Kluwer Academic Publishers, Dordrecht, Netherlands, 2001), pp. 265.
[11] L. W. Liu et al., Physical Review B **71**, 155424 (2005).
[12] J.-M. Ting, and C.-C. Chang, Applied Physics Letters **80**, 324 (2002).
[13] M. S. Wang et al., Advanced Functional Materials **15**, 1825 (2005).
[14] I. Zsoldos et al., Modelling and Simulation in Materials Science and Engineering **12**, 1251 (2004).
[15] P. Avouris, Z. H. Chen, and V. Perebeinos, Nature Nanotechnology **2**, 605 (2007).
[16] S. Heinze et al., Physical Review Letters **89**, 106801 (2002).
[17] M. Stadermann et al., Physical Review B **69**, 201402 (2004).
[18] A. Buldum, and J. P. Lu, Applied Surface Science **219**, 123 (2003).
[19] N. R. Paudel et al., Molecular Simulation **35**, 520 (2009).

[20] M. Terrones et al., Phys Rev Lett **89**, 075505 (2002).
[21] H. W. C. Postma et al., Physical Review B **62**, R10653 (2000).
[22] J. E. Fischer et al., Physical Review B **55**, R4921 (1997).

This chapter has been published in Nano Letters "Electrical connectivity in single walled carbon nanotube networks" Peter N. Nirmalraj et al. 2009, 9, (11), 3890-3895.

Chapter 7

Effect of Acid Treatment & Annealing on the Electronic Properties of Single Walled Carbon Nanotubes

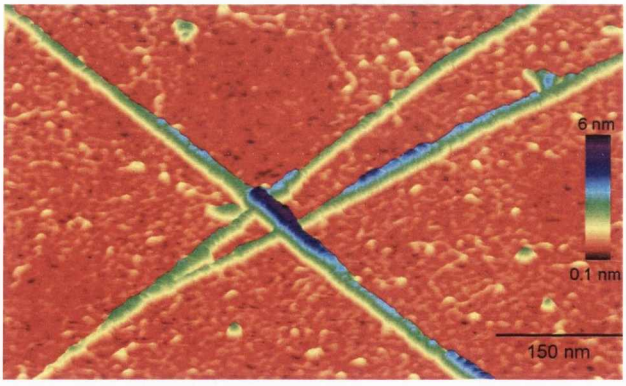

I. Introduction

Various factors like the diameter/length of the tubes and morphology of the networks have been carefully tuned to maximise the conductivity of nanotube networks. In order to improve the film conductivity without having to forgo transmittance it is necessary to develop alternate approaches such as controlled acid treatment. Acid treatment has been known to improve the conductivity in nanotube networks but it also damages the sidewalls of the tubes and creates defects that disturb the chemical inertness of these random networks making them unsuitable for some applications. In particular acid treatment has been shown to induce doping [158, 232] in carbon nanotubes but by careful tailoring of the acid treatment the desired conductivity can be obtained and at the same time the intrinsic structure can be preserved. Geng et al. [143] have shown that it is possible to increase the conductivity of nanotube networks (NTNs) by a factor of 4 times by proper acid treatment without extensive doping effect. Acid treatment is effective in removing the embedded secondary phases such as graphitic particles and amorphous carbon content [233] that accompanies the pristine nanotube material but also gets rid of the metal catalyst particles [234-236] that are present in nanotubes obtained through catalytic seeded growth. For SWCNTs dispersed using surfactants, acid treatment has also shown to remove the residual surfactant and also facilitates densification of the network thereby promoting effective conductance through the 1D nanotubes [143]. Several chemical entities have been experimented with to purify the nanotubes ranging from hydrochloric acid (HCl), nitric acid (HNO_3), thionyl chloride ($SOCl_2$), sulphuric acid (H_2SO_4) to bromine (Br) and their effect on CNT networks have been analysed from a bulk perspective. Only a few studies have carefully examined the effects of these chemicals on the inter tube charge transport for metallic and semiconducting tubes enriched networks [137, 142, 237]. It is of utmost importance to understand the effect of acid treatment on the individual tubes, junctions between the tubes and on the overall conductivity as well. We have performed a controlled and milder acid treatment on CNT networks and analysed the electronic behaviour of the individual nanotube and inter tube junctions in finer detail.

De-doping experiments were also performed via high temperature annealing to remove the adsorbed dopants and the effect of annealing on the junction resistance was examined in detail. Finally we performed bulk electrical measurements on pristine, acid treated and annealed CNT networks and a comparative analysis was performed. The measured junction resistances for pristine, acid-treated and annealed SWCNT bundles was observed to correlate well with the conductivities of the corresponding films, in excellent agreement with a model in which we have shown the junctions to control the overall network performance.

II. Experimental Session

For the acid treatment procedure, Iljin tubes were exposed to nitric acid (70%, 15 M) for 2 hours at room temperature. The as treated tubes were then subjected to vacuum filtration in order to form a bucky paper that was rinsed thoroughly with deionised water. The acid treated bucky paper was again dispersed in NMP to form thermodynamically stable suspensions and these dispersions were then sprayed onto SiO_2 surfaces as discussed in chapter 3. The reason for not treating the already deposited pristine nanotubes on the surface with nitric acid was because the acid treatment resulted in the degradation of the metal contacts and on the oxide thickness on the surface as well. It is critical to have a sufficiently thick oxide layer on the silicon surface to carry out CI-AFM measurements. For 4 probe electrical measurements we immersed pristine carbon nanotube networks as mentioned above (on PET) in 12 M nitric acid for two hours followed by rinsing in deionised water. For the de-doping experiments we annealed the pristine nanotube network at 1000 $^{\circ}$C for 12 hours and maintained the same conditions for both CI-AFM and 4 probe electrical measurements. All the networks for the bulk electrical measurements were synthesised using the vacuum filtration technique. The optical and DC conductivity of the pristine, acid treated and annealed films were measured on both poly ethylene terephthalate (PET) and quartz substrates.

III. Results & Discussion

Effect of Acid Treatment

The topographic image of the acid treated NTNs shows a clean topographical landscape when compared to the pristine NTNs, which is primarily due to the removal of the amorphous carbon content present in the sample. CI-AFM measurements on the sparse acid treated networks reveal important information regarding the junction resistance and the intrinsic resistivity of an individual nanotube. Figure 7.1A shows the topography of a sparse NTN with the electrode positioned on top of the image. Tube 1 (D: ~ 3.6 nm) provides electrical connection to the rest of the network as it is the only tube connected to the electrode. The topographic data shows tube 1 to be intersected by an individual tube of diameter ~ 1.75 nm (Tube 2) to form a junction (Jnct A). The simultaneously acquired current map (Fig. 7.1B) also complements the topographic data and traces the resistance along tube 1 and shows the resistance to slightly increase at the junction of about ~ 25 kΩ (Fig. 7.1C).

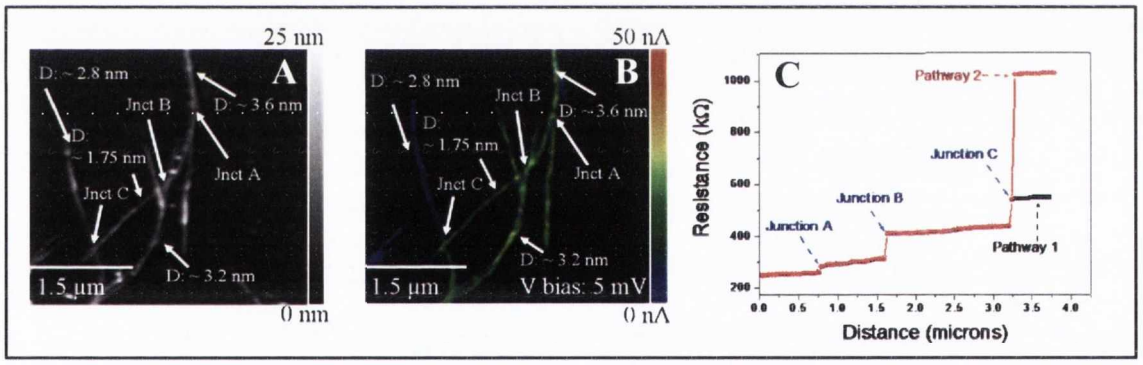

Figure 7.1: Junction resistance analysis of sparse acid treated nanotube networks. (A) & (B) Topography and current map of an acid treated nanotube network where the electrode is positioned on top of the image. Both the topography and current map shows the formation of junctions between the tubes of varying diameters. The associated increase in resistance at the junctions is recorded with nanometer scale resolution and plotted as resistance versus distance from the electrode in section C. The resistance is observed to increase at the junctions but is still very low when compared to the junction resistance between pristine nanotubes. (Scanning conditions: V_{bias}: 5 mV, Preamplifier sensitivity; 100 nA/V).

The current pathway from junction A along tube 2 shows the resistance to increase in small steps and a significant increase in resistance is registered when tube 2 is intersected by tube 3 (D: ~ 3.2 nm) to form junction B. The resistance increase at junction B is ~100 kΩ as shown in the resistance versus distance plot in Fig.7.1C. Further tracing the resistance along tube 2 shows the resistance to remain stable only to increase again at junction C where tube 2 intersects tube 4 (D: ~ 2.8 nm).

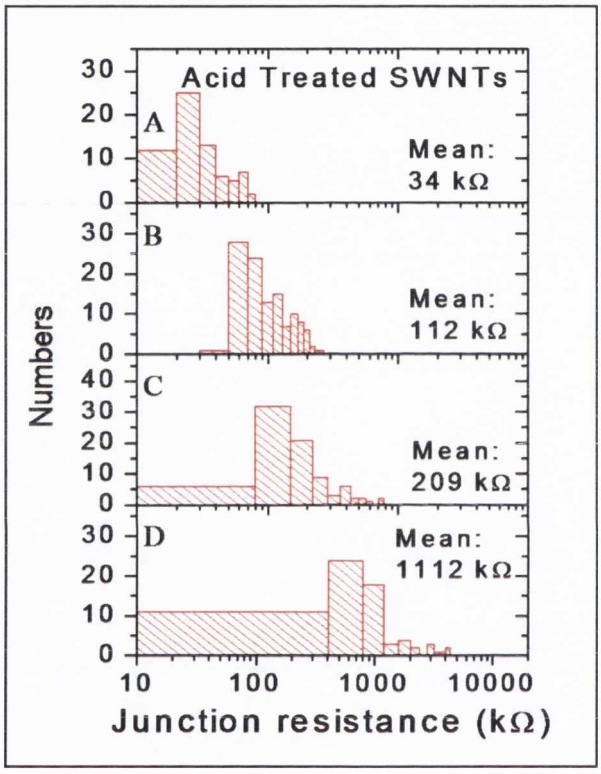

Figure 7.2: Statistical analysis of the junction resistance between acid treated tubes as a function of the tube diameter. The measured junction resistance decreases by a factor of 3 times when compared to the junction resistance of pristine nanotubes. Case A, B, C, D are the junction resistance measured between individual tubes (D: 1.2 - 1.8 nm), between individual nanotubes and smaller diameter nanotube bundles (diameter: 2.5 - 4.5 nm), between medium diameter nanotube bundles (diameter: 4.5 - 6.8 nm) and the junction resistance between larger diameter nanotube bundles (D: 7 – 14 nm), respectively.

The resistance at the junction C is ~ 120 kΩ and the resistance is observed to remain stable along pathway 1 but as we trace along tube 4 from junction C the resistance is seen to increase as shown in Fig. 7.1C and this is also evident from the difference in the colour coded current map (Fig. 7.1B). Even these preliminary initial results show that junction resistance values between acid treated nanotubes of varying diameters is several factors lower than the junction resistance measured between pristine nanotubes in the earlier study. We have performed a detailed analysis on the junction resistance as a function of the diameter of the tubes (similar to the studies in chapter 6), and plotted the data in their respective binning categories shown in Fig. 7.2.

The mean junction resistance between two single tubes is ~34 kΩ and the junction resistance increases as the diameter of the tube increases. The largest measured junction resistance is between larger diameter bundles (D: 7 – 14 nm) which have a mean junction resistance of ~1112 kΩ. Also the acid treatment effectively removes most of the non-carbonaceous content that is buried between larger diameter bundles and results in junction resistance values that are much lower than the junction resistance values obtained for larger diameter pristine tube junctions. The trend is similar to that for pristine tubes were the junction resistance increased as the diameter of the tubes forming the junctions were increased. Remarkably, we find that in each case the junction resistance is reduced over that of the pristine tubes. The largest reduction is observed for junctions comprised of single tubes, where a three-fold drop is observed. Once the effect of acid treatment on the junction resistance between nanotubes was analysed we investigated the intrinsic resistivity of the tubes after the acid treatment. A separate analysis of the individual acid treated tubes connected to the electrodes sheds information on the resistivity of each tube. (Calculation and methodology is discussed in detail in chapter 5 and chapter 6). Performing similar analysis provides us with the mean resistivity of acid treated nanotubes to be $(2.8 \pm 0.8) \times 10^{-8}$ Ωm after averaging over 30 single tubes.

This data clearly highlights that acid treatment does induce additional carriers into the 1D nanotube architecture which moves the Fermi level closer to the valence band edge thereby reducing the intrinsic resistivity of an individual tube by 30 % when compared to the intrinsic resistivity of an individual pristine nanotube.

Effect of Annealing Treatment

Having shown how acid treatment affects the junction resistance, we might expect a related effect after annealing. A simple junction occurring between two annealed tubes is shown in Fig. 7.3A, where an individual tube (D: ~1.6 nm) forms an intersecting X-junction with a smaller diameter bundle (D: ~2.2 nm) that is connected to the electrode. As we trace the local resistance along the nanotube bundle from the current map (Fig.7 3B), the resistance at the junction is found to be ~1.3 MΩ.

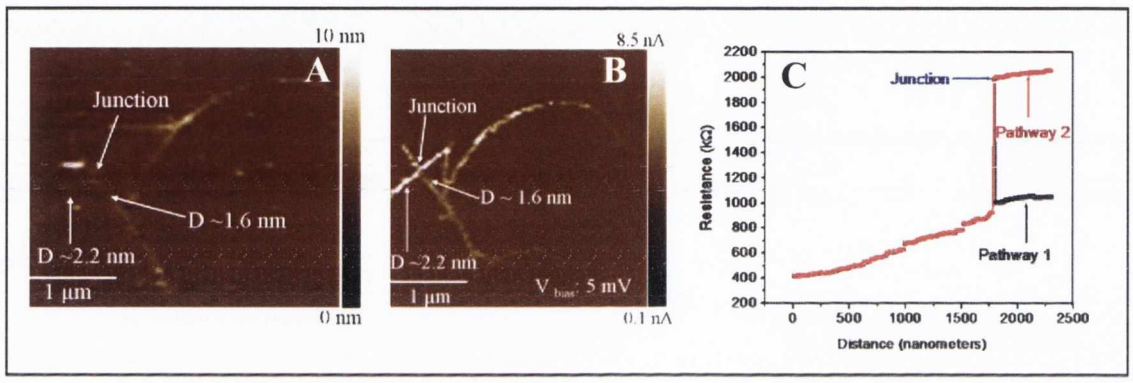

Figure 7.3: Junction resistance analysis of annealed tubes. (A) & (B) Topography and current map of a smaller diameter bundle, (D: ~2.2 nm) connected to the electrode on the left hand side of the image (not shown) and intersected by an individual tube (D : ~1.6 nm). (C) The plot shows the resistance to increase by ~1.3 MΩ at the junction point. Pathway 1 and pathway 2 shown in Fig. 3B is the resistance traced along the bundle and the resistance traced from the bundle through the interconnecting individual tube. (Scanning conditions: V_{bias}: 5 mV, Preamplifier sensitivity; 100 nA/V)

Furthermore the resistance drops back to its previous value as we continue measuring along tube 1 as shown in pathway 1 (black trace, Fig. 7.3C). Alternatively as we trace along pathway 2 which is along the single tube, the resistance is found to be much higher and it increases with the distance from the electrode.

Statistical analysis of the junction resistance of the annealed tubes as a function of the diameter of the constituent bundles clearly shows that controlled annealing increases the junction resistance by a factor of nearly 3 times when compared to the junction resistance of the pristine tubes.

Analysing a large population of annealed junctions resulted in similar increase in the inter tube resistance and categorizing these junction resistance values based on the diameter of the tubes forming the junctions reveals a clear increase in the junction resistance as the diameter of the corresponding tubes is increased.

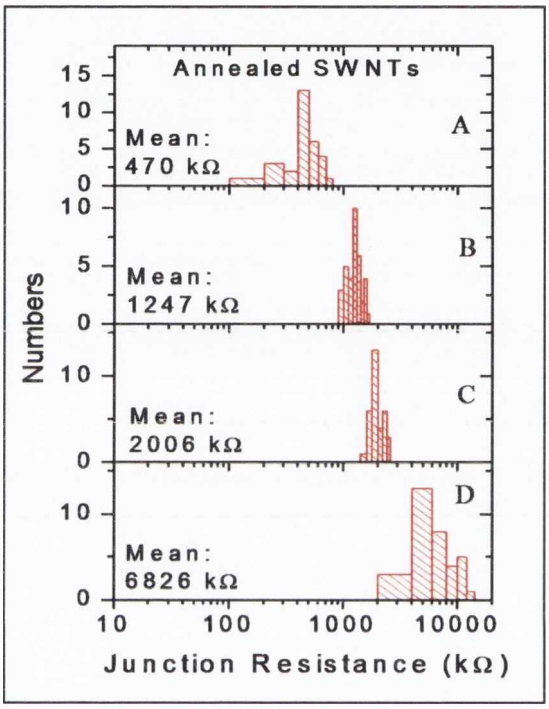

Figure 7.4: Statistical analysis of the junction resistance between annealed tubes as a function of the tube diameter. The junction resistance is clearly observed to increase by a factor of nearly 4 times when compared with the junction resistance of pristine tubes. Case A, B, C, D are the junction resistance measured between individual tubes (diameter: 1.2-1.8 nm), between individual nanotubes and smaller diameter nanotube bundles (D: 2.5-4.5 nm), between smaller diameter nanotube bundles (D: 4.5-6.8 nm) and between larger diameter nanotube bundles (D: 7-14 nm).

The resistance at the junction increases markedly in all 4 different categories (A, B, C, D) when compared with the pristine nanotube junctions. Especially the junctions between individual tubes (Case A, Fig.7.4) shows an average junction resistance value of ~ 470 kΩ which is a striking increase when compared to the mean junction resistance value between individual pristine tubes of ~ 98 kΩ.

Further analysis of an isolated individual annealed tube resulted in mean tube resistivity of $(5.9 \pm 1.1) \times 10^{-8}$ Ωm. The data obtained from the annealed tubes highlights the significant effect of de-doping of the nanotubes as a result of annealing treatment where the intentional and unintentional dopants are removed from the system, thereby increasing both the junction resistance and the specific resistivity of an individual annealed tube.

Comparative Analysis of Pristine, Acid Treated & Annealed SWCNTs.

Analyzing the junctions between individual pristine (~98 kΩ), acid treated (~34 kΩ) and annealed tubes (~470 kΩ) reveals an interesting phenomenon where a three fold decrease in junction resistance between two individual tubes after acid treatment. Furthermore annealing a pristine nanotube junction in argon at 1000 ^{o} C for 12 hours results in a marked increase in the junction resistance which is certainly due to the removal of external dopants on the nanotubes that control the p-type conduction in these materials. On the other hand, the intrinsic resistivities of the nanotubes undergoes a much smaller change after each treatment thereby highlighting that doping is not the only reason for the observed decrease in the junction resistances (See table 2). In order to obtain a clearer picture we performed a standard 4 probe electrical measurement on thicker nanotube networks and analyzed their sheet resistance after each subsequent post processing method. Incorporating these networks onto transparent substrates like PET and quartz allowed us to calculate the optical transmittance these networks. The sheet resistance of a pristine nanotube network was ≈110 Ω/square for films on both PET and quartz and the optical transmittance measurements gave values of ≈78% (λ=550 nm) for networks on both substrates. These values allow us to calculate the optical and DC conductivity of the nanotube networks analyzed. Sheet resistance and transmittance are related by [209]

$$T(\lambda) = \left(1 + \frac{188.5}{R_s}\frac{\sigma_{Op}(\lambda)}{\sigma_{DC}}\right)^{-2} \qquad \text{Equation 1}$$

Where σ_{DC} and σ_{Op} are the DC and optical conductivities, respectively.

As σ_{Op} is generally close to 1.7×10^4 S/m for nanotube films [150, 209, 238] the problem of maintaining high transparency at high conductivities reduces to maximizing σ_{DC}. While DC conductivity depends on the network morphology [217], the most important factor determining network conductivity is believed to be the inter tube electron transfer at nanotube-nanotube junctions [217] which has been the focus of this study. Using equation 1 we can calculate that these R_s and T values imply a value of $\sigma_{DC}/\sigma_{Op}\approx13$. This value is comparable to the best performance reported for untreated nanotube networks [144]. Taking $\sigma_{Op}=1.7\times10^4$ S/m, we calculate $\sigma_{DC} \approx 2.2\times10^5$ S/m for both substrates. In the case of acid treated films we measured sheet resistance and transmittance on PET to be 37 Ω/square and 76% respectively. This corresponds to values of $\sigma_{DC}/\sigma_{Op}= 35$ and $\sigma_{DC} = 6\times10^5$ S/m. We note that these values are extremely high and compare favorably with the best films produced to date [143, 147].

Type of Nanotube	Mean Intrinsic Resistivity ($\times 10^{-8}$ Ωm)	Mean Junction Resistance (kΩ)	Bulk Film Conductivity, σ_{DC} (S/m)	Sheet Resistance (Ω/□)
Pristine	4.3 ± 0.7	98 ± 3.8	1.7×10^4	110
Acid Treated	2.8 ± 0.8	34 ± 1.8	6×10^5	37
Annealed	5.9 ± 1.1	470 ± 16.5	9×10^4	285

Table 2: Summary of the local and bulk electronic characterization of individual carbon nanotubes and carbon nanotube networks. Acid treatment is clearly seen to reduce the junction resistance thereby increasing bulk film conductivity. Whereas annealing increases the resistance at the junctions hence leading to poor conductivity in bulk films.

Finally for annealed films, we measured the sheet resistance and transmittance of 285 Ω/square and 79% respectively. This corresponds to values of $\sigma_{DC}/\sigma_{Op} = 5.3$ and $\sigma_{DC} = 9\times10^4$ S/m. The annealed films are less conductive than pristine or acid treated films.

Table 2 summarizes the values of intrinsic resistivity, junction resistance, DC conductivity and sheet resistance of the pristine nanotube networks and post processed networks. Comparing the results from the nanoscale CI-AFM measurements and the macroscopic 4-probe electrical measurements a common trend is observed relating to the effect of the post processing treatment. In order to verify the complementary results from these studies we formulate an equation where the overall conductivity of the network is associated with the measured junction resistance values. Geometrical scaling arguments [155, 156, 217] have shown that the conductivity, σ, of disordered nanotube films scales linearly with the number density of network junctions N_j, which in turn scales with the network morphology though the film fill-factor, V_f, the diameter , D of the bundles and the mean junction resistance, $\langle R_J \rangle$:

$$\sigma = \frac{K}{\langle R_J \rangle} \frac{V_f^2}{\langle D \rangle^3} \qquad \text{Equation 2}$$

Here K is the proportionality factor which scales with the bundle length as a separate analysis recently revealed that $\sigma \propto L^{1.7}$ [156].

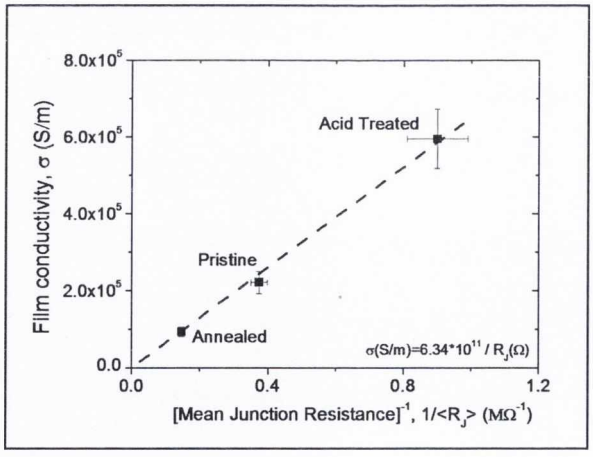

Figure 7.5: Plot of measured film conductivity as a function of the inverse of mean junction resistance measured for pairs of larger bundles (see panels D in fig. 6.9 (ch 6) fig. 7.2, 7.4 (Ch 7)). The error in junction resistance is the standard error of the distribution while the error in film resistivity is associated with the calculation of the film thickness.

Equation 2 predicts that the network conductivity scales inversely with the mean junction resistance. Given measurements for both junction resistance and film conductivity for pristine, acid-treated and annealed NTNs, we can test the inverse relationship predicted by equation 2.

We use the conductivities for the pristine, acid treated and annealed films discussed above. We take the mean junction resistance for the large bundle junctions (see panel D in Fig. 6.9 (Ch 6) Fig.7.2, 7.4 (Ch 7)). This is because the thicker films used for conductivity measurements tend to have higher bundle diameters ($\langle D \rangle$~20 nm). We plot this data in Fig. 7.5, as film conductivity versus the inverse of mean junction resistance, $1/\langle R_J \rangle$ and find a near perfect linearity, indicating very good agreement between experiment and model.

IV. Conclusion

The influence of acid treatment and annealing on carbon nanotubes tubes has been investigated in detail. Acid treatment effectively improves the overall conductivity of the network and results in a significant lowering of the junction resistance. We speculate that the barriers at junctions are related to charge transfer between tubes and that the availability of additional carriers in highly doped tubes effectively screen these electrostatic interactions. Our conclusions are supported by the recent work of Barnes et al. [237]. By carrying out temperature dependent electrical measurements on nanotube films, where they have shown that in addition to doping, chemical treatment of nanotube films tends to alter the potential barrier at inter-nanotube junctions. This would in turn alter the effective junction resistance as we have demonstrated here. Furthermore annealing has shown to de-dope the nanotubes which is consistent with previous studies [159, 239] and has resulted in a large increase in the inter tube resistance followed by lowering of the bulk network conductivity. The excellent agreement between the predicted model and the experimental results shows categorically that film properties are controlled by the junctions.

V. Acknowledgements

I would like to thank Philip Lyons, Sukanta De and Amro Satti for providing me with the nitric acid treated tubes and Prof Jonathan Coleman for discussions on the modelling part.

VI. References

[1] R. Graupner *et al.*, Phys. Chem. Chem. Phys. **5**, 5472 (2003).
[2] V. Skakalova *et al.*, Journal of Physical Chemistry B **109**, 7174 (2005).
[3] H. Z. Geng *et al.*, Journal of the American Chemical Society **129**, 7758 (2007).
[4] M. E. Itkis *et al.*, Journal of the American Chemical Society **127**, 3439 (2005).
[5] E. B. Craig *et al.*, Angewandte Chemie International Edition **45**, 2533 (2006).
[6] M. Pumera, Langmuir **23**, 6453 (2007).
[7] K. Taras, and P. Martin, Small **4**, 1476 (2008).
[8] T. M. Barnes *et al.*, Acs Nano **2**, 1968 (2008).
[9] T. M. Barnes *et al.*, Physical Review B **75** (2007).
[10] G. Fanchini, H. E. Unalan, and M. Chhowalla, Applied Physics Letters **90** (2007).
[11] E. M. Doherty *et al.*, Carbon **47**, 2466 (2009).
[12] L. Hu, D. S. Hecht, and G. Gruner, Nano Letters **4**, 2513 (2004).
[13] B. Ruzicka *et al.*, Physical Review B **61**, R2468 (2000).
[14] P. E. Lyons *et al.*, Journal of Applied Physics **104** (2008).
[15] H. Z. Geng *et al.*, Chemical Physics Letters **455**, 275 (2008).
[16] Z. C. Wu *et al.*, Science **305**, 1273 (2004).
[17] D. Hecht, L. B. Hu, and G. Gruner, Applied Physics Letters **89** (2006).
[18] D. Simien *et al.*, Acs Nano **2**, 1879 (2008).
[19] Y. Zhao, and W. Li, Microelectronic Engineering **87**, 576.
[20] W. Zhou *et al.*, Journal of Applied Physics **95**, 649 (2004).

This chapter has been published in Nano Letters "Electrical connectivity in single walled carbon nanotube networks" Peter N. Nirmalraj et al. 2009, 9, (11), 3890-3895.

General Conclusion

Well dispersed solutions of SWCNT's were obtained by dispersing the pristine nanotube powder in amide solvents. These nanotube solutions were then spray coated onto respective substrates to form homogeneous and well interconnected networks. The spray coating approach allows us to achieve the desired network thickness by varying the quantity of the dispersion volume and the number of passes. To facilitate electrical measurements the nanoscopic materials were contacted using macroscopic electrodes formed by a range of materials from Pd to Ti/Au. We also demonstrated that it is possible to selectively analyse the metallic tubes from their semiconducting counterparts by applying a positive bias as gate voltage, which sweeps the carriers from the semiconducting tubes leaving only the metallic tubes visible in the current map.

The local electrical interface between the SWCNT and the metal electrode has been thoroughly probed as part of this study. The contact resistance between the nanotube (metallic / semiconducting) and the metal electrode was minimised by applying a local voltage pulse (6 V for ~ 2 seconds) using the conductive probe and an optimised loading force (~ 1 nN) to the region of the metal electrode contacting the nanotube.

We believe that the combination of local Joule heating and pressure is important in assisting in the formation of chemical bonds for achieving good electrical contacts. Furthermore Pd contacted semiconducting tubes show a 45% decrease in contact resistance when compared to only 15 % decrease for Ti/Au contacted semiconducting tubes. These results confirm that the optimization process leads to an effective collapse of the Schottky barrier so that it is possible to tunnel through the remnant barrier with minimum resistance. Using this technique we demonstrate that Pd forms superior contacts resulting in very low contact resistance value of ~11 kΩ when compared to Ti/Au which offers a contact resistance of ~ 25 kΩ after the pulsed annealing treatment in the case of metallic tubes. This localised annealing method is also effective in removing any unintentionally adsorbed molecules between the metal and nanotube interface which are known to increase the contact resistance between these two systems especially when measurements are performed in ambient conditions.

In addition Pd contacts were observed to be more stable over a period of time as the contact resistance of Pd contacted tubes did not undergo a huge change when compared to the tubes contacted by Ti/Au electrodes. This is primarily due to the noble character of Pd and the excellent wetting interactions with nanotubes. Even though Au is deposited over the chemically reactive Ti, it does not prevent the slow oxidation of Ti thereby leading to an increase in contact resistance as time progresses.

Having optimised the contacts to the nanotubes we analysed the electronic behaviour of nanotube networks as a function of thickness. Based on the thickness which is proportional to the volume of the dispersion sprayed, networks were classified as sparse, thin and thick respectively. The simultaneously obtained current and morphology data of the networks allowed us to monitor the electronic behaviour of these systems as they transit from a sparse to a thick network. Sparse networks were found to me more resistive where the local electronic variations (metallic or semiconducting) of individual tubes dominate the overall network properties. Whereas as the network thickness is increased the network becomes more conductive due to the availability of a larger number of well interconnected tubes.

Also to the dramatic increase in the number of the connection with thickness, here is a much higher probability for an all metallic pathway bridging the source and drain electrode as the network density is scaled in steps. Complementary four probe measurements offers the possibility to register the onset of conductive pathways in the network as a function of dispersion volume from which the overall sheet resistance is calculated. The tipping point for electrical conduction is registered and the critical density of the networks at a critical volume of 3.5 mL was calculated to be 1.5 CS/μm^2. The sheet conductance is observed to increase as the volume of the dispersion is increased and stabilises beyond a certain network thickness. This investigation clearly highlights that the drop in conductance in a sparse network coincided with the local junction hotspots between the nanotubes, thereby showing that it is essential to understand junctions in finer detail. Naturally occurring junctions seem to take different configurations like X, Y, head-tail arrangement and spliced junctions.

This variation in junction morphology depends on the aspect ratio of the nanotube and the method in which they are deposited on the surface. In order to analyse the junction resistance we categorized the junctions based on the diameter of the constituent tubes.

We measured the junction resistance between several hundred nanotubes and find the junction resistance to scale with the nanotube diameter. We measure a mean junction resistance of ~98 kΩ between two individual nanotubes which is one of the lowest reported values in literature [124, 215]. The resistance measured over junctions involving nanotube bundles (both smaller and larger diameter bundles) presents a more intriguing study as the bundle is composed of individual tubes. There exists a measurable resistance between the tubes in the bundle and the overall resistance of that bundle. We find that in order to construct highly conductive networks based on nanotubes it is necessary to have smaller diameter bundles and a higher population of individual tubes as they offer lower junction resistance values when compared to medium and larger diameter bundles.

In an effort to maximise the conductivity of the pristine nanotubes we treated them with nitric acid and analysed their intrinsic resistivity and their corresponding junction resistance values. Apart from removing the non carbonaceous content from the nanotube networks, acid treatment has shown to effectively reduce the junction resistance of the nanotubes and a significant three fold decrease is observed in the case of the junctions between individual tubes. We speculate that the barriers at junctions are related to charge transfer between tubes and that the availability of additional carriers in highly doped tubes effectively screen these electrostatic interactions. Furthermore the intrinsic resistivity of a nanotube after acid treatment reduces by 30 % ($\rho = (2.8 \pm 0.8) \times 10^{-8}$ Ωm) when compared to the intrinsic resistivity of a pristine nanotube ($\rho = (4.3 \pm 0.7) \times 10^{-8}$ Ωm).

In order to study the effect of de-doping on the SWCNT's we carried out a controlled annealing procedure which resulted in the removal of the dopants from the system resulting in a remarkable increase in the junction resistance by a much as a factor of three times when compared to the pristine nanotubes. Also the resistivity of the nanotube tends to increase by 30 % ($\rho = (5.9 \pm 1.1) \times 10^{-8}$ Ωm) after the annealing procedure reflecting the effect of de-doping.

Simultaneous bulk electrical analysis of the pristine, acid treated and annealed networks exhibit a sheet resistance of 110 Ω/square, 37 Ω/square and 285 Ω/square respectively. This data complements the previous CI-AFM studies where a similar trend of electronic behaviour is observed between the pristine and post treated tubes.

The optical and DC conductivity data of these networks can be extracted based on the measured sheet resistance and transmittance. The acid treated networks exhibits the highest DC conductivity of 6×10^{5} S/m when compared to the pristine and annealed networks. To verify the correlation between the nanoscopic and macroscopic data sets we showed that this behaviour was well described by a model that correlates the overall conductivity of the networks with the mean junction resistance, where the network conductivity is predicted to scale inversely with the mean junction resistance.

Testing the model with the measured mean junction resistance for the larger bundle junctions and using the conductivities of the networks we find a near perfect linearity, demonstrating very good agreement between the conducted experiments and predicted model. Furthermore this result demonstrates that while the acid treatment and annealing procedures slightly alters the intrinsic conductivity of the pristine tubes, the most significant change induced by these post processing techniques is the changes in junction resistance that dictates the overall network conductivity. In addition the measured junction resistance values indicate conclusively the critical role of de-bundling in controlling the conductivity of nanotube films.

In summary, we have verified that the resistance of nanotube network junctions is strongly dependent on the diameter of the constituent tubes, with the smallest values associated with individual tubes. Finally, the measured junction resistances for pristine, acid-treated and annealed SWNT bundles correlate with the measured conductivities of the corresponding films, in excellent agreement with a simple model in which junctions control the overall network performance.

References

[1] G. Binnig *et al.*, Surface Science **189**, 1 (1987).
[2] G. Binnig, C. F. Quate, and C. Gerber, Physical Review Letters **56**, 930 (1986).
[3] G. Binnig, and H. Rohrer, Reviews of Modern Physics **59**, 615 (1987).
[4] G. Binnig *et al.*, Physical Review Letters **49**, 57 (1982).

[5] L. Gross *et al.*, Science **325**, 1110 (2009).
[6] P. Kowalczyk *et al.*, Applied Physics A: Materials Science & Processing **87**, 37 (2007).
[7] O. Marti *et al.*, Surface Science **181**, 230 (1987).
[8] D. M. Eigler, and E. K. Schweizer, Nature **344**, 524 (1990).
[9] I. W. Lyo, and P. Avouris, Science **253**, 173 (1991).
[10] D. M. Eigler, C. P. Lutz, and W. E. Rudge, Nature **352**, 600 (1991).
[11] N. Nilius, T. M. Wallis, and W. Ho, Science **297**, 1853 (2002).
[12] G. V. Nazin, X. H. Qiu, and W. Ho, Science **302**, 77 (2003).
[13] J. Repp *et al.*, Science **312**, 1196 (2006).
[14] L. Lafferentz *et al.*, Science **323**, 1193 (2009).
[15] A. J. Heinrich *et al.*, Science **298**, 1381 (2002).
[16] M. F. Crommie, C. P. Lutz, and D. M. Eigler, Science **262**, 218 (1993).
[17] L. Heller *et al.*, Phys Rev B Condens Matter **49**, 1104 (1994).
[18] H. C. Manoharan, C. P. Lutz, and D. M. Eigler, Nature **403**, 512 (2000).
[19] C. R. Moon *et al.*, Nat Nanotechnol **4**, 167 (2009).
[20] D. Kitchen *et al.*, Nature **442**, 436 (2006).
[21] S. W. Hla *et al.*, Phys Rev Lett **85**, 2777 (2000).
[22] J. K. Gimzewski *et al.*, Science **281**, 531 (1998).
[23] B. C. Stipe, M. A. Rezaei, and W. Ho, Science **279**, 1907 (1998).
[24] T. Komeda *et al.*, Science **295**, 2055 (2002).
[25] J. I. Pascual *et al.*, Nature **423**, 525 (2003).
[26] H. J. Lee, and W. Ho, Science **286**, 1719 (1999).
[27] C. F. Hirjibehedin, C. P. Lutz, and A. J. Heinrich, Science **312**, 1021 (2006).
[28] C. Gerber, and H. P. Lang, Nat Nanotechnol **1**, 3 (2006).
[29] C. T. Hsieh, J. Q. Liu, and J. T. Lue, Applied Surface Science **252**, 1899 (2005).
[30] S. A. Koch *et al.*, Applied Surface Science **226**, 185 (2004).
[31] T. Mélin *et al.*, Physical Review Letters **92**, 166101 (2004).
[32] K. Hiehata, A. Sasahara, and H. Onishi, Nanotechnology **18**, 084007 (2007).
[33] M. L. O'Malley *et al.*, Applied Physics Letters **74**, 272 (1999).
[34] A. Erickson *et al.*, Journal of Electronic Materials **25**, 301 (1996).
[35] L. Rispal *et al.*, Japanese Journal of Applied Physics Part 1-Regular Papers Brief Communications & Review Papers **45**, 3672 (2006).
[36] M. Stadermann *et al.*, Physical Review B **72** (2005).
[37] A. Fujiwara *et al.*, Applied Physics Letters **80**, 1993 (2002).
[38] P. J. de Pablo *et al.*, Advanced Materials **12**, 573 (2000).
[39] M. Stadermann *et al.*, Physical Review B **69**, 201402 (2004).
[40] P. N. Nirmalraj *et al.*, Nano Letters **9**, 3890 (2009).
[41] A. Fujiwara *et al.*, Physica B-Condensed Matter **323**, 227 (2002).
[42] T. Heim, D. Deresmes, and D. Vuillaume, Journal of Applied Physics **96**, 2927 (2004).
[43] D. Xu *et al.*, Nano Letters **5**, 571 (2005).
[44] A. P. Alivisatos, Acs Nano **2**, 1514 (2008).
[45] S. Iijima, Nature **354**, 56 (1991).
[46] H. Benisty, C. M. Sotomayor-Torrès, and C. Weisbuch, Physical Review B **44**, 10945 (1991).
[47] A. K. Geim, and K. S. Novoselov, Nat Mater **6**, 183 (2007).
[48] M. A. Hines, and P. Guyot-Sionnest, The Journal of Physical Chemistry **100**, 468 (1996).
[49] A. Mews *et al.*, The Journal of Physical Chemistry **98**, 934 (1994).
[50] C.-P. Lee, and D.-C. Liu, Applied Surface Science **92**, 519 (1996).

[51] J. H. Ryou, and R. D. Dupuis, Journal of Electronic Materials **32**, 18 (2003).
[52] D.-z. Yang, S.-k. Xu, and Q.-f. Chen, Spectroscopy and Spectral Analysis **27**, 1807 (2007).
[53] K. Sears *et al.*, (Inst. of Elec. and Elec. Eng. Computer Society, Brisbane, Australia, 2006), pp. 505.
[54] D. W. Zhang *et al.*, (SPIE, Wuhan, China, 2009), pp. Chinese Optical Society; Huazhong University of Science and Technology; China Hubei Provincial Science Technology Department; Adm. Comm. Wuhan East Lake High.
[55] R. C. Ashoori, Nature **379**, 413 (1996).
[56] I. K. Ng, and H. Suzuki, (Maney Publishing, Suite 1C, Joseph's Well, Hanover Walk, Leeds, LS3 1AB, United Kingdom, 2009), pp. 192.
[57] W. S. Shi *et al.*, Applied Physics Letters **78**, 3304 (2001).
[58] J. V. D. S. Araujo *et al.*, Solid State Sciences **11**, 1673 (2009).
[59] H. Gerung *et al.*, Journal of the American Chemical Society **128**, 5244 (2006).
[60] H. S. Shin, J. Y. Song, and J. Yu, Materials Letters **63**, 397 (2009).
[61] S. Biswas *et al.*, Journal of Physical Chemistry C **113**, 3617 (2009).
[62] K.-B. Tang *et al.*, Advanced Materials **15**, 448 (2003).
[63] W. Zhiyu, Z. Zongbin, and Q. Jieshan, Chemistry of Materials **19**, 89 (2007).
[64] C. Z. Li, and et al., Nanotechnology **10**, 221 (1999).
[65] Y. Oshima *et al.*, Journal of the Physical Society of Japan **75**, 053705 (2006).
[66] B. Rodell *et al.*, Nanostructured Materials **7**, 229 (1996).
[67] L. T. Ngo *et al.*, Nano Lett **6**, 2964 (2006).
[68] Y. Kim *et al.*, (SPIE, Gwangju, Korea, Republic of, 2006), pp. SPIE; Optical Society of Korea.
[69] K. S. Novoselov, Science **306**, 666 (2004).
[70] F. Miao *et al.*, Science **317**, 1530 (2007).
[71] D. A. Abanin *et al.*, Phys Rev Lett **98**, 196806 (2007).
[72] K. S. Novoselov *et al.*, Science **315**, 1379 (2007).
[73] A. H. Castro Neto *et al.*, Reviews of Modern Physics **81**, 109 (2009).
[74] J. Nilsson *et al.*, Phys Rev Lett **97**, 266801 (2006).
[75] C. Lee *et al.*, Science **321**, 385 (2008).
[76] Y. Hernandez *et al.*, Nat Nanotechnol **3**, 563 (2008).
[77] A. Reina, Nano Lett. (2008).
[78] W. Cai *et al.*, Applied Physics Letters **95**, 123115 (2009).
[79] K. S. Kim *et al.*, Nature **457**, 706 (2009).
[80] S. Iijima, and T. Ichihashi, Nature **363**, 603 (1993).
[81] H. W. Kroto, Nature **329**, 529 (1987).
[82] H. W. Kroto *et al.*, Nature **318**, 162 (1985).
[83] R. Saito *et al.*, Applied Physics Letters **60**, 2204 (1992).
[84] E. Couteau *et al.*, Chemical Physics Letters **378**, 9 (2003).
[85] C. Journet *et al.*, Nature **388**, 756 (1997).
[86] Y. Y. Wei *et al.*, Applied Physics Letters **78**, 1394 (2001).
[87] M. Yudasaka *et al.*, The Journal of Physical Chemistry B **103**, 6224 (1999).
[88] K. D. Ausman *et al.*, The Journal of Physical Chemistry B **104**, 8911 (2000).
[89] S. D. Bergin *et al.*, ACS Nano **3**, 2340 (2009).
[90] S. Giordani *et al.*, Journal of Physical Chemistry B **110**, 15708 (2006).
[91] H. Wang, Current Opinion in Colloid and Interface Science **14**, 364 (2009).
[92] P. K. Rai *et al.*, (American Scientific Publishers, 25650 North Lewis Way, Stevenson Ranch, CA 9138-1439, United States, 2007), pp. 3378.
[93] J. Amiran *et al.*, The Journal of Physical Chemistry C **112**, 3519 (2008).
[94] S. Li *et al.*, Nano Letters **4**, 2003 (2004).

[95] R. Martel *et al.*, Physical Review Letters **87**, 256805 (2001).
[96] S. J. Tans *et al.*, Nature **386**, 474 (1997).
[97] C. Zhou, J. Kong, and H. Dai, Phys Rev Lett **84**, 5604 (2000).
[98] A. Javey *et al.*, Nano Letters **4**, 447 (2004).
[99] A. Javey *et al.*, Physical Review Letters **92**, 106804 (2004).
[100] A. Javey *et al.*, Nature **424**, 654 (2003).
[101] A. A. Kane *et al.*, Nano Letters **9**, 3586 (2009).
[102] A. N. Andriotis *et al.*, Phys Rev Lett **87**, 066802 (2001).
[103] W. Dacheng, and L. Yunqi, Advanced Materials **20**, 2815 (2008).
[104] M. S. Fuhrer *et al.*, Science **288**, 494 (2000).
[105] P. A. Albrecht, and J. W. Lyding, (IEEE, Piscataway, NJ, USA, 2005), pp. 49.
[106] A. Hassanien *et al.*, (Elsevier, Switzerland, 2004), pp. 338.
[107] Z. Osvath *et al.*, Chemical Physics Letters **365**, 338 (2002).
[108] L. Tapaszto *et al.*, Journal of Physics: Condensed Matter **18**, 5793 (2006).
[109] J. W. Janssen *et al.*, Physical Review B (Condensed Matter and Materials Physics) **65**, 115423 (2002).
[110] L. Chico *et al.*, Physical Review B (Condensed Matter) **54**, 2600 (1996).
[111] Y. Young-Gui, and S. G. Louie, (Kluwer Academic Publishers, Dordrecht, Netherlands, 2001), pp. 233.
[112] J. Kong *et al.*, Phys Rev Lett **87**, 106801 (2001).
[113] W. Liang *et al.*, Nature **411**, 665 (2001).
[114] M. J. Biercuk *et al.*, Phys Rev Lett **94**, 026801 (2005).
[115] M. Bockrath *et al.*, Science **275**, 1922 (1997).
[116] M. Freitag *et al.*, Physical Review Letters **89**, 216801 (2002).
[117] A. Javey *et al.*, Nano Lett **5**, 345 (2005).
[118] J.-O. Lee *et al.*, Journal of Physics D: Applied Physics **33**, 1953 (2000).
[119] R. Seidel *et al.*, Nano Letters **3**, 965 (2003).
[120] C. Chen *et al.*, Nanotechnology **17**, 2192 (2006).
[121] Q. Chen, S. Wang, and L.-M. Peng, Nanotechnology **17**, 1087 (2006).
[122] L. Dong *et al.*, Journal of Applied Physics **101**, 024320 (2007).
[123] Y. Woo, G. S. Duesberg, and S. Roth, Nanotechnology **18**, 095203 (2007).
[124] Z. Yao *et al.*, Nature **402**, 273 (1999).
[125] N. Gothard *et al.*, Nano Letters **4**, 213 (2004).
[126] D.-H. Kim *et al.*, Nano Letters **6**, 2821 (2006).
[127] J.-M. Ting, and C.-C. Chang, Applied Physics Letters **80**, 324 (2002).
[128] I. Zsoldos *et al.*, Modelling and Simulation in Materials Science and Engineering **12**, 1251 (2004).
[129] P. Lambin, and V. Meunier, (Kluwer Academic Publishers, Dordrecht, Netherlands, 2001), pp. 265.
[130] M. Menon *et al.*, Physical Review Letters **91**, 145501 (2003).
[131] C. Papadopoulos *et al.*, Physical Review Letters **85**, 3476 (2000).
[132] M. S. Wang *et al.*, Advanced Functional Materials **15**, 1825 (2005).
[133] S. J. Tans, A. R. M. Verschueren, and C. Dekker, Nature **393**, 49 (1998).
[134] L. W. Liu *et al.*, Physical Review B **71**, 155424 (2005).
[135] E. Artukovic *et al.*, Nano Letters **5**, 757 (2005).
[136] C. M. Aguirre *et al.*, Applied Physics Letters **88** (2006).
[137] T. M. Barnes *et al.*, Physical Review B **75** (2007).
[138] T. M. Barnes *et al.*, Applied Physics Letters **90** (2007).
[139] S. De *et al.*, Acs Nano **3**, 714 (2009).
[140] E. M. Doherty *et al.*, Carbon **In press** (2009).
[141] G. Eda *et al.*, Applied Physics Letters **92** (2008).

[142] G. Fanchini, H. E. Unalan, and M. Chhowalla, Applied Physics Letters **90** (2007).
[143] H. Z. Geng *et al.*, Journal of the American Chemical Society **129**, 7758 (2007).
[144] H. Z. Geng *et al.*, Chemical Physics Letters **455**, 275 (2008).
[145] G. Gruner, Journal of Materials Chemistry **16**, 3533 (2006).
[146] B. B. Parekh *et al.*, Applied Physics Letters **90** (2007).
[147] Z. C. Wu *et al.*, Science **305**, 1273 (2004).
[148] E. Bekyarova *et al.*, Journal of the American Chemical Society **127**, 5990 (2005).
[149] G. Gruner, Scientific American **296**, 76 (2007).
[150] L. Hu, D. S. Hecht, and G. Gruner, Nano Letters **4**, 2513 (2004).
[151] M. Kaempgen *et al.*, Nano Letters **9**, 1872 (2009).
[152] V. Skakalova *et al.*, Physical Review B (Condensed Matter and Materials Physics) **74**, 85403 (2006).
[153] E. S. Snow *et al.*, Applied Physics Letters **82**, 2145 (2003).
[154] Z. Wu *et al.*, Science **305**, 1273 (2004).
[155] D. Simien *et al.*, Acs Nano **2**, 1879 (2008).
[156] D. Hecht, L. B. Hu, and G. Gruner, Applied Physics Letters **89** (2006).
[157] Y. Kim *et al.*, Synthetic Metals **156**, 999 (2006).
[158] V. Skakalova *et al.*, Journal of Physical Chemistry B **109**, 7174 (2005).
[159] Y. Zhao, and W. Li, Microelectronic Engineering **87**, 576.
[160] Pedro J. de Pablo *et al.*, Advanced Materials **12**, 573 (2000).
[161] H. Dai, Accounts of Chemical Research **35**, 1035 (2002).
[162] W. Wasel *et al.*, Carbon **45**, 833 (2007).
[163] T. W. Ebbesen, and P. M. Ajayan, Nature **358**, 220 (1992).
[164] C. Journet, and P. Bernier, Applied Physics A: Materials Science & Processing **67**, 1 (1998).
[165] C. Du, and N. Pan, Materials Letters **59**, 1678 (2005).
[166] S. Jong Lee *et al.*, Diamond and Related Materials **11**, 914.
[167] S. Hofmann *et al.*, Applied Physics Letters **83**, 135 (2003).
[168] K. V. Vijay, and X. Jining, edited by K. V. Vijay, and B. K. Laszlo (SPIE, 2003), pp. 204.
[169] K. Hata *et al.*, Science **306**, 1362 (2004).
[170] A.-C. Dupuis, Progress in Materials Science **50**, 929 (2005).
[171] M. J. Bronikowski *et al.*, in The 47th international symposium: Vacuum, thin films, surfaces/interfaces, and processing NAN06 (AVS, Boston, Massachusetts (USA), 2001), pp. 1800.
[172] V. Georgakilas *et al.*, Journal of the American Chemical Society **124**, 14318 (2002).
[173] K. C. Yao *et al.*, Advanced Materials **8**, 1012 (1996).
[174] J. L. Zimmerman *et al.*, Chemistry of Materials **12**, 1361 (2000).
[175] M. S. D. Dresselhaus, G; Eklund. P.C, (Academic Press, Newyork, 1996).
[176] J. Ernesto, ChemPhysChem **5**, 619 (2004).
[177] T. W. Odom *et al.*, Nature **391**, 62 (1998).
[178] J. W. G. Wilder *et al.*, Nature **391**, 59 (1998).
[179] B. J. F. Bruet *et al.*, Nat Mater **7**, 748 (2008).
[180] E. D. Minot *et al.*, Physical Review Letters **90**, 156401 (2003).
[181] R. Buzio *et al.*, Nat Mater **2**, 233 (2003).
[182] M. Raspanti, T. Congiu, and S. Guizzardi, Matrix Biology **20**, 601 (2001).
[183] H. Ximen, and P. E. Russell, Ultramicroscopy **42-44**, 1526 (1992).
[184] N. R. Wilson, and J. V. Macpherson, Nat Nanotechnol **4**, 483 (2009).
[185] K. Arstila *et al.*, Microelectronic Engineering **86**, 1222 (2009).

[186] T. Hantschel *et al.*, physica status solidi (a) **206**, 2077 (2009).
[187] G. Xiao *et al.*, Physica C: Superconductivity **341-348**, 769 (2000).
[188] G. Kazuya, and H. Kazuhiro, edited by A. M. Terry, and A. W. Mark (SPIE, 1997), pp. 84.
[189] M. R. Falvo *et al.*, Nature **397**, 236 (1999).
[190] S. Nuriel *et al.*, Chemical Physics Letters **404**, 263 (2005).
[191] J. Chen *et al.*, Science **282**, 95 (1998).
[192] E. T. Mickelson *et al.*, Journal of Physical Chemistry B **103**, 4318 (1999).
[193] E. T. Mickelson *et al.*, Chemical Physics Letters **296**, 188 (1998).
[194] A. Garg, and S. B. Sinnott, Chemical Physics Letters **295**, 273 (1998).
[195] M. F. Islam *et al.*, Nano Letters **3**, 269 (2003).
[196] V. Nicolosi *et al.*, Biomacromolecules **9**, 598 (2008).
[197] R. J. Murphy *et al.*, (SPIE-Int. Soc. Opt. Eng, USA, 2003), pp. 659.
[198] C. A. Furtado *et al.*, J Am Chem Soc **126**, 6095 (2004).
[199] S. Giordani *et al.*, J Phys Chem B **110**, 15708 (2006).
[200] G. Gruner, Nanosensing: Materials and Devices **5593**, 36 (2004).
[201] J. A. Bardecker *et al.*, Journal of the American Chemical Society **130**, 7226 (2008).
[202] C. Stéphan *et al.*, Synthetic Metals **108**, 139 (2000).
[203] H. J. Jeong *et al.*, Carbon **44**, 2689 (2006).
[204] Y. I. Song *et al.*, Journal of Colloid and Interface Science **318**, 365 (2008).
[205] R. D. Deegan *et al.*, Nature **389**, 827 (1997).
[206] M. Layani *et al.*, Acs Nano **3**, 3537 (2009).
[207] L. B. Hu, D. S. Hecht, and G. Gruner, Applied Physics Letters **94** (2009).
[208] L. B. Hu *et al.*, Applied Physics Letters **94** (2009).
[209] E. M. Doherty *et al.*, Carbon **47**, 2466 (2009).
[210] T. A. Beierlein *et al.*, Synthetic Metals **111-112**, 295 (2000).
[211] Z. Zhang *et al.*, Nano Letters **8**, 3696 (2008).
[212] L. Ding *et al.*, Nano Letters (2009).
[213] L. Marty *et al.*, Nano Letters **3**, 1115 (2003).
[214] T.-H. Kim *et al.*, Nanotechnology **19**, 485201 (2008).
[215] Z. Yao, C. L. Kane, and C. Dekker, Physical Review Letters **84**, 2941 (2000).
[216] J. Tersoff, Nature **424**, 622 (2003).
[217] P. E. Lyons *et al.*, Journal of Applied Physics **104** (2008).
[218] M. A. Topinka *et al.*, Nano Letters **9**, 1866 (2009).
[219] M. Ishigami *et al.*, Nano Lett **7**, 1643 (2007).
[220] G. E. Pike, and C. H. Seager, Physical Review B **10**, 1421 (1974).
[221] Y. B. Yi, and A. M. Sastry, Physical Review E **66**, 066130 (2002).
[222] G. Stauffer, *Introduction to percolation theory* (Taylor & Franics: London, 1985).
[223] S. Heinze *et al.*, Physical Review Letters **89**, 106801 (2002).
[224] H. W. C. Postma *et al.*, Science **293**, 76 (2001).
[225] R. Martel *et al.*, Applied Physics Letters **73**, 2447 (1998).
[226] P. Avouris, Z. H. Chen, and V. Perebeinos, Nature Nanotechnology **2**, 605 (2007).
[227] A. Buldum, and J. P. Lu, Applied Surface Science **219**, 123 (2003).
[228] N. R. Paudel *et al.*, Molecular Simulation **35**, 520 (2009).
[229] M. Terrones *et al.*, Phys Rev Lett **89**, 075505 (2002).
[230] H. W. C. Postma *et al.*, Physical Review B **62**, R10653 (2000).
[231] J. E. Fischer *et al.*, Physical Review B **55**, R4921 (1997).
[232] R. Graupner *et al.*, Phys. Chem. Chem. Phys. **5**, 5472 (2003).

[233] M. E. Itkis *et al.*, Journal of the American Chemical Society **127**, 3439 (2005).
[234] E. B. Craig *et al.*, Angewandte Chemie International Edition **45**, 2533 (2006).
[235] M. Pumera, Langmuir **23**, 6453 (2007).
[236] K. Taras, and P. Martin, Small **4**, 1476 (2008).
[237] T. M. Barnes *et al.*, Acs Nano **2**, 1968 (2008).
[238] B. Ruzicka *et al.*, Physical Review B **61**, R2468 (2000).
[239] W. Zhou *et al.*, Journal of Applied Physics **95**, 649 (2004).

Future Work

The research work that was performed as part of this PhD study was focussed primarily on probe microscopic analysis of the electronic properties of carbon nanotubes. We have shown well defined and reproducible techniques to investigate the local interactions between nanotube-nanotube and nanotube-metal electrode systems. Furthermore we have also demonstrated the methodology in which the resistivity of a one dimensional material can be extracted and the manner in which the effect of post processing techniques can be quantified. These techniques will act as a pathway for future experiments involving the analysis of other nanoscale materials and generating new probe microscopy based analytical techniques. Some prospective materials that can be probed using the CI-AFM technique are listed below.

Metal nanowires and nanoparticles: Using the conductive probe method the resistivity and the inter wire resistance can be obtained for metal nanowire systems and the IV curves for metal nanoparticles can also be acquired thereby delving detailed information on the local electronic properties of these materials. In addition the contact resistance between these materials and the respective metal electrode can be obtained and tuned in order to achieve minimal contact resistance.

Graphene flakes: The edge states of graphene and the inter flake resistance of these planar nanomaterials can be registered with excellent resolution. Moreover the presence of defects over the flake area and the influence of the layer thickness on the overall resistance of a graphene flake can be obtained. These results would provide rich information for both theoretical and experimental work that is currently being pursued by many research groups.

Hybrid nanoscale systems like carbon nanotube/polymer composites, carbon nanotube-metal nanowires and carbon nanotube-planar graphene sheets: Of particular interest would be the investigation of complex hybrid systems were the interaction between a one dimensional material with a two dimensional entity can be probed.

The interface between these various systems is interesting from an experimental and potential application perspective. A range of very interesting experiments can be performed by advancing the conductive imaging force microscopy technique from just electronic measurements to nanoscale manipulation. For instance the unzipping of a multiwalled carbon nanotube via controlled breakdown of its shells to form a graphene nanoribbon should be feasible with this CI-AFM technique. By applying a bias on the conductive probe and rupturing the walls of the nanotube with optimal loading force should result in a well structured and clean graphene ribbon as the outermost wall stretches out in a controlled manner. The CI-AFM methodology can be further extended to study vertically aligned nanostructures like nanowires (ZnO) and nanotubes grown by CVD synthesis, from which the resistivity of these materials can be derived. This technique can also be applied to other biological samples like DNA strands whose electrical properties can be measured with optimal loading force applications. For performing all the above discussed experiments a robust and stable tip is very important. Presently we have been using metal coated tips which restrict continuous measurements which limits the user from performing experiments involving higher loading force and the ability to increase the locally applied bias through the tip as these conditions are known to rapidly degrade the tip. To address this issue a dedicated experiment towards the fabrication of a home built solid metal tip which is robust and provides a faithful representation of the current and morphological map of the surface will be of extreme value for any work based on the CI-AFM technique.

While many of the basic transport phenomena in nanoscale conductive materials have been addressed and understood, endless opportunities await the utilization of the local probe microscopy technique to explore the intricacies involved in the science of the nanoscale world. The future of nanomaterials is very promising and they provide a showcase in which fundamental science and applications go hand in hand. This rich interplay between novel probe microscopy methodologies and the evolution of new nanomaterials is bound to further advance the field of nanoscience.

List of Publications

Peter N. Nirmalraj, Philip E. Lyons, Sukanta De, Jonathan N. Coleman and John J. Boland. **"Electrical connectivity in single walled carbon nanotube networks"**. Nano Letters. Vol 9, 11, 2009, 3890-3895.

Peter N. Nirmalraj and John J. Boland. **"Selective Tuning and Optimization of the Contacts to Metallic and Semiconducting Single Walled Carbon Nanotubes"** ACS Nano. Vol 4, 7, 2010, 3801–3806.

Peter N. Nirmalraj, Jonathan N. Coleman and John J. Boland. **"Unravelling the local electronic properties in complex nanoscale systems"**.The Journal of Microscopy and Analysis. Vol 24, 3. April 2010.

G.Behan, J.F.Feng, P.N.Nirmalraj, J.J.Boland and H.Z .Zhang. **"Effect of Sample Bias on Backscattered Ion Spectroscopy in the Helium Ion Microscope".** Manuscript accepted for publication in The Journal of Vacuum Science and Technology A.

Sukanta De, Tom Higgins, Philip E Lyons, Evelyn Doherty, Peter N. Nirmalraj, Werner J Blau, John J Boland and Jonathan N Coleman. **"Silver nanowire networks as flexible, transparent, conducting 1 films: Extremely high DC to optical conductivity ratios".** ACS Nano. Vol 3, 7, 2009, 1767-1774

Sukanta De, Philip E. Lyons, Sophie Sorel, Evelyn M. Doherty, Paul J. King, Werner J. Blau, Peter N. Nirmalraj, John J. Boland, Vittorio Scardaci, Jerome Joimel, and Jonathan N. Coleman. **"Transparent, Flexible, and Highly Conductive Thin Films Based on Polymer-Nanotube Composites"**. ACS Nano. Vol 3, 3 2009, 714-720.

Evelyn M. Doherty, Sukanta De, Philip E. Lyons, Aleksey Shmeliov, Peter N. Nirmalraj, Vittorio Scardaci, Jerome Joimel, Werner J. Blau, John J. Boland and Jonathan N. Coleman**. "The spatial uniformity and electromechanical stability of transparent, conductive films of single walled nanotubes".** Carbon, 4 7,2009, 2 4 6 6 –2 4 7 3

Yenny Hernandez, Valeria Nicolosi, Mustafa Lotya, Fiona M. Blighe, Zhenyu Sun, Sukanta De, I. T. McGovern, Brendan Holland, Michele Byrne, Yurri K. Gunko, John J. Boland, Peter P. Niraj, Georg Duesberg, Satheesh Krishnamurthy, Robbie Goodhue, John Hutchison, Vittorio Scardaci, Andrea C. Ferrari &Jonathan N. Coleman, **"High-yield production of graphene byliquid-phase exfoliation of graphite"** Nature Nanotechnology, Vol 3, 2008, 563-568.

Shane D. Bergin, Valeria Nicolosi, Philip V. Streich, Silvia Giordani, Zhenyu Sun, Alan H. Windle, Peter Ryan, N. Peter P. Niraj, Zhi-Tao T. Wang, Leslie Carpenter, Werner J. Blau, John J. Boland, James P. Hamilton, and Jonathan N. Coleman. **"Towards Solutions of Single-Walled Carbon Nanotubes in Common Solvents"** Advanced Materials, 20, 2008, 1-6.

P. Palmgren, B.R. Priya, N.P.P. Niraj, M. Gothelid **"Self-ordering of metal-free phthalocyanine on InAs (100) and InSb (100)"** J. Phys. Condens. Matter 18, 2006, 10707–10723.

P. Palmgren, B.R. Priya, N.P.P. Niraj, M. Gothelid **"Bonding of metal-free phthalocyanine to TiO2 (110) single crystal"** Solar Energy Materials & Solar Cells 90, 2006, 3602–3613.

Forthcoming Publications

Peter N. Nirmalraj, Tarek Lutz, Shishir Kumar, Georg Duesberg and John J. Boland. "**Probing interlayer interactions in graphene films**" Manuscript submitted to Nano Letters.